

# **ZnO Based Organic-Inorganic Hybrids: Properties and Device Applications**

**Ph.D. Thesis**

by

**Aaryashree**



**DISCIPLINE OF ELECTRICAL ENGINEERING  
INDIAN INSTITUTE OF TECHNOLOGY  
INDORE**

**December 2018**

# **ZnO Based Organic-Inorganic Hybrids: Properties and Device Applications**

**A Thesis**

*Submitted in partial fulfillment of the  
requirements for the award of the degree*

*of*

**DOCTOR OF PHILOSOPHY**

*by*

**Aaryashree**



**DISCIPLINE OF ELECTRICAL ENGINEERING  
INDIAN INSTITUTE OF TECHNOLOGY  
INDORE**

**December 2018**



# INDIAN INSTITUTE OF TECHNOLOGY INDORE

## CANDIDATE'S DECLARATION

I hereby certify that the work which is being presented in the thesis entitled **ZnO Based Organic-Inorganic Hybrids: Properties and Device Applications**, in the partial fulfillment of the requirements for the award of the degree of **Doctor of Philosophy** and submitted in the **Discipline of Electrical Engineering, Indian Institute of Technology Indore**, is an authentic record of my own work carried out during the time period from **July, 2014** to **October, 2018** under the supervisions of **Dr. Shaibal Mukherjee**, Associate Professor, Electrical Engineering, IIT Indore, and **Dr. Apurba K Das**, Associate Professor, Discipline of Chemistry, IIT Indore.

The matter presented in this thesis has not been submitted by me for the award of any other degree of this or any other institute.

Signature of the student with date

**AARYASHREE**

-----  
This is to certify that the above statement made by the candidate is correct to the best of our knowledge.

Signature of Thesis Supervisor #1 with date

**Dr. SHAIBAL MUKHERJEE**

Signature of Thesis Supervisor #2 with date

**Dr. APURBA K DAS**

-----  
**AARYASHREE** has successfully given her Ph.D. Oral Examination held on -----

Signature of Chairman OEB

Date:

Signature of External Examiner

Date:

Signature(s) of Thesis Supervisor(s)

Date:

Signature of PSPC Member #1

Date:

Signature of PSPC Member #2

Date:

Signature of Head of Discipline

Date:

Signature of Convener, DPGC

Date:

## ACKNOWLEDGEMENTS

Now, I am approaching the end of a long journey towards obtaining my PhD and being true, I would not have traveled this far without the help and encouragement of many people.

I express my profound sense of reverence to my supervisor **Dr. Shaibal Mukherjee**, for his endless guidance, support, motivation, and patient help during the course of my PhD. Under his guidance and encouragement, I successfully surpassed many difficulties and learned a lot. He is definitely a great supervisor. Also, I am extremely indebted to my co-supervisor, **Dr. Apurba K Das**, for his critical and constructive suggestions which have always been useful in improving my skills and for strengthening our manuscripts. I am very grateful for his untiring support to me.

I am extremely grateful to my doctoral committee members **Dr. Tushar Kanti Mukherjee** and **Dr. Vimal Bhatia** for giving me valuable advice on my research and kindly going through my dissertation. My sincere appreciation to **Dr. Ajay Agarwal**, Sr. Principal Scientist, Coordinator, Smart Sensors Area, and Head of Nano Biosensors Group at CSIR-Central Electronics Engineering Research Institute, Pilani., in providing valuable suggestion in the gas sensor project.

I would like to thank **Dr. Pradeep Mathur**, Director, IIT Indore for providing the essential experimental facilities and financial support in attending international conferences. I want to acknowledge the support provided by sophisticated instrumentation center (SIC) at IIT Indore, for performing SEM, EDX and XRD measurements.

I express my deepest gratitude to my co-authors who shared with me the stressful times and supported me with their knowledge; I owe very especial thanks to **Dr. Manoj K Manna**, **Vivek Garg**, **Brajendra Sengar** and **Biswajit Mandal** for their brilliant collaboration during this thesis. I am thankful to all the past and present members of the Hybrid

Nanodevice Research Group for their moral support, best wishes, and unforgettable days we spent together. I am grateful for all of you for providing a simulating and fun environment.

It's my fortune to gratefully acknowledge the support and encouragement of some special individuals. The words and emotions fail me to express deepest appreciations to my teacher, **Prof. D. Sivakumar** for his support, love and prayers. I strongly believe that his prayers played a significant role in my life.

My appreciations and gratitude to **my mother** are beyond all known words. I wish to acknowledge **my father** for his endless love, support, encouragement, and prayers during the entire journey of my life. I am grateful to **my entire family** for their sincere love. I pay regards to my lovely sister **Shiwangi** and my lovely brother **Amartya**. I am thankful for their sincere reassurances and motivations throughout my research work. I must express my appreciation to all **my in-laws' family** for their love, encouragement and best wishes for my PhD studies. I owe loving thanks to my husband **Ashish** for his unwavering understanding and support during these hard years. He was always there lifting me uphill this phase of life. Without your patience and encouragement nothing of this would have been achievable. Thanks for being beside me. Last but not the least, I owe my heartiest thanks to **Antim Mourya** and **Madhubala Mourya** for giving me the warmth of a family, so far from Jharkhand, and always being there like a guardian.

Aaryashree

© Copyright by AARYASHREE 2018

All Rights Reserved

*Dedicated to those  
most complaisant  
thoughtful  
appeasingly incorruptible  
and  
unquestionably indispensable  
persons in my life...*

*My Nanaji, Sri Kapil Dev Jha*

*My Bauji, Sri K N Singh*

*and*

*My Maa, Smt. Madhushree*

# LIST OF PUBLICATIONS

## A: Publications from Ph.D. Thesis Work

### A1. In Peer-reviewed Journals

1. **Aaryashree**, B. Mandal, R. Bhardwaj, S. Maiti, D.S. Sharma, A. K. Das, and S. Mukherjee, “*Functionalized oligo(p-phenylenevinylene) and ZnO based nanohybrid for selective ammonia sensing at room temperature,*” **IEEE Sensors Journal**, vol. 19, no. 8, pp 2847-2854, April, 2019. (**Impact factor: 2.617**)
2. **Aaryashree**, P. Sharma, B. Mandal, A. Biswas, M. K. Manna, S. Maiti, A. K. Das, and S. Mukherjee, “*Synergetic accrual of lamellar nano-hybrids for band-selective photodetection*” **Journal of Physical Chemistry C**, vol. 121, no.26, pp 14037-14044, June 16, 2017. (**Impact factor: 4.536**)
3. **Aaryashree**, S. Biswas, P. Sharma, V. Awasthi, B.S. Sengar, A. K. Das, and S. Mukherjee. “*Photosensitive ZnO- graphene quantum dot hybrid nanocomposite for optoelectronic applications,*” **ChemistrySelect**, vol. 1, no. 7, pp. 1503-1509, May 25, 2016. (**Impact factor: 1.505**)

### A2. In Proceedings of International Conferences

1. **Aaryashree**, B. Mandal, R. Bhardwaj, S. Maiti, A. K. Das, and S. Mukherjee, “*Self-assembled Zn-OPV composite for ammonia sensing,*” **17<sup>th</sup> International Meeting on Chemical Sensors (IMCS 2018)**, University of Vienna, Vienna. Austria, July 15-19, 2018.
2. **Aaryashree**, B. Mandal, R. G Jadhav, A. K. Das, and S. Mukherjee, “*Molar concentration variation in hydrothermal growth for highly porous Zn-BTC metal organic framework,*”

**19<sup>th</sup> International Workshop on The Physics of Semiconductor Devices (19<sup>th</sup> IWPSD)**, IIT Delhi, India, December 11-15, 2017.

3. **Aaryashree**, B. Mandal, R. G Jadhav, M. Das, A. K. Das, and S. Mukherjee, “*Study of ZnO-oligophenylenevinylene nano-hybrid for optoelectronic applications,*” **6<sup>th</sup> International Symposium on Integrated Functionalities**, Shangri-La’s Eros Hotel, Delhi, India, December 10-13, 2017.
4. **Aaryashree**, S. Biswas, V. Awasthi, B. S. Sengar, A. K. Das, and S. Mukherjee, “*Effect of electrochemical deposition time on optical properties of graphene quantum dots,*” **18<sup>th</sup> International Workshop on The Physics of Semiconductor Devices (18<sup>th</sup> IWPSD)**, IISc, Bangalore, India, December 7-10, 2015.

## **B: Other Publications during PhD.**

### **B1. In Peer-reviewed Journals**

1. B. Mandal, A. Biswas, **Aaryashree**, D. S. Sharma, R. Bhardwaj, M. Das, Md. A. Rahman, S. Kuriakose, M. Bhaskaran, S. Sriram, M. T. Htay, A. K. Das, and S. Mukherjee, “ *$\pi$ -conjugated amine-ZnO nanohybrids for the selective detection of CO<sub>2</sub> gas at room temperature,*” **ACS Applied Nano Materials**, accepted, Dec. 2018. (*Impact factor: Not available*)
2. B. Mandal, **Aaryashree**, M. Das, M. T. Htay, and S. Mukherjee, “*Architecture tailoring of MoO<sub>3</sub> nanostructures for superior ethanol sensing performance*”, **Materials Research Bulletin**, vol. 109, pp. 281-290, September 2018.
3. V. Garg, B. S. Sengar, P. Sharma, A. Kumar, **Aaryashree**, S. Kumar, S. Mukherjee, “*Sputter-instigated plasmon-enhanced optical backscattering layer in ultrathin solar cells: Application of GZO in CIGSe material system,*” **Solar Energy**, vol. 174, pp. 35-44, September 4, 2018. (*Impact factor: 4.374*)

4. B. Mandal, Aaryashree, R. Singh, and S. Mukherjee, “Highly selective and sensitive methanol sensor using rose-like ZnO microcube and MoO<sub>3</sub> micrograss based composite,” **IEEE Sensors Journal**, vol. 18, no. 7, pp. 2659-2666, April 1, 2018. (*Impact factor: 2.512*)
5. P. Sharma, Aaryashree, V.Garg, and S. Mukherjee, “Optoelectronic properties of phosphorus doped p-type ZnO films grown by dual ion beam sputtering,” **Journal of Applied Physics**, vol. 121, no. 225306, pp. 1-9, June 12, 2017. (*Impact factor: 2.068*)
6. V. Awasthi, V. Garg, B. S. Sengar, S. K. Pandey, Aaryashree, S. Kumar, C. Mukherjee, and S. Mukherjee, “Impact of sputter-instigated plasmonic features in TCO films: for ultrathin photovoltaic applications,” **Applied Physics Letters**, vol. 110, no. 103903, pp. 1-4, March 7, 2017. (*Impact factor: 3.411*)
7. M. K. Manna, Aaryashree, S. Verma, A. K. Das, and S. Mukherjee, “Lamellar peptide-cadmium-doped zinc oxide nanohybrids that emit white light” **ChemPlusChem**, vol. 81, no.3, pp. 329-337, March, 2016. (*Impact factor: 2.997*)
8. B. S. Sengar, V. Garg, V. Awasthi, Aaryashree, S. Kumar, C. Mukherjee, M. Gupta, and S. Mukherjee, “Growth and characterization of dual ion beam sputtered Cu<sub>2</sub>ZnSn(S,Se)<sub>4</sub> thin films for cost-effective photovoltaic application,” **Solar Energy**, vol. 139, pp. 1-12, September 17, 2016. (*Impact factor: 4.018*)
9. V. Garg, B. S. Sengar, V. Awasthi, Aaryashree, P. Sharma, C. Mukherjee, S. Kumar and S. Mukherjee, “Localized surface plasmon resonance on Au nanoparticles: tuning and exploitation for performance enhancement in ultrathin photovoltaics,” **RSC Advances**, vol. 6, pp. 26216-26226, March 1, 2016. (*Impact factor: 3.108*)

## **B1. In Proceedings of International Conferences**

1. B. Mandal, Aaryashree, M. Das, and S. Mukherjee, “*Synthesis of micrograss like  $\alpha$ - $\text{MoO}_3$  and their enhanced ethanol sensing performance*,” **6<sup>th</sup> International Symposium on Integrated Functionalities**, Shangri-La’s Eros Hotel, Delhi, India, December 10-13, 2017.
2. B. Mandal, Aaryashree, M. Das, and S. Mukherjee, “*Synthesis of high crystalline nanobelt like  $\alpha$ - $\text{MoO}_3$  and their alcohol sensing performance*,” **19<sup>th</sup> International Workshop on The Physics of Semiconductor Devices (19<sup>th</sup> IWPSD)**, IIT Delhi, India, December 11-15, 2017.
3. A. Kumar, M. Das, Md A. Khan, Aaryashree, Vivek Garg, A.Kranti and S. Mukherjee, “*Dual ion beam sputtered low-power and high-endurance resistive switching memory device with memristive behavior*,” **34<sup>th</sup> International Conference on the Physics of Semiconductors (ICPS 2018)**, Montpellier, France, July 29-Aug 03, 2018.
4. A. Kumar, M. Das, B. Mandal, R. Bhardwaj, Aaryashree, A. Kranti, and S. Mukherjee, “*Nano-scaled ZnO based resistive memory device fabricated by dual ion beam sputtering*,” **18<sup>th</sup> IEEE International Conference on Nanotechnology (IEEE NANO 2018)**, Cork, Ireland, July 23-26 2018.
5. R. Bhardwaj, B. Mandal, Md. A. Khan, Aaryashree, A. Kumar, and S. Mukherjee, “*Spectral photoresponse tunability of MgZnO based UV photodetectors*,” **18<sup>th</sup> IEEE International Conference on Nanotechnology (IEEE NANO 2018)**, Cork, Ireland, July 23-26 2018.
6. A. Kumar, M. Das, Aaryashree, Md A. Khan, R. Bhardwaj, A. Kranti, and S. Mukherjee, “*Interface-engineered forming-free dual ion beam sputtered ZnO based memristive device*,” **20<sup>th</sup>**

**International Conference on Superlattices, Nanostructures and Nanodevices (ICSNN2018)**, Madrid, Spain, July 23-26, 2018.

7. B. Mandal, Aaryashree, R. Bhardwaj, M. Das, D.S. Sharma, S. Mukherjee, “*Enhancement in methanol selectivity using MoO<sub>3</sub> micrograss encapsulated ZnO microcube,*” **IEEE SENSOR 2018**, Pullman City, New Delhi, India, Oct. 28-31, 2018.
8. B. Mandal, Aaryashree, R. Bhardwaj, M. Das, M.T. Htay, D. S. Sharma, S. Mukherjee, “*Defect control in MoO<sub>3</sub> nanostructures as ethanol sensor,*” **IEEE SENSOR 2018**, Pullman City, New Delhi, India, Oct. 28-31, 2018.

# TABLE OF CONTENT

TITLE PAGE.....	i
DECLARATION PAGE.....	ii
ACKNOWLEDGEMENTS.....	iii
DEDICATION PAGE.....	v
LIST OF PUBLICATIONS.....	vi
TABLE OF CONTENT.....	xi
LIST OF FIGURES.....	xv
LIST OF TABLES.....	xix
ACRONYMS.....	xx
NOMENCLATURE.....	xxi
ABSTRACT.....	xxii

## **Chapter 1 Introduction**

1.1. Challenges and Opportunities in Nanotechnology	1
1.2. Nanomaterials: The Boon	2
1.3. Metal Oxide Nanomaterials for Diversity of Applications	3
1.4. Metal Oxide Based Organic-Inorganic Hybrids	4
1.5. Objective and Research Outline	6
1.6. Organization of Thesis	7
1.7. References	7

## **Chapter 2 Materials and Their Properties**

2.1. Zinc Oxide	17
2.2. Graphene Quantum Dots	19
2.2.1. Synthesis of GQDs	20
2.2.2. Properties of Synthesized GQDs	21
2.3. Oligo-( <i>p</i> -phenylenevinylene)	22

2.3.1. Synthesis of OPV	22
2.3.1.1. Materials:	22
2.3.1.2. Synthesis of Oligo(p-phenylenevinylene)(OPV) Conjugated Oligopeptide	23
2.3.2. Properties of Synthesized OPVs	27
2.4. References	27

### **Chapter 3 Fabrication and Characterization Techniques**

3.1. Substrate Selection and Its Cleaning	33
3.1.1. Procedures Employed for Si Substrate Cleaning	34
3.1.2. Procedure Employed for Glass Substrate Cleaning	35
3.2. Fabrication Techniques	35
3.2.1. Dual Ion Beam Sputtering System	35
3.2.2. Electrodeposition System	40
3.3. Characterization Techniques	43
3.3.1. X-Ray Diffraction Measurement	43
3.3.2. Field Emission Scanning Electron Microscopy	45
3.3.3. Energy Dispersive X-Ray Spectroscopy	47
3.3.4. Photoluminescence Measurement System	48
3.3.5. Variable Angle Variable Wavelength Spectroscopic Ellipsometry Measurement System	49
3.3.6. High-Resolution Transmission Electron Microscopy	51
3.3.7. I-V and C-V Measurement System	52
3.4. Device Measurement Set-ups	53
3.4.1. Incident Photon Conversion Efficiency	53
3.4.2. Gas Sensing Set-up	55
3.5. References	56

### **Chapter 4 Photosensitive ZnO-GQD Hybrid Nanocomposite**

4.1. Introduction	59
4.2. Experimental Details	60
4.2.1. Experimental Layout	60
4.2.2. Electrochemical Deposition	62
4.3. Results and Discussions:	63
4.3.1. Voltammogram	63

4.3.2. Morphology and Structure	64
4.3.2.1. FESEM	64
4.3.2.2. X-ray Diffraction	65
4.3.3. Optical Properties	66
4.3.3.1. Photoluminescence	66
4.3.3.2. Current-Voltage (I-V) Characteristics	68
4.3.3.3. Spectroscopic Ellipsometry (SE)	69
4.4. Conclusion	72
4.5. References	73

## **Chapter 5 Devices Based on ZnO-OPV Nanocomposite**

5.1. ZnO-OPV Based Photodetector	82
5.1.1. Introduction	82
5.1.2. Experimental Section	82
5.1.2.1. The Growth of Working Electrodes	82
5.1.2.2. Electrochemical Synthesis	83
5.1.2.3. Synthesis of Thin Film Standards	83
5.1.3. Device Characterization	83
5.1.4. Results and Discussions	84
5.1.4.1. Morphology and Structure	84
5.1.4.2. The Device Structure	86
5.1.4.3. Device performances	86
5.2. ZnO-OPV Based Gas Sensor	92
5.2.1. Introduction	92
5.2.2. Experimental Section	94
5.2.2.1. The Growth of Working Electrodes:	94
5.2.2.2. Electrochemical Synthesis	94
5.2.2.3. Synthesis of Standard Film	95
5.2.2.4. Device Fabrication	95
5.2.3. Device Characterization	95
5.2.4. Results and Discussions	96
5.2.4.1. Morphology and Structure	96
5.2.4.2. Device Performances	97
5.2.4.3. Device Sensing Mechanism	101

5.3. Conclusion	102
5.4. References	103
<b>Chapter 6 Conclusion and Scope for Future Work</b>	<b>111</b>

## LIST OF FIGURES

Figure No.	Figure Title	Page No.
Figure 2.1.	<i>The schematic representation of ZnO (wurtzite) crystal structure.</i>	17
Figure 2.2.	<i>Schematic diagram of ZnO NR showing the growth direction.</i>	18
Figure 2.3.	<i>TEM image of as obtained GQDs.</i>	21
Figure 2.4.	<i>FTIR spectrum of GQDs. GQDs were in the form of KBr pellets, thoroughly dried before mixing with KBr.</i>	21
Figure 2.5.	<i>Synthetic scheme of compound 1 (HO-YY-OPV-YY-OH).</i>	25
Figure 2.6.	<i>Synthesis scheme of compound 2 (HO-OPV-OH).</i>	26
Figure 2.7.	<i>Calculated molecular orbitals for compound 1 at the B3LYP/6-31G** level for C, N, O and H.</i>	27
Figure 3.1.	<i>Actual image of dual ion beam sputtering system.</i>	36
Figure 3.2.	<i>Schematic diagram of dual ion beam sputtering system.</i>	37
Figure 3.3.	<i>Schematic diagram of primary ion beam source.</i>	38
Figure 3.4.	<i>Schematic diagram of assist ion source.</i>	39
Figure 3.5.	<i>The electrochemical cell.</i>	41
Figure 3.6.	<i>The electrodeposition setup by Metrohm (AutoLab).</i>	42
Figure 3.7.	<i>Basic principle of XRD diffraction.</i>	44
Figure 3.8.	<i>Photograph of Rigaku SmartLab, Automated Multipurpose X-Ray Diffractometer.</i>	45
Figure 3.9.	<i>Photograph of FE-SEM and EDX instrument, Zeiss Supra 55.</i>	47
Figure 3.10.	<i>Actual image of Photoluminescence Measurement Setup.</i>	48

Figure 3.11.	<i>Photographic image of Variable Angle Variable Wavelength Spectroscopic Ellipsometry system.</i>	49
Figure 3.12.	<i>Photographic image representation of HRTEM.</i>	50
Figure 3.13.	<i>Photographs of (a) probe station and (b) temperature controller.</i>	52
Figure 3.14.	<i>Images of (a) Keithley 2612A and (b) Keithley 4200A Semiconductor Parameter Analyzer.</i>	53
Figure 3.15.	<i>Photograph of IPCE measurement setup.</i>	54
Figure 3.16.	<i>Gas sensing setup.</i>	55
Figure 4.1.	<i>Layout of the scheme of deposition of the samples, ZnO, GQD and ZnO-GQD.</i>	61
Figure 4.2.	<i>The electrodeposition setup diagram. Here, CE is Counter Electrode, RE is Reference Electrode and WE is Working Electrode.</i>	62
Figure 4.3.	<i>Cyclic voltammogram of GQD</i>	64
Figure 4.4.	<i>a), b), c) FESEM images of ZnO, GQD, and ZnO-GQD nanocomposite, respectively, d) TEM image of GQD individual sample.</i>	64
Figure 4.5.	<i>XRD peaks of ZnO, GQD and ZnO-GQD samples</i>	66
Figure 4.6.	<i>a) Room-temperature PL spectra of ZnO, GQD and ZnO-GQD nanocomposite, b) Raman spectra of ZnO, GQD and ZnO-GQD nanocomposite and c) I-V characteristics of the samples under dark condition and illumination at room temperature. Inset shows the I-V of ZnO and GQD alone.</i>	67
Figure 4.7.	<i>a) n, b) k, c) <math>\Psi</math>, and d) <math>\Delta</math> variation of ZnO, GQDs and ZnO-GQD nanocomposite.</i>	70
Figure 4.8.	<i>Spectral variation of absorption coefficient of ZnO, GQDs and ZnO-GQD nanocomposite as fitted from SE. Inset shows corresponding Tauc's plots.</i>	71
Figure 5.1.	<i>a) FE-SEM of ZnO-OPV hybrid, b) FE-SEM of ZnO-f-OPV hybrid, c) EDX image of ZnO-OPV,</i>	85

	<i>d) EDX image of ZnO-f-OPV, e) XRD pattern of ZnO, ZnO-OPV and ZnO-f-OPV hybrid compared. Asterisk (*) represents some organic phase. f) XRD pattern of ZnO-OPV and ZnO-f-OPV hybrid at a smaller angle showing a lamellar structure of the ZnO-f-OPV hybrid.</i>	
Figure 5.2.	<i>a) Schematic diagram of the fabricated device, b) Energy band diagram of photodetector under zero bias for the device with hybrid nanostructure as sensing (photo-detecting) layer.</i>	86
Figure 5.3.	<i>a) Schematic of IPC System, b) Responsivity of ZnO based detector c) Responsivity of ZnO-f-OPV hybrid based detector d) Responsivity of ZnO-f-OPV hybrid detector compared with ZnO detector at zero bias (responsivity at zero bias is <math>\times 50</math> times multiplied) and at a reverse bias of 20V.</i>	87
Figure 5.4.	<i>a) Comparison of the quantum efficiencies and the specific detectivity of ZnO alone and ZnO-f-OPV hybrid based detectors. b) Comparative analysis of I-V curves of sensing films of ZnO alone and ZnO-f-OPV hybrid.</i>	88
Figure 5.5.	<i>a) Temporal response of ZnO/f-oligophenylenevinylene hybrid at 325 nm and -5 V bias b) charge generation and transport model when UV light is off and when it is on at same bias and wavelength.</i>	90
Figure 5.6.	<i>Schematic diagram of the preparation process for the ZnO-OPV hybrid.</i>	94
Figure 5.7.	<i>a) FESEM image of ZnO-OPV and b) EDX image of ZnO-OPV.</i>	96
Figure 5.8.	<i>XRD images of ZnO and ZnO-OPV. Inset shows the peaks due to formation of lamellar structure.</i>	97

Figure 5.9.	<i>a) Sensing response of ZnO, OPV and ZnO-OPV with varying ppm of ammonia, b) cyclic response of ZnO, OPV and ZnO-OPV at 10 ppm of ammonia, c) single cycle response of ZnO-OPV towards 10 ppm of ammonia showing response time and recovery time, and d) selectivity graph showing selectivity of ZnO-OPV towards ammonia over other analyte gases.</i>	98
Figure 5.10.	<i>Long-term stability of ZnO-OPV at 10 ppm of NH<sub>3</sub>.</i>	100
Figure 5.11.	<i>Schematics of sensing mechanism using the band diagram.</i>	102

## LIST OF TABLES

<b>Table No.</b>	<b>Table Title</b>	<b>Page No.</b>
Table 2.1.	<i>Some basic properties of wurtzite ZnO.</i>	19
Table 4.1.	<i>Deposition parameters for ZnO, GQD and ZnO-GQD.</i>	61
Table 4.2.	<i>Bandgap of the ZnO, GQD and ZnO-GQD nanocomposite as obtained from PL and SE measurements.</i>	72
Table 5.1.	<i>Comparative analysis of sensing properties of various ZnO based organic-inorganic hybrid ammonia sensor.</i>	101

## ACRONYMS

<b>DIBS</b>	<i>Dual Ion Beam Sputtering Deposition</i>
<b>eV</b>	<i>Electron Volt</i>
<b>FE-SEM</b>	<i>Field Emission Scanning Electron Microscopy</i>
<b>FWHM</b>	<i>Full Width at Half Maximum</i>
<b>I-V</b>	<i>Current- Voltage</i>
<b>SE</b>	<i>Spectroscopic Ellipsometry</i>
<b>GZO</b>	<i>Gallium-doped Zinc Oxide</i>
<b>PL</b>	<i>Photoluminescence</i>
<b>SEM</b>	<i>Scanning Electron Microscopy</i>
<b>TCO</b>	<i>Transparent Conducting Oxide</i>
<b>DI</b>	<i>De-Ionized</i>
<b>HRTEM</b>	<i>High Resolution Transmission Electron Microscopy</i>
<b>XRD</b>	<i>X-Ray Diffraction</i>
<b>EDX</b>	<i>Energy Dispersive X-ray</i>
<b>ZnO</b>	<i>Zinc Oxide</i>
<b>GQD</b>	<i>Graphene Quantum Dots</i>
<b>ITO</b>	<i>Indium Tin Oxide</i>
<b>OPV</b>	<i>Oligo(p-phenylenevinylene)</i>
<b>DPC</b>	<i>Deposition Chamber</i>
<b>LLC</b>	<i>Load Lock Chamber</i>
<b>MSE</b>	<i>Mean Square Error</i>
<b>RMS</b>	<i>Root-Mean-Square</i>
<b>HOMO</b>	<i>Highest Occupied Molecular Orbital</i>
<b>LUMO</b>	<i>Lowest Unoccupied Molecular Orbital</i>
<b>ED</b>	<i>Electrodeposition</i>
<b>PD</b>	<i>Photodetector</i>

## NOMENCLATURE

$\Delta E_C$	<i>Conduction Band Offset</i>
$\Delta E_V$	<i>Valence Band Offset</i>
$\eta$	<i>Efficiency</i>
$a, c$	<i>Lattice Constant</i>
$\lambda$	<i>Wavelength</i>
$E_g$	<i>Energy Gap</i>
$\alpha$	<i>Absorption Coefficient</i>
$\theta_B$	<i>Bragg Diffraction Angle</i>
$h\nu$	<i>Photon Energy</i>

## ABSTRACT

# ZnO Based Organic-Inorganic Hybrids: Properties and Device Applications

*by*

**Aaryashree**

Hybrid Nanodevice Research Group, Discipline of Electrical Engineering  
Indian Institute of Technology Indore

Supervisor: Dr. Shaibal Mukherjee

Co-Supervisor: Dr. Apurba K Das

In the current interdisciplinary age of nanotechnology, metal oxide based semiconductors have gained substantial interest. This is mainly because of their applications in various technological areas, such as nanoelectronics, optoelectronics, sensors, etc. One of the most studied metal oxide for potential applications is zinc oxide (ZnO) due to its attractive physical and chemical properties. Also, the material characteristics such as wide bandgap, large surface area to volume ratio, intrinsic *n*-type conductivity, and a large exciton binding energy, have made ZnO an exciting material for various technological applications.

Sensors based on ZnO are generally seen to have high chemical and thermal stability. However, they operate at high temperatures and lack selectivity [1], [2]. Hence, a stable device with high selectivity and high response at room temperature is still the concern of the research community. Interestingly, the synergetic effects between organic and inorganic components have been reported to have improved both properties and performances [3]. Therefore, our main objective is to reduce the drawbacks of ZnO based sensor, i.e. high operating temperature and low selectivity,

by adding an organic moiety to it and making an organic-inorganic hybrid. In this thesis work, two ZnO based hybrid materials are synthesized, characterized and used as the active material for device fabrication.

The summary of the present thesis work, in view of the main objective, is as follows:

- ZnO-graphene quantum dots (GQD) hybrid:
  - *Synthesis:* Synthesis of GQD, ZnO, and ZnO-GQD hybrid.
  - *Characterization:* Study of optical, elemental, electrical, crystalline and morphological properties of the grown thin films (GQD, ZnO, and ZnO-GQD hybrid).
  - *Application:* Enhanced properties for optoelectronic application.
  
- ZnO-oligo(*p*-phenylenevinylene) (OPV) hybrid:
  - *Synthesis:* Synthesis of OPV, ZnO and ZnO-OPV hybrid.
  - *Characterization:* Study of structural, elemental, electrical, morphological and optical properties of the grown thin films (OPV, ZnO and ZnO-OPV hybrid).
  - *Applications:*
    - Fabrication of ZnO-OPV based band-selective UV photodetector.
    - Fabrication of ZnO-OPV based highly selective ammonia gas sensor.

First of all, a comparative analysis has been done on the properties of graphene quantum dots (GQDs) and ZnO-GQD organic-inorganic nanocomposite films, deposited using a simple electrochemical deposition process. The room-temperature photoluminescence (PL) spectra of the ZnO-GQD, GQDs and ZnO structures were studied. The PL peak from ZnO was observed at 380 nm. Electrodeposition process might lead to a

non-uniform film deposition with various intrinsic defects which generally helps in producing a broad emission PL spectrum. ZnO film, primarily grown under oxygen-rich conditions, begets most presumptive intrinsic defects like zinc vacancies, oxygen interstitial or the extrinsic defects like trapped OH<sup>-</sup>, some functional group impurities, etc. With the excitation of 325 nm, GQD exhibits a relatively broader PL peak at 423 nm. These PL peaks are attributed from aromatic  $\pi$ - $\pi$  stacking interactions. ZnO-GQD nanocomposite shows a distinct PL peak at 370 nm and looks similar to the PL peak from ZnO. However, the spectral location of PL peak (380 nm) observed in ZnO film shows a marginal blue shift towards the UV region (~370 nm) in the case of ZnO-GQD nanocomposite. Further, the band gap as obtained from PL was verified using spectroscopic ellipsometry (SE). The current-voltage ( $I$ - $V$ ) characteristics of all three samples showed a similar behaviour of photocurrent variation. Both the dark and the irradiated currents increase linearly with increasing bias voltage. The values of photosensitivity of ZnO, GQD, and ZnO-GQD nanocomposite were found to be 6.77, 51, and 99.32, respectively at room temperature. Further, in the perspective of device fabrication, the hybrids containing conjugated organic moiety have been exploited in areas such as photodetectors, transistors, sensors, etc. Blending organic molecules with the inorganic network is seen to offer extra benefits such as tuning the optical spectra, the lifetime of trap states, sensitivity and response time. Sensitivity can be optimized by controlling the structure of nano-hybrids to maximize the density of organics bound to the inorganic surface and also minimize the turbulence and discontinuities in conduction through the permeating network. This perspective inspired us to accomplish our goal of synthesizing self-assembled hybrid nanostructures having both electronically active organic (*i.e.* OPV) and inorganic (ZnO) components. Hence, a hybrid photodetector containing ZnO and functionalized OPV was fabricated, which was deposited electrochemically onto an ITO-coated glass electrode. X-ray diffraction (XRD) results revealed the lamellar structure of the conjugates. As photodetectors, room temperature responsivity as high as 0.2 AW<sup>-1</sup> at 330 nm with a bias of -20 V, the

maximum external quantum efficiency of 75% at -20 V bias was observed. When the ZnO-OPV hybrid photodetector device was illuminated with a wavelength of 325 nm, excitons are generated in both OPV and ZnO. On externally applying a bias, these photo-generated excitons in ZnO or OPV dissociate at various interfaces formed between the oligomer and ZnO inside the bulk and thus form a complimentary trajectory for the electrons from oligomer to transfer onto ZnO and holes to transfer onto OPV. However, both the rise and fall time of the response were approximately 0.8 s, indicating average photoresponse characteristics. Most likely, the charge trapping at the grain boundaries of the hybrid film is detrimental to the device performance. Also, the presence of deep traps, which have longer charge release times, renders the device sluggish. Furthermore, to check the stability of the devices, the devices were exposed to air and kept in room ambience for eleven months, but no visible change in device performance was observed.

Additionally, an electrochemically deposited hybrid ammonia gas sensor containing ZnO and OPV was fabricated. As a gas sensor, the response as high as 8.83 at 10 ppm of ammonia have been observed. Also, the excellent selectivity and the response time and recovery time of 9.8 s and 17.3 s, respectively, at room temperature can effectuate forthcoming high-performance hybrid gas sensor which could be cost-effective and environmentally benign. The sensing responses of the three sensors viz. OPV, ZnO and ZnO-OPV sensors were measured by exposing them to different concentrations of NH<sub>3</sub> gas at room temperature. It is seen that, among the three sensors, Zn-OPV sensor shows the best response. For the ZnO and the OPV sensors, the responses at all the concentrations are almost similar, i.e., they do not change much. However, in the case of ZnO-OPV sensor, the change in response to the change in concentration is quite noticeable. Also, it is very clear from the results that the response of the ZnO-OPV sensor to lower concentrations of ammonia is much higher than that of bare ZnO and OPV based sensor. This implies that ZnO-OPV can be used even for sensing the lower concentrations of NH<sub>3</sub> gas. High selectivity is most desirable parameters for a gas sensor to be practically valuable. Therefore, the room temperature selectivity of the ZnO-OPV thin

film towards various toxic gases such as hydrogen sulphide, carbon dioxide, and carbon monoxide was studied. The responses were 1 to 100 ppm H<sub>2</sub>S, 0.1 to 1000 ppm CO<sub>2</sub>, and 0.2 to 100 ppm CO, respectively, as compared 8.83 to 10 ppm of NH<sub>3</sub>. In hydrated state (in the presence of humidity), the ionic mobility across the peptide bonds arises due to the H<sup>+</sup> transfer from -NHCO- to -N-COH- via the hydrogen bonding with water. The H<sup>+</sup> transfer becomes restricted in the presence of NH<sub>3</sub> due to the formation of [NH<sub>3</sub>...H<sub>2</sub>O] complex formation. As a consequence, H<sup>+</sup> transfer across the peptide molecules become hindered, and resistance increases along the organic layer. Although, the exact reason for the high selectivity of ZnO-OPV towards ammonia is not clear, yet, the reason that might account for the excellent selectivity is: ammonia has a strong electron donating ability due to the presence of a lone electron pair, and thus it can readily donate the unpaired electrons. The sensing layer, consisting of the *p*-type OPV might have a higher binding affinity for the electron-donating ammonia. Hence, the electrons get transferred to the sensing layer, which may lead to a significant change in resistance. Also, the self-assembly of OPV and ZnO provides a continuous path for charge transfer, thus, providing a faster response.

The major contributions of the work can be summarily concluded as below.

- A simple and facile methodology, i.e. electrodeposition is demonstrated for synthesizing GQD and ZnO-GQD nanocomposite films. The study showed improved properties of the ZnO-GQD hybrid nanocomposites film over pure organic GQD and inorganic ZnO film.
- The ZnO-OPV hybrid photodetector is demonstrated for the first time in literature. The photoresponse and external quantum efficiency of the nanohybrid photodetector were measured at different bias voltages and reached 0.2 A W<sup>-1</sup> and 75.5%, respectively, at -20 V. These experimental findings indicate that the hybrid nanostructure of ZnO-OPV may be especially well suited for the use in high-performance nanoscale photodetectors.

- Sensors with sensing layers made up of OPV, ZnO and ZnO-OPV composites are successfully synthesized by electrochemical deposition. The composite based sensor exhibited the highest response of 8.83 to 10 ppm of NH<sub>3</sub>. It showed an excellent selectivity to NH<sub>3</sub> among various test gases.

# Chapter 1

## Introduction

### 1.1. Challenges and Opportunities in Nanotechnology

Nanotechnology is a rapidly growing technology with an enormous potential to develop novel materials with remarkable properties leading to new, innovative and enriched products for various applications. Numerous nano-based products such as electronics, personal care products, sporting goods, and automotive parts, have already flooded the marketplace. However, there are many concerns about the impact of nanomaterials on both human health and the environment [1].

Although the term “nanotechnology”, coined by the Japanese scientist Norio Taniguchi, dates back to 1974 to describe precision processes in semiconductor engineering [2], Richard Feynman, for the first time, seeded the idea of creating, manipulating, and controlling materials on a small scale in his famous talk “There’s Plenty of Room at the Bottom” in 1959 [3]. Later, the 80s saw the concepts of nanotechnology becoming popular owing to the invention of new nano-characterization tools such as scanning tunneling microscope (STM), atomic force microscope (AFM), etc. which enabled the study and manipulation of nanomaterials. The discovery of the fullerene in 1985 [4] and the rediscovery of carbon nanotubes in 1991 [5] marked the turning point of research around the world. The research and development in nanotechnology fields are greatly influenced by the fabrication of new nanomaterials with improved properties. These nanomaterials are designed to meet our increasing demands for renewable clean energy, advanced drug delivery systems, bio-monitoring devices, green lighting technologies, and ultra-fast computing architectures, etc.

## 1.2. Nanomaterials: The Boon

Nanotechnology is exploited to determine, manipulate, or integrate materials with at least one dimension between 1 and 100 nm. Such materials retain properties that are different from their bulk counterparts. At the nano-scale range, the nanomaterials may exhibit different physical and chemical properties owing to the specific particle size. For example, quantum dots which are an assembly of atoms with the size of about 5- 10 nm, emit different colors by just varying the dot size. As the material size shrinks, the surface area to volume ratio significantly increases to the level that the material properties are determined by the surface properties. This large surface area/volume ratio offers distinctive properties that have wide-ranging applications in numerous industrial sectors, including medical, electronics, and chemical sectors. Varieties of new and stimulating nanomaterials have been synthesized in the last two decades, which include quantum dots and nanoparticles [4]–[7] as examples of zero dimension nano entities. Likewise, nanotubes, and nanowires, nanorods are examples of one dimension (1D) nanomaterials, while graphene sheet is classified as a two-dimension (2D) nanomaterial [8]–[12]. In the case of three dimensional (3D) nanomaterials, there is a huge number of reported structures, such as nanodandelion [13]–[15], nanoflowers [16]–[18], and hyperbranched nanostructures (NSs) [19], [20].

Likewise, combining the unique properties of two or more nanomaterials to benefit from their individual properties has led to nanocomposites that have further enhanced the material properties [21]–[23]. For example, due to their high electrical conductivity carbon nanotubes have the potential for the manufacturing of low-cost solar cells [24], electronics [24]–[26] and anti-static composite materials [27]. Metallic silver (Ag) and gold (Au) nanoparticles have been found to be very effective as an anti-bacterial agent [28], [29] and effective catalysts for several chemical reactions under room temperature [30], [31]. While metal oxides such as titanium dioxide ( $\text{TiO}_2$ ) nanoparticles having a large band gap and hence have proven to be an excellent candidate for

photocatalysis, UV protection, photovoltaics, and sensing [32]–[35]. Also, TiO<sub>2</sub> nanomaterials have been used to cover exterior walls of buildings to offer self-cleaning surfaces, as this nanomaterial exhibits super-hydrophilicity under solar irradiation [36], [37]. Another example is cerium oxide (CeO<sub>2</sub>) which can be applied as a diesel fuel combustion catalyst [38], [39], which reduces fuel consumption, carbon monoxide emission, and other exhausts. The last example is semiconductor quantum dots which as mentioned above can emit different color depending on their particle size; this property enables them to be used in applications such as bio-labeling [40], chemical sensing, [41] light display [41], etc. Thus, the research and development of nanomaterials represent the driving force for many nanotechnology sectors, however, for this new technology to revolutionize the way we live today, tremendous efforts are required to fully understand the basic properties, applications, and functionalities of these nanomaterials. Additionally, the assessment of their impact on human and environment has to be fully understood.

### **1.3. Metal Oxide Nanomaterials for Diversity of Applications**

In the current interdisciplinary age of nanotechnology, the metal oxide semiconductor nanomaterials have gained substantial interest due to their promising applications in a diversity of technological areas, such as electronics, optoelectronics, bio/chemical sensors, coating systems, and catalysis. One of the most studied metal oxide nanomaterials for potential applications is TiO<sub>2</sub> due to its wide band gap and photocatalytic activity as well as sensitivity. As mentioned before TiO<sub>2</sub> nanoparticles have been applied as self-cleaning and anti-fogging coatings for exterior walls and windows of buildings using the concept of super-hydrophilicity [36]. Furthermore, UV irradiation of tiles covered with TiO<sub>2</sub>:Cu have shown to function well for self-sterilization application [42]. Also, TiO<sub>2</sub> nanowires have been proposed as a possible candidate for advanced batteries with better storage and fast charging/discharging capabilities [43] Another example of an oxide nanomaterial that has

received vast attention is zinc oxide (ZnO) which is one of the most promising metal oxides due to its attractive physical and chemical properties. ZnO has a unique ability to demonstrate both semiconducting and piezoelectric characteristics simultaneously, which can have numerous applications in energy harvesting domains for small devices such as cell phones [44]. The synthesis of ZnO nanomaterials has resulted in a plentiful number of NSs such as nanowires, nanotubes as examples of 1D nanomaterials [45], [46] nanosheets, nanowalls, and nanoplates as a 2D structures [47]–[50]. The 3D ZnO NSs include nanoflowers and other complex structures such as nanotetrapods [51], [52]. All these nanofeatures of ZnO have developed increasing attention in broad spreading research areas for applications in electronics, optoelectronics, and sensing. Material characteristics such as wide bandgap, large surface area to volume ratio, intrinsic *n*-type conductivity, and a large number of native point defects as will be discussed in the next chapter, render ZnO nanomaterials to be exciting material for diverse technological applications. These applications include transparent conductors as a low-cost replacement of indium tin oxide (ITO) in applications such as displays and photovoltaics panels. ZnO has been explored for fabrication of inexpensive disposable electronics such as multisource energy converter[51] and light emitting diodes (LED) [51]. Also, ZnO nanomaterials have found resurgent attention in areas such as bio/chemical sensing owing to their relatively large surface/volume ratio as well as their high ionicity, biocompatibility, and non-toxicity combined with the conductive nature which enables enhanced analytical and sensitivity performances [53]. One of the most urgent challenges is the realization of repeatable and stable *p*-type conductivity of ZnO which is very critical for electronics and photonics applications.

#### **1.4. Metal Oxide Based Organic-Inorganic Hybrids**

The possibility of combining the properties of organic and inorganic compounds in a unique material is an old challenge that started with the beginning of the industrial era. Some of the oldest and most famous

organic-inorganic hybrids come from the paint industries, where inorganic pigments were suspended in organic mixtures. While the concept of 'hybrid' materials was not mentioned at that time, the wide increase of work on organic-inorganic structures continued with the development of the polymer industry. Inorganic fillers were added to polymers to improve some of the properties of the compounds. The concept of 'hybrid organic-inorganic' materials emerged only very recently, when the research shifted to more sophisticated materials with a higher added value.

Inorganic compounds (such as  $\text{TiO}_2$ ,  $\text{SnO}_2$ ,  $\text{ZnO}$ , etc.) behave generally high chemical and thermal stability that allows their application under different operating conditions, and they can be obtained by cheap processes and be easily deposited in thin or thick film form by different techniques. Organic compounds are characterized by a synthetic versatility and reactivity, which makes it possible to modulate the molecular structure of the sensing materials to achieve desired property [54], [55]. Additionally, the organic sensing materials such as conducting polymers (polyaniline (PANI), polypyrrole (PPy), and polythiophene (PTP), etc.) can show a response at room temperature or low temperature, which has a convenient operating and attractive prospect [56]–[59]. Nevertheless, the drawbacks for single inorganic or single organic sensing materials, namely, high operating temperature and low selectivity for inorganic sensing materials, and poor chemical stability and mechanical strength for organic sensing materials, could restrict their practical application.

The researches have proved that the mechanical strength and chemical stability can be enhanced by the addition of inorganic particles into the organic materials to form hybrids [60]–[64]. Therefore, in the past decades, the organic/inorganic hybrid materials with different combinations of the two components, expected to obtain new kind composite materials with synergetic or complementary behaviors, have received more and more attention worldwide and become attractive for many new electronic, optical, magnetic or catalytic applications since

their properties or performances can be improved, considering the possibility to combine the advantages of organic and inorganic counterparts. Numerous reports have been published based on the organic/inorganic hybrid sensing materials for the applications in gas sensors, humidity sensors, ultraviolet sensors, strain sensors, and other sensors [65]–[67].

## 1.5. Objective and Research Outline

The main focus of this thesis is devoted to the development of ZnO based hybrid materials and to assess their potentials in areas such as optoelectronic applications, photodetectors, and gas sensing applications.

The general objectives and outcomes of this thesis work can be summarized as follows:

- ZnO-Graphene Quantum Dots (GQD) hybrid:
  - *Synthesis:* Synthesis of GQD, ZnO, and ZnO-GQD hybrid.
  - *Characterization:* Study of optical, elemental, electrical, crystalline and morphological properties of the grown thin films (GQD, ZnO, and ZnO-GQD hybrid).
  - *Application:* Enhanced properties for the optoelectronic application.
- ZnO-Oligo(*p*-phenylenevinylene) (OPV) hybrid:
  - *Synthesis:* Synthesis of OPV, ZnO and ZnO-OPV hybrid.
  - *Characterization:* Study of structural, elemental, electrical, morphological and optical properties of the grown thin films (OPV, ZnO and ZnO-OPV hybrid).
  - *Applications:*
    - Fabrication of ZnO-OPV based band-selective ultraviolet (UV) photodetector.
    - Fabrication of ZnO-OPV based highly selective ammonia gas sensor.

## 1.6. Organization of Thesis

*Chapter 1* summarises an introduction to metal oxide based composite nanomaterials for diverse applications and discusses the background of the prior work in the field of realization of organic-inorganic based hybrid devices.

*Chapter 2* demonstrates a summarising description of basic properties of ZnO, ZnO-GQD and ZnO-OPV composites, and their advantages for the realization of sensing devices and discusses the background of the prior work in the field of realisation of composite-based sensing devices.

*Chapter 3* describes the deposition and characterization systems employed for fabricating and probing ZnO based organic-inorganic hybrid composite structure. Autolab, dual ion beam sputtering system, field-emission scanning electron microscope, X-ray diffraction, variable-angle-variable-wavelength spectroscopic ellipsometry, four probe hall measurement technique, semiconductor parameter analyzer 4200A, energy dispersive X-ray spectroscopy, and high-resolution transmission electron microscopy are the major systems used for this work.

*Chapter 4* describes the synthesis of stable ZnO and GQD based nanocomposite and its detailed properties for the optoelectronic application.

*Chapter 5* describes the realization of ZnO-OPV based devices. Photodetector and gas sensors are the two main devices discussed in this chapter. The response and stability of these sensing devices are elaborately explained.

*Chapter 6* concludes the thesis and proposes the scope for future works for the continuation of the research.

## 1.7. References

[1] C. Buzea, I. I. Pacheco, and K. Robbie, "Nanomaterials and

- nanoparticles: Sources and toxicity,” *Biointerphases*, vol. 2, no. 4, pp. MR17-MR71, Dec. 2007.
- [2] R. W. Whatmore, “Nanotechnology—what is it? Should we be worried?,” *Occup. Med. (Chic. Ill.)*, vol. 56, no. 5, pp. 295–299, Aug. 2006.
- [3] W. A. Goddard III, D. Brenner, S. E. Lyshevski, and G. J. Iafrate, *Handbook of nanoscience, engineering, and technology*. 2007.
- [4] T. S. Ahmadi, Z. L. Wang, T. C. Green, A. Henglein, and M. A. El-Sayed, “Shape-Controlled Synthesis of Colloidal Platinum Nanoparticles,” *Science*, vol. 272, no. 5270, pp. 1924–1925, Jun. 1996.
- [5] C. Wang, H. Daimon, T. Onodera, T. Koda, and S. Sun, “A general approach to the size- and shape-controlled synthesis of platinum nanoparticles and their catalytic reduction of oxygen,” *Angew. Chemie - Int. Ed.*, vol. 47, no. 19, pp. 3588–3591, Apr. 2008.
- [6] N. Saravanan, S. Ponnusamy, S. Shri Prasad, and V. Joseph, “Synthesis and characterization of SnO<sub>2</sub> quantum dots,” *Int. J. ChemTech Res.*, vol. 6, no. 1, pp. 600–603, May 2014.
- [7] W. K. Bae, K. Char, H. Hur, and S. Lee, “Single-step synthesis of quantum dots with chemical composition gradients,” *Chem. Mater.*, vol. 20, no. 2, pp. 531–539, Jan. 2008.
- [8] A. K. Geim, “Graphene: Status and prospects,” *Science*, vol. 324, no. 5934, pp. 1530–1534, Jun. 2009.
- [9] A. K. Geim and K. S. Novoselov, “The rise of graphene,” *Nat. Mater.*, vol. 6, no. 3, pp. 183–191, Mar. 2007.
- [10] A. Gole and C. J. Murphy, “Seed-Mediated Synthesis of Gold Nanorods: Role of the Size and Nature of the Seed,” *Chem. Mater.*, vol. 16, no. 19, pp. 3633–3640, Sep. 2004.

- [11] D. Bekermann, A. Gasparotto, D. Barreca, A. Devi, R. A. Fischer, M. Kete, U. L. Štangar, O. I. Lebedev, C. Maccato, E. Tondello, and G. van Tendeloo, “ZnO nanorod arrays by plasma-enhanced CVD for light-activated functional applications,” *ChemPhysChem*, vol. 11, no. 11, pp. 2337–2340, Jun. 2010.
- [12] J. Y. Park, D. J. Lee, and S. S. Kim, “Size control of ZnO nanorod arrays grown by metalorganic chemical vapour deposition,” *Nanotechnology*, vol. 16, no. 10, pp. 2044–2047, Oct. 2005.
- [13] H. Chen, E. Kern, C. Ziegler, and A. Eychmüller, “Ultrasonically assisted synthesis of 3D hierarchical silver microstructures,” *J. Phys. Chem. C*, vol. 113, no. 44, pp. 19258–19262, Nov. 2009.
- [14] Y. Qin, Y. Song, N. Sun, N. Zhao, M. Li, and L. Qi, “Ionic liquid-assisted growth of single-crystalline dendritic gold nanostructures with a three-fold symmetry,” *Chem. Mater.*, vol. 20, no. 12, pp. 3965–3972, Jun. 2008.
- [15] G. Lu, C. Li, and G. Shi, “Synthesis and characterization of 3D dendritic gold nanostructures and their use as substrates for surface-enhanced Raman scattering,” *Chem. Mater.*, vol. 19, no. 14, pp. 3433–3440, 2007.
- [16] O. V. Kharissova and B. I. Kharisov, “Less-common nanostructures in the forms of vegetation,” *Ind. Eng. Chem. Res.*, vol. 49, no. 22, pp. 11142–11169, Nov. 2010.
- [17] Y. Luo, G. Chang, W. Lu, and X. Sun, “Synthesis and characterization of CuInS<sub>2</sub> nanoflowers,” *Colloid J.*, vol. 72, no. 2, pp. 282–285, Apr. 2010.
- [18] B. Su, G. Wu, C. J. Yang, Z. Zhuang, X. Wang, X. Chen, and X. Chen, “Platinum nanoflowers supported on graphene oxide nanosheets: Their green synthesis, growth mechanism, and advanced electrocatalytic properties for methanol oxidation,” *J.*

Mater. Chem., vol. 22, no. 22, pp. 11284–11289, May 2012.

- [19] A. G. Kanaras, C. Sönnichsen, H. Liu, and A. P. Alivisatos, “Controlled synthesis of hyperbranched inorganic nanocrystals with rich three-dimensional structures,” *Nano Lett.*, vol. 5, no. 11, pp. 2164–2167, 2005.
- [20] Z. Khan, T. R. Chetia, and M. Qureshi, “Rational design of hyperbranched 3D heteroarrays of SrS/CdS: Synthesis, characterization and evaluation of photocatalytic properties for efficient hydrogen generation and organic dye degradation,” *Nanoscale*, vol. 4, no. 11, pp. 3543–3550, May 2012.
- [21] H. Kim, M. Achermann, L. P. Balet, J. A. Hollingsworth, and V. I. Klimov, “Synthesis and characterization of Co/CdSe core/shell nanocomposites: Bifunctional magnetic-optical nanocrystals,” *J. Am. Chem. Soc.*, vol. 127, no. 2, pp. 544–546, 2005.
- [22] C. L. Chiang and R. C. Chang, “Synthesis, characterization and properties of novel self-extinguishing organic-inorganic nanocomposites containing nitrogen, silicon and phosphorus via sol-gel method,” *Compos. Sci. Technol.*, vol. 68, no. 14, pp. 2849–2857, Nov. 2008.
- [23] J. T. Moore, “Semiconductor/Ceramic Nanocomposites: Synthesis, Characterization, and Properties,” in *Encyclopedia of Inorganic and Bioinorganic Chemistry*, Chichester, UK: John Wiley & Sons, Ltd, 2011.
- [24] D. M. Guldi, G. M. A. Rahman, M. Prato, N. Jux, S. Qin, and W. Ford, “Single-wall carbon nanotubes as integrative building blocks for solar-energy conversion,” *Angew. Chemie - Int. Ed.*, vol. 44, no. 13, pp. 2015–2018, Mar. 2005.
- [25] A. Javey, J. Guo, Q. Wang, M. Lundstrom, and H. Dai, “Ballistic carbon nanotube field-effect transistors,” *Nature*, vol. 424, no.

6949, pp. 654–657, Aug. 2003.

- [26] Y. J. Lee, H. Yi, W. J. Kim, K. Kang, D. S. Yun, M. S. Strano, G. Ceder, and A. M. Belcher, “Fabricating genetically engineered high-power lithium-ion batteries using multiple virus genes,” *Science*, vol. 324, no. 5930, pp. 1051–1055, May 2009.
- [27] Z. Li, G. Luo, F. Wei, and Y. Huang, “Microstructure of carbon nanotubes/PET conductive composites fibers and their properties,” *Compos. Sci. Technol.*, vol. 66, no. 7–8, pp. 1022–1029, Jun. 2006.
- [28] A. Rai, A. Prabhune, and C. C. Perry, “Antibiotic mediated synthesis of gold nanoparticles with potent antimicrobial activity and their application in antimicrobial coatings,” *J. Mater. Chem.*, vol. 20, no. 32, pp. 6789–6798, Aug. 2010.
- [29] J. S. Kim, E. Kuk, K. N. Yu, J. H. Kim, S. J. Park, H. J. Lee, S. H. Kim, Y. K. Park, Y. H. Park, C. Y. Hwang, Y. K. Kim, Y. S. Lee, D. H. Jeong, and M. H. Cho, “Antimicrobial effects of silver nanoparticles,” *Nanomedicine Nanotechnology, Biol. Med.*, vol. 3, no. 1, pp. 95–101, Mar. 2007.
- [30] Z. J. Jiang, C. Y. Liu, and L. W. Sun, “Catalytic properties of silver nanoparticles supported on silica spheres,” *J. Phys. Chem. B*, vol. 109, no. 5, pp. 1730–1735, 2005.
- [31] X. Zhou, W. Xu, G. Liu, D. Panda, and P. Chen, “Size-dependent catalytic activity and dynamics of gold nanoparticles at the single-molecule level,” *J. Am. Chem. Soc.*, vol. 132, no. 1, pp. 138–146, Jan. 2010.
- [32] R. Rella, J. Spadavecchia, M. G. Manera, S. Capone, A. Taurino, M. Martino, A. P. Caricato, and T. Tunno, “Acetone and ethanol solid-state gas sensors based on TiO<sub>2</sub> nanoparticles thin film deposited by matrix assisted pulsed laser evaporation,” *Sensors*

Actuators, *B Chem.*, vol. 127, no. 2, pp. 426–431, Nov. 2007.

- [33] S. Günes, N. Marjanovic, J. M. Nedeljkovic, and N. S. Sariciftci, “Photovoltaic characterization of hybrid solar cells using surface modified TiO<sub>2</sub> nanoparticles and poly(3-hexyl)thiophene,” *Nanotechnology*, vol. 19, no. 42, p. 424009, Oct. 2008.
- [34] A. P. Popov, A. V. Priezzhev, J. Lademann, and R. Myllylä, “TiO<sub>2</sub> nanoparticles as an effective UV-B radiation skin-protective compound in sunscreens,” *J. Phys. D. Appl. Phys.*, vol. 38, no. 15, pp. 2564–2570, Aug. 2005.
- [35] W. Pingxiao, T. Jianwen, and D. Zhi, “Preparation and photocatalysis of TiO<sub>2</sub> nanoparticles doped with nitrogen and cadmium,” *Mater. Chem. Phys.*, vol. 103, no. 2–3, pp. 264–269, Jun. 2007.
- [36] A. Fujishima, X. Zhang, and D. A. Tryk, “TiO<sub>2</sub> photocatalysis and related surface phenomena,” *Surf. Sci. Rep.*, vol. 63, no. 12, pp. 515–582, Dec. 2008.
- [37] B. Huang and S. Saka, “Photocatalytic activity of TiO<sub>2</sub> crystallite-activated carbon composites prepared in supercritical isopropanol for the decomposition of formaldehyde,” *J. Wood Sci.*, vol. 49, no. 1, pp. 79–85, 2003.
- [38] B. Park, K. Donaldson, R. Duffin, L. Tran, F. Kelly, I. Mudway, J. P. Morin, R. Guest, P. Jenkinson, Z. Samaras, M. Giannouli, H. Kouridis, and P. Martin, “Hazard and risk assessment of a nanoparticulate cerium oxide-based diesel fuel additive - A case study,” *Inhal. Toxicol.*, vol. 20, no. 6, pp. 547–566, Jan. 2008.
- [39] V. Sajith, C. B. Sobhan, and G. P. Peterson, “Experimental investigations on the effects of cerium oxide nanoparticle fuel additives on biodiesel,” *Adv. Mech. Eng.*, vol. 2010, p. 581407, Jan. 2010.

- [40] C. A. J. Lin, T. Liedl, R. A. Sperling, M. T. Fernández-Argüelles, J. M. Costa-Fernández, R. Pereiro, A. Sanz-Medel, W. H. Chang, and W. J. Parak, “Bioanalytics and biolabeling with semiconductor nanoparticles (quantum dots),” *J. Mater. Chem.*, vol. 17, no. 14, pp. 1343–1346, Mar. 2007.
- [41] M. F. Frasco and N. Chaniotakis, “Semiconductor Quantum Dots in Chemical Sensors and Biosensors,” *Sensors*, vol. 9, no. Figure 1, pp. 7266–7286, Sep. 2009.
- [42] G. B. Smith, C. G. Granqvist, and C. R. C. Press, *Green Nanotechnology: Solutions for Sustainability and Energy in the Built Environment*, vol. 5. CRC Press, 2011.
- [43] A. S. Aricò, P. Bruce, B. Scrosati, J.-M. Tarascon, and W. Van Schalkwijk, “Nanostructured materials for advanced energy conversion and storage devices,” in *Materials for Sustainable Energy*, Co-Published with Macmillan Publishers Ltd, UK, 2010, pp. 148–159.
- [44] Z. L. Wang and J. Song, “Piezoelectric nanogenerators based on zinc oxide nanowire arrays,” *Science*, vol. 312, no. 5771, pp. 242–6, Apr. 2006.
- [45] L. E. Greene, M. Law, J. Goldberger, F. Kim, J. C. Johnson, Y. Zhang, R. J. Saykally, and P. Yang, “Low- Temperature Wafer-Scale Production of ZnO Nanowire Arrays,” *Angew. Chemie*, vol. 115, no. 26, pp. 3139–3142, Jul. 2003.
- [46] S. Xu and Z. L. Wang, “One-dimensional ZnO nanostructures: Solution growth and functional properties,” *Nano Res.*, vol. 4, no. 11, pp. 1013–1098, Nov. 2011.
- [47] W. Zhao, X. Song, Z. Yin, C. Fan, G. Chen, and S. Sun, “Self-assembly of ZnO nanosheets into nanoflowers at room temperature,” *Mater. Res. Bull.*, vol. 43, no. 11, pp. 3171–3176,

Nov. 2008.

- [48] Z. Jing and J. Zhan, "Fabrication and gas-sensing properties of porous ZnO nanoplates," *Adv. Mater.*, vol. 20, no. 23, pp. 4547–4551, Dec. 2008.
- [49] M. M. Brewster, M. Y. Lu, S. K. Lim, M. J. Smith, X. Zhou, and S. Gradak, "The growth and optical properties of ZnO nanowalls," *J. Phys. Chem. Lett.*, vol. 2, no. 15, pp. 1940–1945, Aug. 2011.
- [50] J. H. Park, H. J. Choi, Y. J. Choi, S. H. Sohn, and J. G. Park, "Ultrawide ZnO nanosheets," *J. Mater. Chem.*, vol. 14, no. 1, pp. 35–36, Dec. 2004.
- [51] G. Amin, S. Zaman, A. Zainelabdin, O. Nur, and M. Willander, "ZnO nanorods-polymer hybrid white light emitting diode grown on a disposable paper substrate," *Phys. status solidi - Rapid Res. Lett.*, vol. 5, no. 2, pp. 71–73, Feb. 2011.
- [52] D. Liu, W. Wu, Y. Qiu, S. Yang, S. Xiao, Q.-Q. Wang, L. Ding, and J. Wang, "Surface Functionalization of ZnO Nanotetrapods with Photoactive and Electroactive Organic Monolayers," *Langmuir*, vol. 24, no. 9, pp. 5052–5059, May 2008.
- [53] M. H. Asif, S. M. U. Ali, O. Nur, M. Willander, C. Brännmark, P. Strålfors, U. H. Englund, F. Elinder, and B. Danielsson, "Functionalised ZnO-nanorod-based selective electrochemical sensor for intracellular glucose," *Biosens. Bioelectron.*, vol. 25, no. 10, pp. 2205–2211, Jun. 2010.
- [54] S. Nardis, D. Monti, C. Di Natale, A. D'Amico, P. Siciliano, A. Forleo, M. Epifani, A. Taurino, R. Rella, and R. Paolesse, "Preparation and characterization of cobalt porphyrin modified tin dioxide films for sensor applications," *Sensors Actuators B Chem.*, vol. 103, no. 1–2, pp. 339–343, Sep. 2004.
- [55] N. Parvatikar, S. Jain, S. Khasim, M. Revansiddappa, S. V.

- Bhoraskar, and M. V. N. A. Prasad, "Electrical and humidity sensing properties of polyaniline/WO<sub>3</sub> composites," *Sensors Actuators B Chem.*, vol. 114, no. 2, pp. 599–603, Apr. 2006.
- [56] D. Tyler McQuade, A. E. Pullen, and T. M. Swager, "Conjugated polymer-based chemical sensors," *Chem. Rev.*, vol. 100, no. 7, pp. 2537–2574, 2000.
- [57] D. W. Hatchett and M. Josowicz, "Composites of intrinsically conducting polymers as sensing nanomaterials," *Chem. Rev.*, vol. 108, no. 2, pp. 746–769, 2008.
- [58] J. Huang and R. B. Kaner, "A General Chemical Route to Polyaniline Nanofibers," *J. Am. Chem. Soc.*, vol. 126, no. 3, pp. 851–855, Jan. 2004.
- [59] A. Riul, A. M. G. Soto, S. V. Mello, S. Bone, D. M. Taylor, and L. H. C. Mattoso, "An electronic tongue using polypyrrole and polyaniline," *Synth. Met.*, vol. 132, no. 2, pp. 109–116, Jan. 2003.
- [60] A. S. Subbiah, A. Halder, S. Ghosh, N. Mahuli, G. Hodes, and S. K. Sarkar, "Inorganic hole conducting layers for perovskite-based solar cells," *J. Phys. Chem. Lett.*, vol. 5, no. 10, pp. 1748–1753, 2014.
- [61] D. S. Chung, Y.-H. Kim, and J.-S. Lee, "Achieving high sensitivity in hybrid photodetectors based on an organic single crystal and an inorganic nanocrystal array," *Nanotechnology*, vol. 25, no. 3, p. 035202, Jan. 2014.
- [62] D. Shao, M. Yu, H. Sun, G. Xin, J. Lian, and S. Sawyer, "High-Performance Ultraviolet Photodetector Based on Organic–Inorganic Hybrid Structure," *ACS Appl. Mater. Interfaces*, vol. 6, no. 16, pp. 14690–14694, Aug. 2014.
- [63] S. Mridha and D. Basak, "ZnO/polyaniline based inorganic /organic hybrid structure: Electrical and photoconductivity

- properties,” *Appl. Phys. Lett.*, vol. 92, no. 14, p. 142111, Apr. 2008.
- [64] L. E. Greene, M. Law, B. D. Yuhas, and P. Yang, “ZnO–TiO<sub>2</sub> Core–Shell Nanorod/P3HT Solar Cells,” *J. Phys. Chem. C*, vol. 111, no. 50, pp. 18451–18456, Dec. 2007.
- [65] M. Xu, J. Zhang, S. Wang, X. Guo, H. Xia, Y. Wang, S. Zhang, W. Huang, and S. Wu, “Gas sensing properties of SnO<sub>2</sub> hollow spheres/polythiophene inorganic-organic hybrids,” *Sensors Actuators, B Chem.*, vol. 146, no. 1, pp. 8–13, 2010.
- [66] H. Tai, Y. Jiang, G. Xie, J. Yu, and X. Chen, “Fabrication and gas sensitivity of polyaniline–titanium dioxide nanocomposite thin film,” *Sensors Actuators B Chem.*, vol. 125, no. 2, pp. 644–650, Aug. 2007.
- [67] H.-G. Li, G. Wu, M.-M. Shi, L.-G. Yang, H.-Z. Chen, and M. Wang, “ZnO/poly(9,9-dihexylfluorene) based inorganic/organic hybrid ultraviolet photodetector,” *Appl. Phys. Lett.*, vol. 93, no. 15, p. 153309, Oct. 2008.

# Chapter 2

## Materials and Their Properties

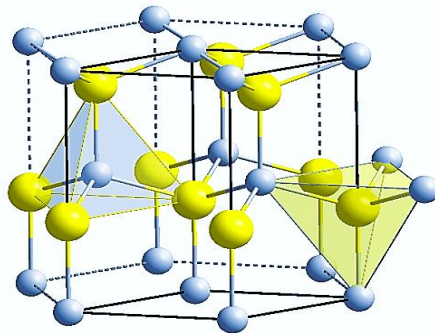
ZnO is a wide bandgap material possessing many interesting properties and probably the richest family of nanostructures. Also, it has been employed to form numerous organic-inorganic hybrids for innumerable applications. In this chapter, we aim to narrate some properties of ZnO comprehensively, as well as discuss the polymers which are used in this work.

### 2.1. Zinc Oxide

Zinc oxide (ZnO) is a metal oxide semiconductor with wurtzite structure under ambient condition. The wurtzite structure has hexagonal unit cell as shown in Figure 2.1. In this crystal structure, two interpenetrating hexagonal-close-pack (hcp) sublattices are alternatively stacks along the c-axis. One sublattice consists of four *Zn* atoms and the other sublattice consists of four Oxygen *O* atoms in a unit cell; every atom of one kind is surrounded by four atoms of the other kind and forms a tetrahedron structure [1].

ZnO commonly consists of polar (0001) and non-polar (10-10), (11-20) surfaces. The surface energy of the polar surface is higher than the non-

---



---

*Figure 2.1. The schematic representation of ZnO (wurtzite) crystal structure.*

---

polar surfaces, and therefore the preferential growth direction of ZnO NR is along the  $\langle 0001 \rangle$  [2]. Figure 2.2 shows the schematic diagram of a ZnO NR growing along the  $\langle 0001 \rangle$  direction or along the c-axis.

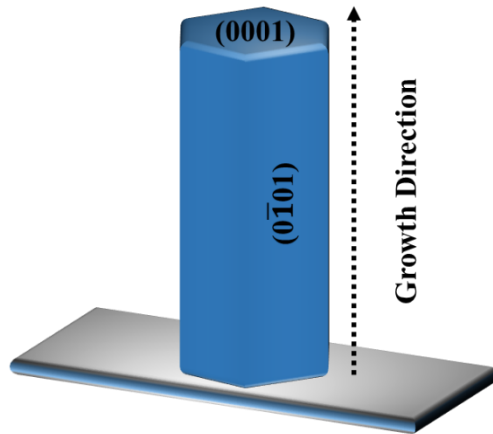


Figure 2.2. Schematic diagram of ZnO NR showing the growth direction.

ZnO-based optoelectronic and sensing devices have rapidly gained momentum due to its inimitable properties such as high exciton binding energy, high radiation resistance, chemical and thermal stability in strident ambiance, etc. Additionally, one amongst the most noteworthy properties of ZnO lies in its rich and precisely accessible nanostructures. The direct wide band gap of ZnO  $\sim 3.4$  eV is suitable for short wavelength optoelectronic applications, while the high exciton binding energy  $\sim 60$  meV allows efficient excitonic emission at room temperature [3]. Moreover, in addition to the ultraviolet (UV) emission, ZnO emission covers the whole visible region, i.e. containing green, yellow and red emission peaks [4]–[6]. The emission in the visible region is associated with deep level defects. Generally, oxygen vacancies ( $V_o$ ), zinc vacancies ( $V_{Zn}$ ), zinc interstitials ( $Zn_i$ ), and the incorporation of hydroxyl (OH) groups in the crystal lattice during the growth of ZnO are most common sources of the defects related emission [7]–[9]. ZnO naturally exhibits *n*-type semiconductor polarity due to native defects such as oxygen vacancies and zinc interstitials. *p*-type doping of ZnO is still a challenging problem that is hindering the possibility of a *p-n* homojunction ZnO devices. Furthermore, the

remarkable properties of ZnO like being bio-safe, bio-compatible, having high-electron transfer rates and enhanced growth direction (0001) analytical performances are suitable for intra/extra-cellular sensing applications [10]–[12]. Some basic physical parameters of ZnO at the room temperature are presented in *Table 2.1*.

*Table 2.1. Some basic properties of wurtzite ZnO.*

<b>Property</b>	<b>Value</b>	<b>Reference</b>
<b><i>Lattice Parameters</i></b>	a = b = 3.25 Å c = 5.21 Å	[1], [13]
<b><i>Stable crystal structure</i></b>	Wurtzite	[1]
<b><i>Density</i></b>	5.606 gm/cm <sup>3</sup>	[14]
<b><i>Melting Point</i></b>	1975 °C	
<b><i>Dielectric Constant</i></b>	8.66	[15]
<b><i>Refractive Index</i></b>	2.008	[1]
<b><i>Energy Gap</i></b>	3.4 eV, direct	[1], [16]
<b><i>Exciton Binding Energy</i></b>	60 meV	[17]
<b><i>Effective Mass (Electron/Hole)</i></b>	0.24 m <sub>o</sub> /0.59 m <sub>o</sub>	[16]
<b><i>Electron Mobility</i></b>	100-200 cm <sup>2</sup> /Vs	[14]
<b><i>Hole Mobility</i></b>	5-50 cm <sup>2</sup> /Vs	
<b><i>Bulk Young Modulus</i></b>	111.2 ± 4.7 GPa	[17]

## 2.2. Graphene Quantum Dots

Graphene quantum dots (GQDs) consisting of two-dimensional graphene sheets with dimensions less than 100 nm in single, double or few (3–10) layers. [18], [19] They are different from the spherical photoluminescent carbon nanodots within 10 nm in diameter, which is generally divided into carbon quantum dots (CQDs) with crystal lattices and carbon nanoparticles without crystalline structures.[20] Compared with the above mentioned carbon nanodots, their cousin GQDs possess excellent physical and chemical properties, such as higher surface area, larger length-to-diameter ratio, and better surface grafting via the  $\pi$ - $\pi$  conjugated network because of their structural graphene layers. GQDs

possess not only intriguing properties of the graphene,[21]–[24] but also improved solubility and extended fluorescence compared with those of larger graphene sheets.[18], [25] Interestingly, as a new family member of the fluorescent materials, GQDs display many merits, such as lower toxicity, better resistance to photo bleaching and better biocompatibility, compared with commercial organic dyes and traditional semiconductor quantum dots (for example, CdS and CdTe).[26] Therefore, fluorescent GQDs with unique structure and properties provide an unprecedented opportunity to improve the performance of organic light-emitting diodes, fuel cells, bioimaging and so on [21], [24]–[27]. Of particular interest is the recent finding that GQDs can be used as fluorescent sensing probes to detect inorganic ions, small organic molecules, and large biomaterials.[18], [28] This is because a) the high photo-stability of GQDs guarantees the stability of the fluorescence signal, which can ensure the accuracy of the detection results; b) qualitative detection of an analyte can be easily achieved by simply monitoring the variation of the fluorescence intensity of GQDs without the need for expensive instruments, time-consuming operations and complicated sample pretreatment; and c) their low toxicity and good biocompatibility make GQDs safe for humans and the environment. Therefore, GQD-based fluorescent probes are promising candidates for analyte detection, and many studies on this topic are emerging at present.

### ***2.2.1. Synthesis of GQDs***

Commercially available graphene oxide (GO, 800 mg) was heated in a furnace at 200 °C for two hours to obtain graphene sheets (GSs), and the resultant graphene sheets were mixed with 3:1 HNO<sub>3</sub>: H<sub>2</sub>SO<sub>4</sub>. This mixture was then heated at 90 °C for 3 hours and was diluted with 250 ml distilled water. Further, the mixture was filtered through 0.22 μm microporous syringe filter to remove the acids. Then the purified (300 mg) oxidized GSs were dissolved in 50 ml of Millipore water, and the pH was adjusted to 8 with NaOH. This mixture was then taken in a reaction bomb vessel, and the vessel was kept in a hot air oven for 12

hours with a constant heating at 200 °C. Finally, the solution was dialyzed for 24 hours with a dialysis tube of 3500 K Dalton.

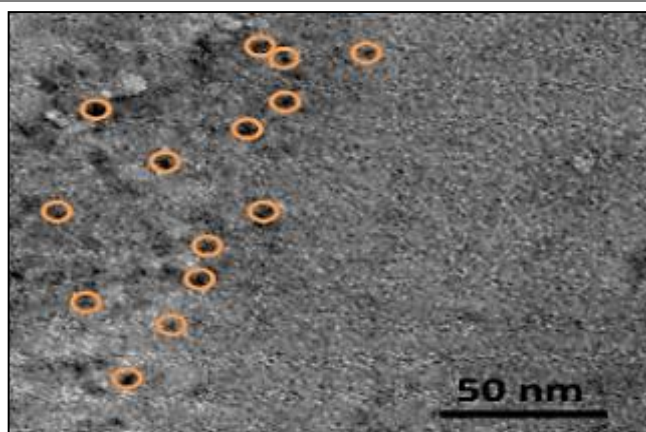


Figure 2.3. TEM image of as obtained GQDs.

### 2.2.2. Properties of Synthesized GQDs

A transmission electron microscopy (TEM) image of the GQD nanoparticles was taken and has been shown in Figure 2.3. The approximate size of the GQDs in the figure can be around 8-10 nm.

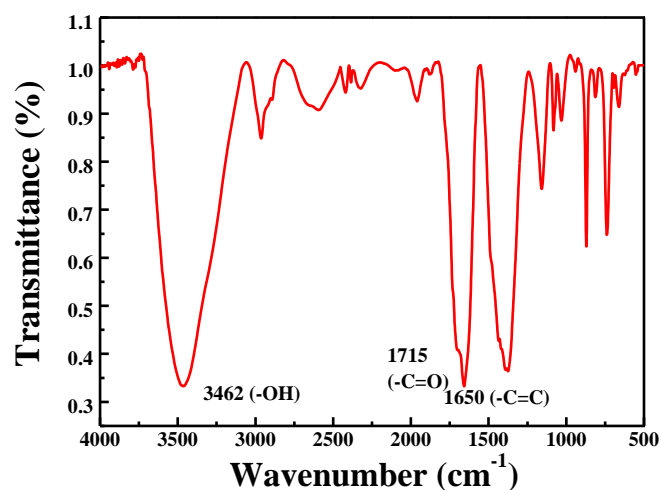


Figure 2.4. FTIR spectrum of GQDs. GQDs were in the form of KBr pellets, thoroughly dried before mixing with KBr.

For further confirmation of the formation of GQDs, the FT-IR spectroscopy of GQDs was done and the results obtained is shown in Figure 2.4. IR spectra depicted a peak at 3462  $\text{cm}^{-1}$  due to the presence of -OH group and a peak at 1715  $\text{cm}^{-1}$  for carbonyl group. These two peaks suggest the presence of the carboxyl group in GQDs.[29] And also

the presence of a peak at 1650 due to carbon-carbon double bond tells us that these GQDs are completely reduced, and functional groups are present only at the edge of GQDs.

### **2.3. Oligo-(*p*-phenylenevinylene)**

Oligo(phenylenevinylene)s (OPVs) are extensively investigated *p*-conjugated molecules that exhibit absorption and fluorescence in the UV-Vis spectral region, which can be widely tuned by chemical functionalization and external control (e.g., solvent, temperature, pH). Further modulation of the optoelectronic properties of OPVs is possible by supramolecular aggregation, primarily driven by hydrogen bonding or *p*-stacking interactions. In recent years, extensive research work has been accomplished in exploiting the unique combination of the structural and electronic properties of OPVs, most of which have been targeted at the preparation of molecules and materials featuring photoinduced energy transfer.

Due to intrinsic absorption and fluorescence behaviors,  $\pi$ -conjugated OPVs are widely used in the development of optoelectronics and photonics applications. The optoelectronic behavior of OPVs can be tuned by chemical functionalization and external stimuli, *e.g.* pH, solvent and temperature[30], [31]. Moreover, supramolecular architectures of functionalized OPVs, which are driven by hydrogen bonding as well as  $\pi$ - $\pi$  stacking interactions, are highly conceived.[32] Well-defined supramolecular architectures are of growing attraction for applications in optoelectronics and photonics.

#### **2.3.1. Synthesis of OPV**

##### **2.3.1.1. Materials:**

All starting materials including L-tyrosine, 4-iodobenzoic acid, 1,4-divinylbenzene, tetrakis(triphenylphosphine)palladium(0) (Pd(PPh<sub>3</sub>)<sub>4</sub>), 1-ethyl-3-(3-dimethylaminopropyl)carbodiimide (EDC), 4-(*N,N*-dimethylamino) pyridine, 1-hydroxybenzotriazole (HOBt) were purchased from commercial sources (Sigma-Aldrich, Alfa Aesar and Merck).

2.3.1.2. *Synthesis of Oligo(p-phenylenevinylene)(OPV) Conjugated Oligopeptide:*

Y-4-iodobenzoate (3):

A solution of 4-iodobenzoic acid (4.96 g, 20 mmol) and HOBt (3.51 g, 26 mmol) was stirred in DMF (30 mL). After that, methyl ester of L-tyrosine (4.29 g, 22 mmol), EDC (4.03 g, 26 mmol) and DMAP (3.17 g, 26 mmol) were added at 0 °C to the stirred solution. The mixture was allowed to stir at room temperature for 12 h. The reaction mixture was diluted with ethyl acetate, and the organic layer was washed with 1M HCl (2 × 60 mL), brine, 1M Na<sub>2</sub>CO<sub>3</sub> (3 × 60 mL), and again with brine. The organic layer was dried over Na<sub>2</sub>SO<sub>4</sub> and evaporated under vacuum to yield compound 3 as a white solid. Yield = 5.200 g (12.23 mmol, 61%). <sup>1</sup>H NMR (400 MHz, DMSO-*d*<sub>6</sub>): δ = 9.22 (s, 1H), 8.87 (d, 1H), 7.85 (d, 2H), 7.58 (d, 2H), 7.05 (d, 2H), 6.63 (d, 2H), 4.53 (q, 1H), 3.62(s, 3H), 3.04-2.91 (m, 2H) ppm. ESI-MS *m/z* calculated for C<sub>17</sub>H<sub>16</sub>NO<sub>4</sub>INa: 448.0023 (M+Na)<sup>+</sup>; found: 448.0025 (M+Na)<sup>+</sup>.

MeO-Y-OPV-Y-OMe (4):

A mixture of 1,4-divinylbenzene (0.39 g, 3 mmol), compound 3 (2.81 g, 6.6 mmol), and K<sub>2</sub>CO<sub>3</sub> (2.86 g, 21.21 mmol) in 50 mL of DMF was degassed under vacuum by using an oil pump and purged with nitrogen three times. After nitrogen purging, Pd(PPh<sub>3</sub>)<sub>4</sub> (138 mg, 0.12 mmol) was added to the reaction mixture. The resulting mixture was again degassed and purged with nitrogen three times. Then the reaction mixture was stirred at 120 °C for 72 h. The mixture was cooled to room temperature and poured into water and washed with ethyl acetate (3 x 50 mL). The organic layer was dried over Na<sub>2</sub>SO<sub>4</sub> and evaporated under vacuum. Desire compound was purified by column chromatography on silica gel (100–200 mesh) with ethyl acetate/toluene (1:1) as the eluent to get compound 4 as a white solid. Yield = 1.2015 g (1.66 mmol, 55 %). <sup>1</sup>H NMR (400 MHz, CDCl<sub>3</sub>, δ<sub>ppm</sub>): δ = 7.73 (d, 4H), 7.56 (d, 4H), 7.45-7.32 (m, 4H), 7.21-7.08 (m, 4H), 6.99 (d, 4H), 6.74 (d, 4H), 6.63 (d, 2H), 5.59 (s, 2H), 5.08 (q, 2H), 3.78 (s, 6H), 3.19 (m, 4H) ppm. ESI-MS *m/z*

calculated for  $C_{44}H_{40}N_2O_8Na$ : 747.2682 ( $M+Na$ )<sup>+</sup>; found: 747.2677( $M+Na$ )<sup>+</sup>.

#### HO-Y-OPV-Y-OH (5):

A solution of 4 (0.72 g, 1 mmol) in dry methanol (10 mL) was allowed to react with 2M NaOH. The progress of the reaction was monitored by TLC. The reaction mixture was kept under stirring up for 6 h. Then, methanol was removed under vacuum. The residue was dissolved in water (100 mL) and washed with diethyl ether ( $2 \times 20$  mL). Then, the pH of the aqueous layer was adjusted to 2 by using 2M HCl and extracted with ethyl acetate ( $3 \times 30$  mL). The ethyl acetate layer was dried over anhydrous sodium sulphate and evaporated under vacuum to yield 5 as white solid. Yield = 0.66 g (0.94 mmol, 94%). <sup>1</sup>H NMR (400 MHz, DMSO-*d*<sub>6</sub>):  $\delta$  = 12.66 (s, 2H), 9.17 (s, 2H), 7.92-7.22 (m, 16H), 7.10 (d, 4H), 6.64 (d, 4H), 4.43 (m, 2H), 3.08-2.92 (m, 4H) ppm. ESI-MS *m/z* calculated for  $C_{42}H_{35}N_2O_8$ : 695.2394 ( $M-H$ )<sup>-</sup>; found: 695.2472 ( $M-H$ )<sup>-</sup>.

#### MeO-YY-OPV-YY-OMe (6):

A solution of compound 5 (0.5574 g, 0.8 mmol) and HOBt (0.248 g, 1.84 mmol) was stirred in DMF (20 mL). To the stirred solution, H<sub>2</sub>N-Tyr-OMe (0.171 g, 0.88 mmol), EDC (0.2856 g, 1.84 mmol) and DMAP (0.224 g, 1.84 mmol) were added at 0 °C. The resulting mixture was allowed to stir at room temperature for 12 h. The reaction mixture was diluted with ethyl acetate, and the organic layer was washed with 1M HCl ( $2 \times 30$  mL), brine, 1M Na<sub>2</sub>CO<sub>3</sub> ( $3 \times 30$  mL) and again with brine. The organic layer was dried over Na<sub>2</sub>SO<sub>4</sub> and evaporated under vacuum to get compound 6. Yield = 0.46 mg (0.44 mmol, 55.23%) as white solid. Purification of the product was performed by column chromatography on silica gel (100–200 mesh) with ethyl acetate/toluene (1:1) as the eluent. ESI-MS *m/z* calculated for  $C_{42}H_{36}N_2O_8Na$ : 1073.3949 ( $M+Na$ )<sup>+</sup>; found: 1073.3933 ( $M+Na$ )<sup>+</sup>.

### HO-YY-OPV-YY-OH (1):

A solution of 6 (0.42 g, 0.4 mmol) in dry MeOH (10 mL) was allowed to react with a 2M solution of NaOH. TLC monitored the progress of the reaction. The reaction mixture was stirred up for 6 h. Then, methanol was removed under vacuum. The residue was dissolved in water (100 mL) and washed with diethyl ether ( $2 \times 20$  mL). The pH of the aqueous layer was adjusted to 2 by using 2M HCl and extracted with ethyl acetate ( $3 \times 30$  mL). The ethyl acetate layer was dried over anhydrous sodium sulphate and evaporated under vacuum to get compound 1 as yellow

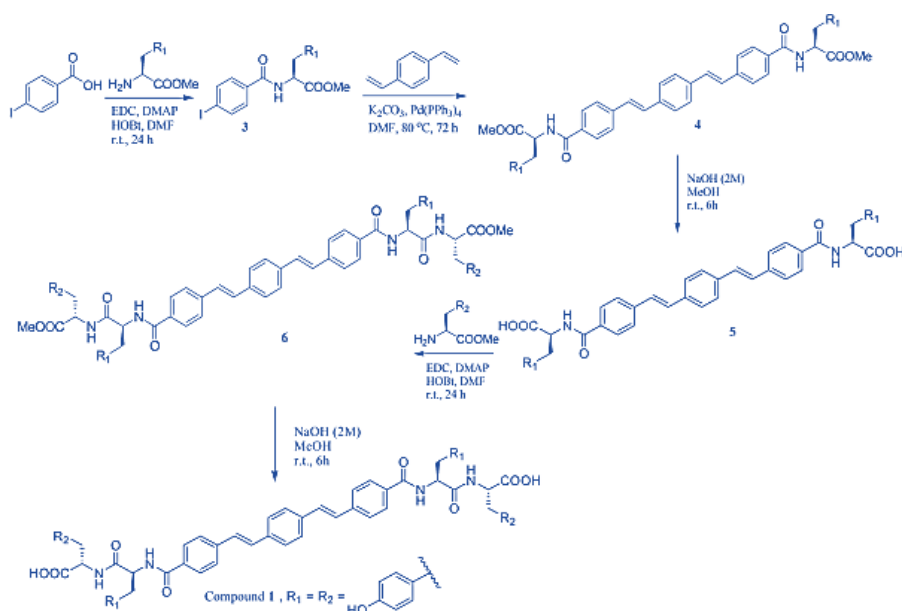


*Figure 2.5. Synthetic scheme of compound 1 (HO-YY-OPV-YY-OH).*

solid. Yield = 0.34 g (0.33 mmol, 83%).  $^1\text{H NMR}$  (400 MHz,  $\text{DMSO-}d_6$ ):  $\delta$  = 12.73 (s, 2H), 9.17 (d, 2H), 9.11 (s, 2H), 8.45 (d, 1H), 8.37 (d, 1H), 8.32 (d, 1H), 8.17 (d, 1H), 7.92-6.71 (m, 28H), 6.60 (m, 8H), 4.64 (m, 2H), 4.40 (m, 2H), 2.92-2.60 (m, 8H) ppm. ESI-MS  $m/z$  calculated for  $\text{C}_{60}\text{H}_{53}\text{N}_4\text{O}_{12}$ : 1021.3660 (M-H) $^-$ ; found: 1021.3622 (M-H) $^-$ .

### MeO-OPV-OMe (7):

4-Iodo-benzoic acid methyl ester (0.724 g, 2.53 mmol), triphenylphosphine (25 mg, 9.21 mmol), triethylamine (2 mL) and 20 mL DMF were placed in a 100 mL two neck round bottle flask. The solvent was purged for 30 minutes under nitrogen gas. After that

divinylbenzene (0.15 gm, 1.15 mmol) and Pd(OAc)<sub>2</sub> (12 mg, 5.75 mmol) were added to the reaction mixture. The reaction mixture was stirred at 110 °C for 72 hours. The mixture was cooled to room temperature and poured into water, extracted with dichloromethane. Organic part was washed with 1M HCl (3 x 100 mL) and brine (3 x 100 mL) solution. Obtained organic part was dried over anhydrous NaSO<sub>4</sub>. Finally, after concentrated in a vacuum, the resulting mixture was purified by silica gel column chromatography (hexane/ethyl acetate = 20:1) to afford the desired product. Yield = 0.25 g (0.63 mmol, 54%). <sup>1</sup>H-NMR (400 MHz, CDCl<sub>3</sub>) : δ = 8.02 (d, 4H), 7.82 (d, 4H), 7.45 (d, 4H), 7.59 (d, 4H), 3.93 (s, 6H) ppm. HRMS-MS *m/z* calculated for C<sub>26</sub>H<sub>22</sub>O<sub>4</sub>Na: 421.1416 (M+Na)<sup>+</sup>; found 421.1430 (M+Na)<sup>+</sup>.

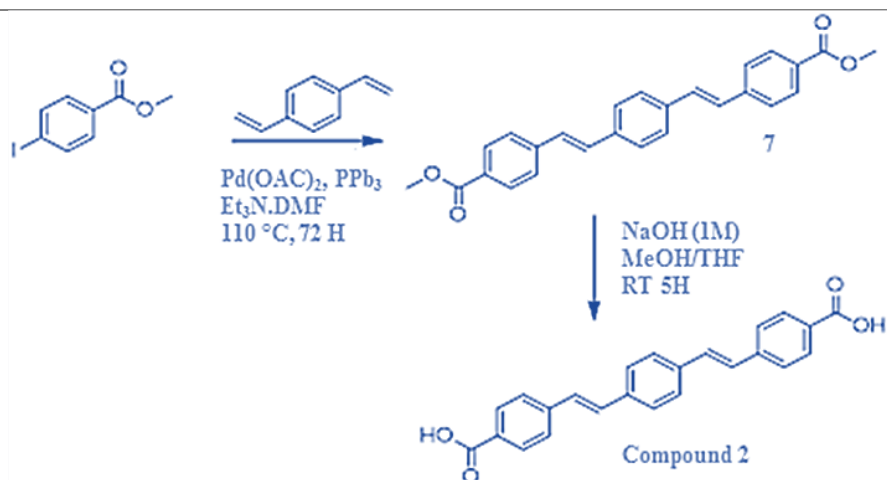


Figure 2.6. Synthesis scheme of compound 2 (HO-OPV-OH).

#### HO-OPV-OH (2):

A solution of 7 (0.25 g, 0.62 mmol) in 1M NaOH and 15 mL MeOH/THF (1:1) was stirred at room temperature, and the reaction was monitored by TLC. The reaction mixture was stirred up to 5h for complete conversion. The reaction mixture was concentrated under vacuum, and the residue was suspended in water. The aqueous layer was extracted with diethyl ether. The aqueous layer was acidified to pH = 2 with 1M HCl, then extracted with ethyl acetate. The organic layer was dried over Na<sub>2</sub>SO<sub>4</sub> and concentrated on getting compound 2. Yield = 0.20 g (0.54 mmol, 87% yield). <sup>1</sup>H-NMR (400MHz, DMSO-d<sub>6</sub>): δ =

12.87 (s, 2H), 8.03 (d, 4H), 7.88 (d, 4H), 7.73 (d, 4H), 7.46 (d, 4H) ppm. HRMS-MS  $m/z$  calculated for  $C_{24}H_{18}O_4Na$ : 393.1097 ( $M+Na$ )<sup>+</sup>; found 393.1087 ( $M+Na$ )<sup>+</sup>.

### 2.3.2. Properties of Synthesized OPVs

The detailed properties of the synthesized OPVs as per the application is discussed in Chapter 5. The density functional theory was employed to calculate the theoretical HOMO and LUMO levels of OPV, as shown in Figure 2.7, and the calculated values of HOMO and LUMO were -5.4 eV and -2.2 eV respectively. Thus, the calculated bandgap of OPV was 3.2 eV.

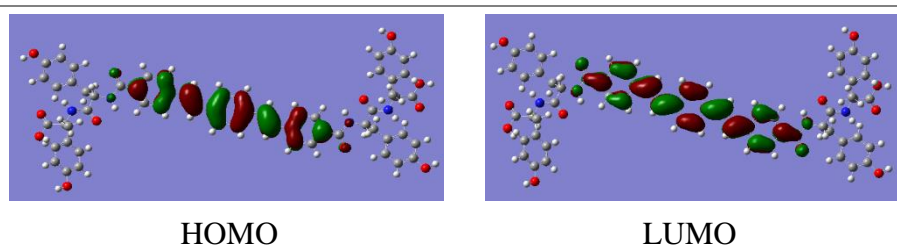


Figure 2.7. Calculated molecular orbitals for compound **1** at the B3LYP/6-31G\*\* level for C, N, O, and H.

---

## 2.4. References

- [1] C. Jagadish and S. J. Pearton, Zinc Oxide Bulk, Thin Films, and Nanostructures: Processing, Properties, and Applications. Elsevier, 2006.
- [2] S. Xu and Z. L. Wang, “One-dimensional ZnO nanostructures: Solution growth and functional properties,” *Nano Res.*, vol. 4, no. 11, pp. 1013–1098, Nov. 2011.
- [3] A. B. Djurišić, A. M. C. Ng, and X. Y. Chen, “ZnO nanostructures for optoelectronics: Material properties and device applications,” *Prog. Quantum Electron.*, vol. 34, no. 4, pp. 191–259, Jul. 2010.
- [4] M. Willander et al., “Zinc oxide nanorod based photonic devices: Recent progress in growth, lightemitting diodes and lasers,”

Nanotechnology, vol. 20, no. 33, p. 332001, Aug. 2009.

- [5] A. B. Djurišić, Y. H. Leung, K. H. Tam, L. Ding, W. K. Ge, H. Y. Chen, and S. Gwo, “Green, yellow, and orange defect emission from ZnO nanostructures: Influence of excitation wavelength,” *Appl. Phys. Lett.*, vol. 88, no. 10, p. 103107, Mar. 2006.
- [6] N. H. Alvi, K. ul Hasan, O. Nur, and M. Willander, “The origin of the red emission in *n*-ZnO nanotubes/p-GaN white light emitting diodes,” *Nanoscale Res. Lett.*, vol. 6, no. 1, p. 130, 2011.
- [7] C. V. Manzano, D. Alegre, O. Caballero-Calero, B. Alén, and M. S. Martín-González, “Synthesis and luminescence properties of electrodeposited ZnO films,” *J. Appl. Phys.*, vol. 110, no. 4, p. 043538, Aug. 2011.
- [8] A. Janotti and C. G. Van de Walle, “Fundamentals of zinc oxide as a semiconductor,” *Reports Prog. Phys.*, vol. 72, no. 12, p. 126501, 2009.
- [9] C. H. Park, S. B. Zhang, and S.-H. Wei, “Origin of *p*-type doping difficulty in ZnO: The impurity perspective,” *Phys. Rev. B*, vol. 66, no. 7, p. 073202, Aug. 2002.
- [10] M. H. Asif, S. M. U. Ali, O. Nur, M. Willander, U. H. Englund, and F. Elinder, “Functionalized ZnO nanorod-based selective magnesium ion sensor for intracellular measurements,” *Biosens. Bioelectron.*, vol. 26, no. 3, pp. 1118–1123, Nov. 2010.
- [11] S. M. Usman Ali, N. H. Alvi, Z. Ibupoto, O. Nur, M. Willander, and B. Danielsson, “Selective potentiometric determination of uric acid with uricase immobilized on ZnO nanowires,” *Sensors Actuators, B Chem.*, vol. 152, no. 2, pp. 241–247, Mar. 2011.
- [12] J. Zhou, N. S. Xu, and Z. L. Wang, “Dissolving Behavior and Stability of ZnO Wires in Biofluids: A Study on Biodegradability and Biocompatibility of ZnO Nanostructures,” *Adv. Mater.*, vol. 18, no. 18, pp. 2432–2435, Sep. 2006.

- [13] H. Morkoç and U. Özgür, *Zinc oxide : fundamentals, materials and device technology*. Wiley-VCH, 2009.
- [14] K. Ellmer, A. Klein, and B. Rech, *Transparent conductive zinc oxide : basics and applications in thin film solar cells*. Springer, 2008.
- [15] S. J. Pearton, D. P. Norton, K. Ip, Y. W. Heo, and T. Steiner, "Recent progress in processing and properties of ZnO," *Prog. Mater. Sci.*, vol. 50, no. 3, pp. 293–340, Mar. 2005.
- [16] B. G. Yacobi, *Semiconductor Materials : an Introduction to Basic Principles*. Kluwer Academic/Plenum Publishers, 2003, 2003.
- [17] A. B. Djurišić, X. Chen, Y. H. Leung, and A. Man Ching Ng, "ZnO nanostructures: growth, properties, and applications," *J. Mater. Chem.*, vol. 22, no. 14, p. 6526, 2012.
- [18] S. Benítez-Martínez and M. Valcárcel, "Graphene quantum dots in analytical science," *TrAC Trends Anal. Chem.*, vol. 72, pp. 93–113, Oct. 2015.
- [19] L. Li, G. Wu, G. Yang, J. Peng, J. Zhao, and J. J. Zhu, "Focusing on luminescent graphene quantum dots: Current status and future perspectives," *Nanoscale*, vol. 5, no. 10, pp. 4015–4039, May 2013.
- [20] S. Zhu, Y. Song, X. Zhao, J. Shao, J. Zhang, and B. Yang, "The photoluminescence mechanism in carbon dots (graphene quantum dots, carbon nanodots, and polymer dots): current state and future perspective," *Nano Res.*, vol. 8, no. 2, pp. 355–381, Feb. 2015.
- [21] Q. Li, B. Guo, J. Yu, J. Ran, B. Zhang, H. Yan, and J. R. Gong, "Highly efficient visible-light-driven photocatalytic hydrogen production of CdS-cluster-decorated graphene nanosheets," *J. Am. Chem. Soc.*, vol. 133, no. 28, pp. 10878–10884, Jul. 2011.
- [22] P. Guo, F. Xiao, Q. Liu, H. Liu, Y. Guo, J. Ru Gong, S. Wang, and Y. Liu, "One-pot microbial method to synthesize dual-doped

- graphene and its use as high-performance electrocatalyst,” *Sci. Rep.*, vol. 3, no. 1, p. 3499, Dec. 2013.
- [23] G. Xie, K. Zhang, H. Fang, B. Guo, R. Wang, H. Yan, L. Fang, and J. R. Gong, “A photoelectrochemical investigation on the synergetic effect between CdS and reduced graphene oxide for solar-energy conversion,” *Chem. - An Asian J.*, vol. 8, no. 10, pp. 2395–2400, Oct. 2013.
- [24] J. Zhang, J. Yu, M. Jaroniec, and J. R. Gong, “Noble Metal-Free Reduced Graphene Oxide-Zn<sub>x</sub>Cd<sub>1-x</sub>S Nanocomposite with Enhanced Solar Photocatalytic H<sub>2</sub>-Production Performance,” *Nano Lett.*, vol. 12, no. 9, pp. 4584–4589, Sep. 2012.
- [25] Z. Zhang, J. Zhang, N. Chen, and L. Qu, “Graphene quantum dots: An emerging material for energy-related applications and beyond,” *Energy Environ. Sci.*, vol. 5, no. 10, pp. 8869–8890, Sep. 2012.
- [26] Z. Wang, H. Zeng, and L. Sun, “Graphene quantum dots: Versatile photoluminescence for energy, biomedical, and environmental applications,” *J. Mater. Chem. C*, vol. 3, no. 6, pp. 1157–1165, Jan. 2015.
- [27] Q. Liu, B. Guo, Z. Rao, B. Zhang, and J. R. Gong, “Strong two-photon-induced fluorescence from photostable, biocompatible nitrogen-doped graphene quantum dots for cellular and deep-tissue imaging,” *Nano Lett.*, vol. 13, no. 6, pp. 2436–2441, Jun. 2013.
- [28] J. Ju and W. Chen, “Graphene Quantum Dots as Fluorescence Probes for Sensing Metal Ions : Synthesis and Applications,” *Curr. Org. Chem.*, vol. 19, no. 12, pp. 1150–1162, Jun. 2015.
- [29] S. Some, A. R. Gwon, E. Hwang, G. H. Bahn, Y. Yoon, Y. Kim, S. H. Kim, S. Bak, J. Yang, D. G. Jo, and H. Lee, “Cancer therapy using ultrahigh hydrophobic drug-loaded graphene derivatives,” *Sci. Rep.*, vol. 4, no. 1, p. 6314, May 2014.

- [30] A. Chaieb, L. Vignau, R. Brown, G. Wantz, N. Huby, J. François, and C. Dagron-Lartigau, "PL and EL properties of oligo(p-phenylene vinylene) (OPPV) derivatives and their applications in organic light-emitting diodes (OLED)," *Opt. Mater. (Amst)*., vol. 31, no. 1, pp. 68–74, Sep. 2008.
- [31] H. Li, L. Wang, B. Zhao, P. Shen, and S. Tan, "Synthesis and optoelectronic properties of liquid-crystalline copolymers based on fluorene and triphenylamine-containing oligo(p-phenylenevinylene) derivatives for white light emission," *J. Polym. Sci. Part A Polym. Chem.*, vol. 47, no. 13, pp. 3296–3308, Jul. 2009.
- [32] V. K. Praveen, C. Ranjith, E. Bandini, A. Ajayaghosh, and N. Armaroli, "Oligo(phenylenevinylene) hybrids and self-assemblies: versatile materials for excitation energy transfer," *Chem. Soc. Rev.*, vol. 43, no. 12, pp. 4222–4242, 2014.



# Chapter 3

## Fabrication and Characterization Techniques

The literature has various reports on the diverse techniques that have been adopted for the preparation of hybrid nanostructures and their thin films. In the present thesis work, the nanocomposites of ZnO were grown by using electrodeposition technique on coated substrates. These substrates (generally glass or silicon) were coated with Ga doped ZnO or ITO using the ion sputtering process. However, the Pt electrode pattern has been deposited using RF magnetron sputtering facility at CEERI-Pilani. The detailed description regarding the selection of substrate and its cleaning, the deposition system used, the characterization techniques employed, and the sensor testings are discussed in detail in the following sections.

### 3.1. Substrate Selection and Its Cleaning

The quality of the deposited film depends on the nature and surface condition of the substrate on which the films are grown. The selection of the substrate generally depends on the type of application, the process, the cost, the availability and the packaging of the device. Some of the desired properties in a substrate are – a) good mechanical strength, b) chemical inertness, c) low porosity, etc. In the present work, different substrates used for the deposition of sensing film are mainly, silicon (100 and 111) and borosilicate glass. The selection of Silicon as the substrate is due to its excellent thermal and mechanical properties, its wide use in various applications and established fabrication process. The glass substrates have been used because of their excellent transparency which is useful for the optical characterizations.

It is a well-known fact that the substrate contamination may affect the film purity and their adhesion to the substrates. Hence, it is essential to

clean the substrates thoroughly before the start of the deposition process to get films with reproducible properties. The cleaning process involves the breaking of bonds between contaminants and the substrate. The choice of cleaning process depends on

- Nature of substrate
- Type of contaminants
- Degree of cleanliness required

The common cleaning procedure includes solvent cleaning, thermal cleaning by heating the substrate or glow discharge cleaning. The most commonly used procedure is solvent cleaning. Any dust, fingerprints, grease or oil on the substrate results in poor adhesion of the deposited film with the substrate, as a result, the film peels off. Therefore, substrates were cleaned thoroughly before loading into the deposition chamber.

### ***3.1.1. Procedures Employed for Si Substrate Cleaning***

In the present work, the following procedures were employed for the Si-substrate cleaning.

- Remove dust using pipette like blower before cleaning the substrates.
- Ultrasonic cleaning in diluted HF solution to remove native silicon dioxide from wafers.
- Rinse with de-ionized water to remove any HF remaining.
- Ultrasonic cleaning in diluted TCE solution to remove any fingerprints on the wafer or any other heavy residue on the wafer.
- Rinse with de-ionized water to remove any TCE remaining.
- Ultrasonic cleaning in acetone to remove the organic remnants/contaminants from the wafers.
- Rinse with de-ionized water to remove any acetone remaining.
- Ultrasonic cleaning in diluted isopropanol solution for dissolving non-polar contaminants which are left on the wafers.

- Rinse with de-ionized water to remove any isopropanol remaining.
- Purge with Nitrogen to remove any water remaining.

### ***3.1.2. Procedure Employed for Glass Substrate Cleaning***

Glass substrates have been used because of their excellent transparency facilitating optical characterizations. In addition to that, the glass substrates are cost-effective and readily available commercially. Although there is no definite procedure for cleaning the glass substrate, the procedure employed in the present work is as described below:

- Ultrasonic cleaning with soap water to remove any fingerprints, or oil contamination.
- Rinse with de-ionized water to remove any soap remaining.
- Ultrasonic cleaning in acetone to remove tiny dust particles on the surface through agitation.
- Isopropanol to remove further contaminants.
- Rinse with de-ionized water and blow off the water-droplets.
- Remove any other dust using Nitrogen purging.

## **3.2. Fabrication Techniques**

For the growth of thin films and nanostructures, different fabrication techniques have been employed. The DIBS system is used for coating the substrate, and electrodeposition is used for thin film growth in this research work. The two systems mentioned above is explained concisely in the following section.

### ***3.2.1. Dual Ion Beam Sputtering System***

Electrorava make DIBS system, is a specifically designed, compact, clean room compatible, and versatile state-of-the-art system. DIBS is a very effective physical vapor deposition technique for the preparation of epitaxial films under moderate vacuum, or ultrahigh vacuum conditions [1-3]. This is a relatively simple and versatile technique commonly used

for thin-film deposition of high crystalline quality. The main components of this system are

- (i) Deposition chamber,
- (ii) Load lock chamber,
- (iii) Ion sources,
- (iv) Robotic arm,
- (v) Vacuum pumps and vacuum gauges,
- (vi) Heater assembly, water chiller, and parameter controlling unit

Figure 3.1 shows an actual image of the DIBS system. The system consists of two chambers. First is the main deposition chamber (DPC), and the other one is a load lock chamber (LLC).



---

*Figure 3.1. Actual image of dual ion beam sputtering system.*

---

The actual growth is executed in DPC while the LLC is used for loading the sample. Both the chambers are separated by a gate valve. The vacuum is maintained in both DPC and LLC by two separate turbo molecular pumps. Vacuum gauges are employed to measure the vacuum

level in the deposition and load lock chamber. The background pressure inside the DPC and LLC are maintained at  $10^{-8}$  mbar and  $10^{-9}$  mbar respectively. The chambers are made up of stainless steel as it is non-corrodible, non-magnetic, easy to weld and clean, highly malleable and have good out gassing characteristics [4]. The substrate holder is attached to the heater assembly for maintaining the desired temperature ranging from room temperature to 1000 °C during the growth as well as annealing processes. The water chiller is employed to remove heat from the deposition chamber, target assembly, and vacuum pumps. DIBS system growth parameters, i.e. growth temperature, gas pressure, gas composition, and RF power are controlled by parameter controlling unit of the DIBS system [3-5]. In order to load the sample: first, the pressure of LLC is released, and then the sample is kept in LLC, which is finally loaded in the main deposition chamber by an automatic computer-controlled robotic arm. The DIBS system's schematic diagram is shown in Figure 3.2 This DPC chamber consists of two separate ion sources.

- (i) Primary ion source or main deposition source
- (ii) Secondary ion source or assist source

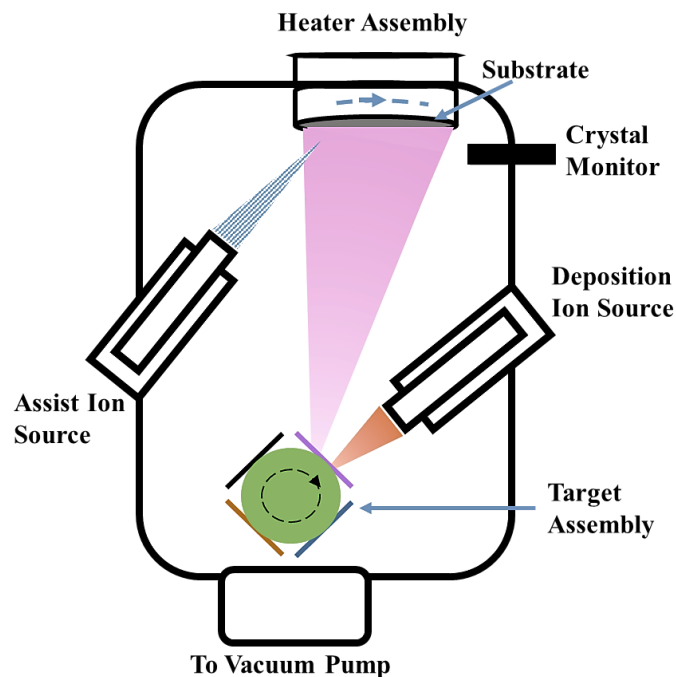


*Figure 3.2. Schematic diagram of dual ion beam sputtering system.*

---

The function of the main ion source is to sputter materials from a target. Four targets can be mounted in a rotating target assembly inside the chamber, and the desired target can be chosen at the time of deposition. The secondary ion source, i.e. the assist ion source which is exposed to the substrate, is employed to pre-clean the substrate surface before film deposition and to hinder island formation and remove weak dangling bonds during the actual sputtering process [1,2]. The angle between the primary ion source and the sputtering target is fixed at 45° off normal while the angle between the assist ion source and the substrate is maintained at 60°. Another important unique features of the DIBS system are high-quality growth with reduced surface roughness, increased growth uniformity on a larger substrate area and in-situ substrate pre-cleaning before growth.

In DIBS system, Kauffman Robinson ion sources are employed to generate Ar<sup>+</sup> ion beam. Ar<sup>+</sup> ion beam is spatially mono-energetic and well confined [1-3]. Essentially, an ion beam source is a plasma source fitted with a set of grids enabling a stream of ions to be extracted. The primary ion source has three main parts: the discharge chamber, grids, and neutralizer. When the Ar gas is exposed to an RF field, it results in the production of Ar<sup>+</sup> gas in the discharge chamber. The gas is fed into

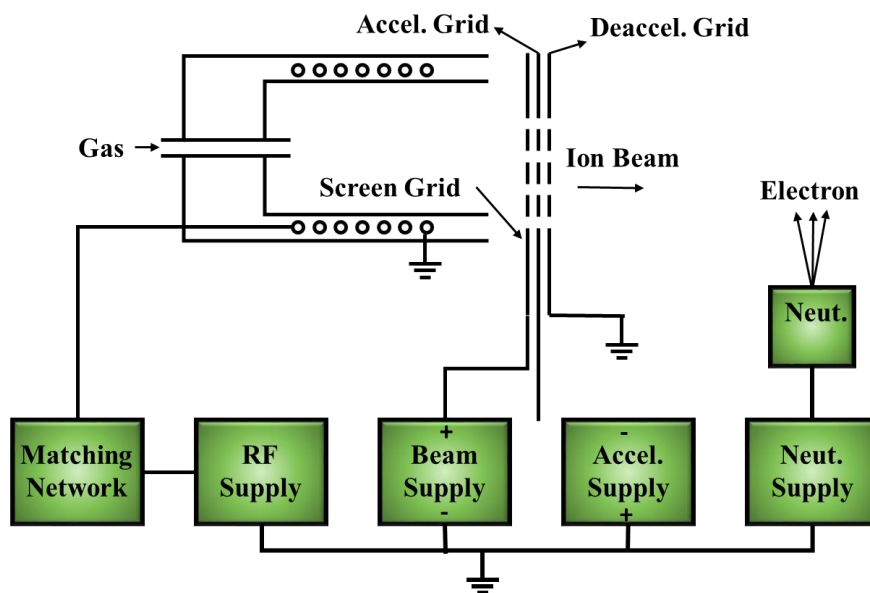


Figure 3.3. Schematic diagram of primary ion beam source.

a quartz or alumina chamber with an RF powered coil around it. The RF field excites free electrons until they have enough energy to break gas atoms into ions and electrons. The gas is thus ionized, and plasma is established. The various voltages applied on grids pull out the  $\text{Ar}^+$  ions in the form of a beam from the discharge chamber. Primary source contains three-grids to eject the ions and to reduce the beam spreading. The neutralizer (hollow cathode electron source) is used in primary source assembly to neutralize the positive ion beam [2]. The schematic diagram of the primary ion source is shown in Figure 3.3

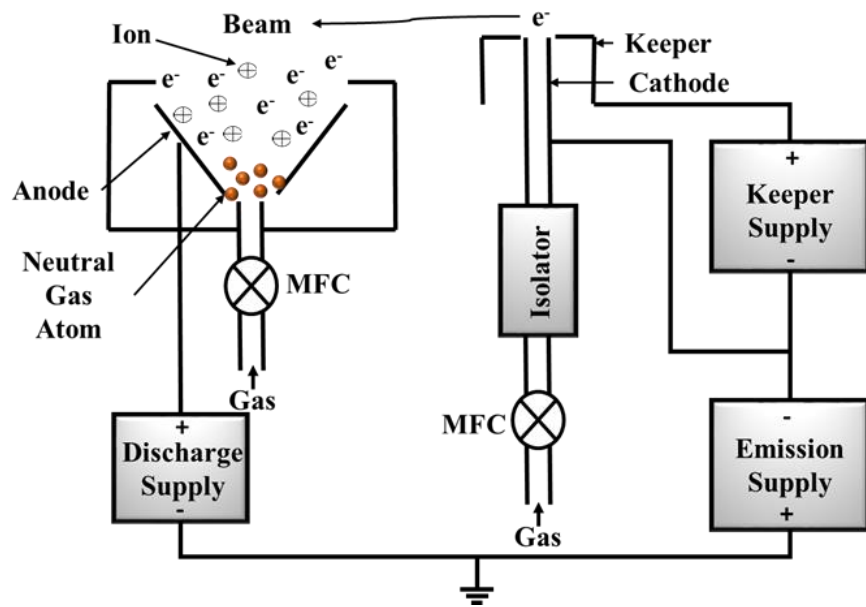


Figure 3.4. Schematic diagram of assist ion source.

The assist ion source mainly contains end-Hall 400 ion source module and hollow-cathode neutralizer assembly. This source has three varieties of power supplies (1) Keeper power supply (2) Emission power supply (3) Discharge power supply. The keeper and emission power supplies are employed for hollow cathode neutralizer. Discharge power supply offers voltage and current to end-Hall 400 ion source module. The assist ion source possesses much higher ion-current capabilities at even low ion energies (e.g., 200 eV and less) enabling suitable etching rates [4].

Moreover, cost-effectiveness, broad ion-beam coverage, and greater reliability are the expected rewards of the assist ion source. Figure 3.4 shows the schematic diagram of Assist ion source. The Discharge Power

Supply offers voltage and current to the anode of the end-Hall 400 ion source module and generates the positive  $\text{Ar}^+$  ion beam. In order to ignite the hollow cathode and keeping the cathode hot enough for thermionic emission of electrons, the Keeper Power Supply delivers voltage and current to the hollow cathode neutralizer [3,4]. The Emission Power Supply provides a negative voltage to the hollow cathode after it is ignited by the Keeper Power Supply and controls the electron beam emitted from the hollow cathode neutralizer to neutralize the positive ion beam of end-Hall 400 ion source.

### ***3.2.2. Electrodeposition System***

Electrodeposition is an electrochemical process that allows the preparation of solid deposits on the surface of conductive materials. It is a commercially highly relevant process, providing the basis for many industrial applications, such as electro-winning, refining, and metal plating. Electrodeposits are formed by the action of an electric current passing in an electrochemical cell, a device that consists of two conductive or semi-conducting electrodes immersed in an electrolyte. The electrodes are called the working electrode (cathode), consisting of the object where electrodeposition is planned, and the counter-electrode (anode), necessary to complete the electrical circuit. Electrolytes for electrodeposition are usually aqueous solutions containing positive and negative ions, prepared by dissolving metal salts. The electric current that flows between the two conductive electrodes in the presence of an external voltage is because of the motion of charged species, via migration and diffusion, towards the surfaces of the polarized electrodes. At the surface of the electrodes, the conduction mechanism must change from ionic to electronic, an interface process mediated by the occurrence of electrochemical reactions that promote the reduction or the oxidation (redox reactions) of the ionic species. An essential characteristic of electrochemical reactions is that the exchange of charge does not occur between chemical species, as it does in a typical chemical reaction, but between chemical species and the electrode. The

electrochemical reaction that is most important for the electrodeposition process is the one that occurs at the working electrode.

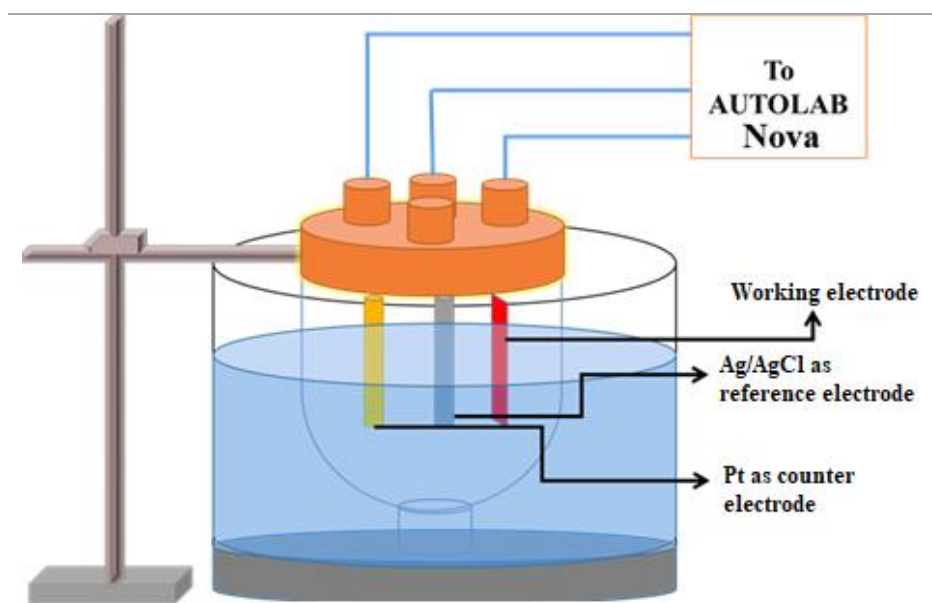


*Figure 3.5. The electrochemical cell.*

This approach is relatively simple and inexpensive, and is known as galvanostatic system because the current between the electrodes is controlled (maintained constant). Another important deposition mode is the potentiostatic one. This mode is a consequence of the development of electrochemical science, where electrochemical reactions at the surfaces of electrodes are carefully investigated. For this, reference electrodes are developed in order to measure the potential drop near the surface of the electrodes. Assuming that the electrolyte has sufficiently high conductivity to avoid any ohmic voltage drop, because of the resistance of the electrolyte between the electrodes, all the voltage applied will appear near the surface of the electrodes, where a charged region is formed. Interestingly, a simple metal foil could be used as a reference electrode; however, because of the need to have a standard electrode to measure potential drops at the surface of different types of working electrode in contact with different electrolytes, a silver/silver chloride (Ag/AgCl) was elected, and hence all electrode potentials are quoted relative to this arbitrarily chosen reference electrode. By defining the potential of the Ag/AgCl as zero, it is possible to generate a table of

all the possible redox reaction potentials relative to this electrode, and these potentials are called standard potentials. The potential of an electrochemical cell, also known as the cell potential or electromotive force (emf) is the sum of the potential drops at the cathode and anode, where the reduction and oxidation reactions occur. With the introduction of a reference electrode, the potentials of these two electrodes can be measured independently, allowing the independent investigation of the reactions that are taking place at each electrode (working or counter). A simple representation of the electrochemical cell is shown in Figure 3.5

---



*Figure 3.6. The electrodeposition setup by Metrohm (AutoLab).*

---

To measure the electrode potentials and study the various possible cell reacts, the Autolab potentiostat by Metrohm is used throughout this work, as shown in Figure 3.6. The N-series Autolab potentiostat/galvanostat instruments are state of the art instrumentation that can be used for virtually all electrochemical applications. One of the important features of Autolab electrochemical instruments is the modularity. The basis of the instrument is a potentiostat/galvanostat, which can be further configured to one's needs by adding one or more of the available. NOVA is the new electrochemistry software from Metrohm Autolab. This application is used to control all compatible Autolab instruments and accessories. NOVA is a powerful and flexible software with a simple and modern user interface. The design of NOVA

is based on simple and effective graphical representations of common tasks that can be carried out by the instrument.

NOVA provides an extensive list of unique features:

- A simple, consistent and clear presentation
- A dashboard for all the relevant information
- Tabbed navigation throughout the application
- An extensive library of predefined methods
- An easy to use procedure editor for custom methods
- Powerful 2D and 3D plotting options
- A wide range of data analysis and data handling tools
- A seamless transition from procedure to data and the other way around
- A powerful procedure scheduler
- Multi Autolab support up to 128 instruments from one computer
- Manual control options of all supported instruments

### **3.3. Characterization Techniques**

The equipment used for the characterization of thin films and hybrid structures in this research work are demonstrated briefly in the following sections.

#### **3.3.1. X-Ray Diffraction Measurement**

X-Ray diffraction (XRD) is an important technique to examine the crystallinity, phase, strain, and preferred orientation, etc. of samples [4]. A collimated beam of X-Rays was incident on a sample and diffracted by the crystalline phases in the sample according to Bragg's law such that:

$$n\lambda = 2d \sin\theta \quad (3.1)$$

where  $\lambda$  is the wavelength of the incident X-Ray beam,  $d$  is the inter-plane separation of lattice between atomic planes in the crystalline phase,  $\theta$  is the angle between atomic planes and the incident X-Rays

beam and  $n$  is an integer that represents the interference order (Figure 3.7).

The intensity of the diffracted X-Rays is measured as a function of the diffraction angle  $2\theta$ . This diffraction pattern is used to identify the sample crystal orientation [4]. It is well known that atoms of a pure solid

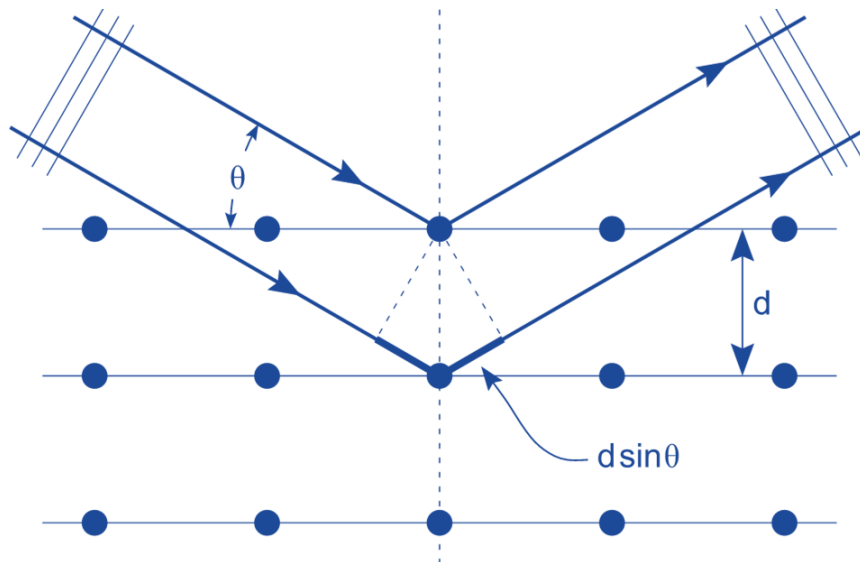


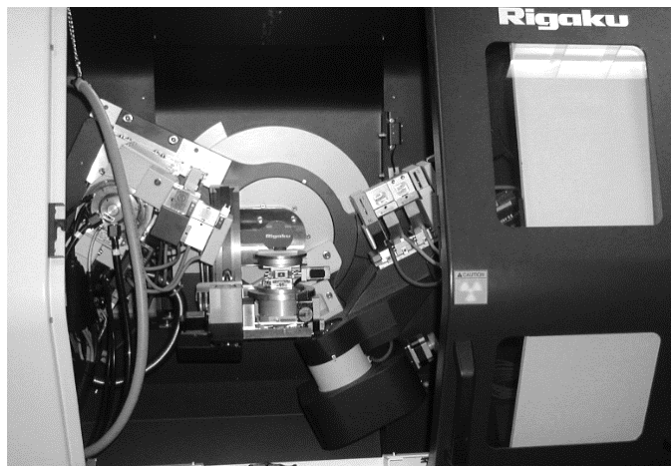
*Figure 3.7. Basic principle of XRD diffraction.*

are arranged in a regular periodic pattern called ‘lattice.’ The interatomic distance and interaction of atoms in any crystalline lattice is unique and results in a unique XRD pattern to identify its crystal structure. The XRD patterns include peak position and intensity of the diffracted beam, which provides a variety of information about the samples.

In this research work, the crystal structure of ZnO and the ZnO based hybrid thin films were characterized using Rigaku SmartLab, Automated Multipurpose X-Ray Diffractometer equipped with a copper target (Cu-K $\alpha$ ) to generate the incident X-Rays of wavelength  $\lambda = 0.154178$  nm for the diffraction measurement in Bragg Brentano configuration. The actual image of this XRD system is shown in Figure 3.8.

### 3.3.2. *Field Emission Scanning Electron Microscopy*

Field emission scanning electron microscope (FE-SEM) is commonly used for analyzing morphological properties of the sample under observation. FE-SEM is considered as a very powerful microscopic technique which provides 100000 times magnified image of the sample [5]. The FE-SEM mainly involves four components: (a) an electron source known as electron gun, (b) an electron condenser lens which controls the size of the electron beam, (c) XY deflection coils to move



---

*Figure 3.8. Photograph of Rigaku SmartLab, Automated Multipurpose X-Ray Diffractometer.*

the electron beam in a controlled fashion, and (d) the electron detectors. All components are fixed in a chamber, and this whole chamber is kept under ultra-high vacuum conditions. In FE-SEM system, a different type of electron source called Field Emission Gun is used for very high magnification. In this system, the source is not heated by the current; instead, an electric field is used to obtain the electrons from the source, which is a very sharp tungsten crystal or zirconium oxide. Here, the electrons have energy in the range of 1-40 KeV [5].

When the electron beam falls on the sample, it interacts with the atoms and the electron is slowed down due to strong elastic scattering. The atoms absorb the energy and get ionized. Some of the electrons from the sample atoms are released. These are called ‘secondary electrons’. They usually have lower energy (< 50 eV) compared to the primary electrons

from the electron gun. When the electron beam falls on the surface of sample, the electrons are scattered, and the beam diameter increases. Hence, in the beginning, it spreads like a cone and the area below the surface also is probed. The beam energy decreases as it goes deeper inside the sample. The number of secondary electrons produced also decreases. Besides, the electrons from the surface easily escape and arrive at the detector. The electrons from the bottom (trough) may be captured by other atoms before they escape to the surface. Hence only fewer secondary electrons from the trough come to the detector. Overall, the secondary electrons at the detector are essentially produced at the top of the surface. These secondary electrons are used to present the morphology and topography of the sample. The detector of instruments count the number of e-interactions and display to the screen whose intensity is determined by this number, producing the FE-SEM image [5], [6].

A ZEISS Supra<sup>55</sup> FE-SEM system was used to observe the surface morphologies of the undoped ZnO and ZnO based hybrid thin films. Figure 3.9 show the actual image of this FE-SEM system.



---

*Figure 3.9. Photograph of FE-SEM and EDX instrument, Zeiss Supra 55.*

---

### ***3.3.3. Energy Dispersive X-Ray Spectroscopy***

Energy Dispersive X-Ray Spectroscopy (EDS or EDX) is a chemical microanalysis technique used in conjunction with scanning electron microscopy (SEM). The EDX technique detects X-Rays emitted from the sample during the bombardment by an electron beam to characterize the elemental composition of the analyzed volume. Features or phases as small as 1  $\mu\text{m}$  or less can be analyzed [7].

When the sample is bombarded by the SEM's electron beam, electrons are ejected from the atoms comprising the sample's surface. The resulting electron vacancies are filled by electrons from a higher state, and an X-Ray is emitted to balance the energy difference between the two electrons' states. The X-Ray energy is characteristic of the element from which it was emitted.

The EDX X-Ray detector measures the relative abundance of emitted X-Rays versus their energy. The detector is typically lithium-drifted silicon, solid-state device. When an incident X-Ray strikes the detector, it creates a charge pulse that is proportional to the energy of the X-Ray. The charge pulse is converted to a voltage pulse (which remains proportional to the X-Ray energy) by a charge-sensitive preamplifier. The signal is then sent to a multichannel analyzer where the pulses are sorted by voltage. The energy, as determined by the voltage measurement, for each incident X-Ray is sent to a computer for display and further data evaluation. The spectrum of X-Ray energy versus counts is evaluated to determine the elemental composition of the sampled volume. Quantitative results can be obtained from the relative X-Ray counts at the characteristic energy levels for the sample constituents [7].

In this research work, the composition of different elements in ZnO based hybrids were characterized using energy dispersive X-Ray (EDX, Zeiss Supra 55).

### 3.3.4. Photoluminescence Measurement System

Photoluminescence is the optical emission obtained by photon excitation and is commonly observed with III-V semiconductor materials. This type of analysis allows non-destructive characterization of semiconductors [8], [9]. A light source (usually laser) possess the photon energy larger than the band-gap energy of the semiconductor under observation producing the electron-hole pairs within the semiconductor. The produced electron-hole pairs can be recombined via either radiative or non-radiative recombination. The light emitted from radiative recombination is detected by a detector which gives the photon count as a function of wavelength. The information of the energy band structure

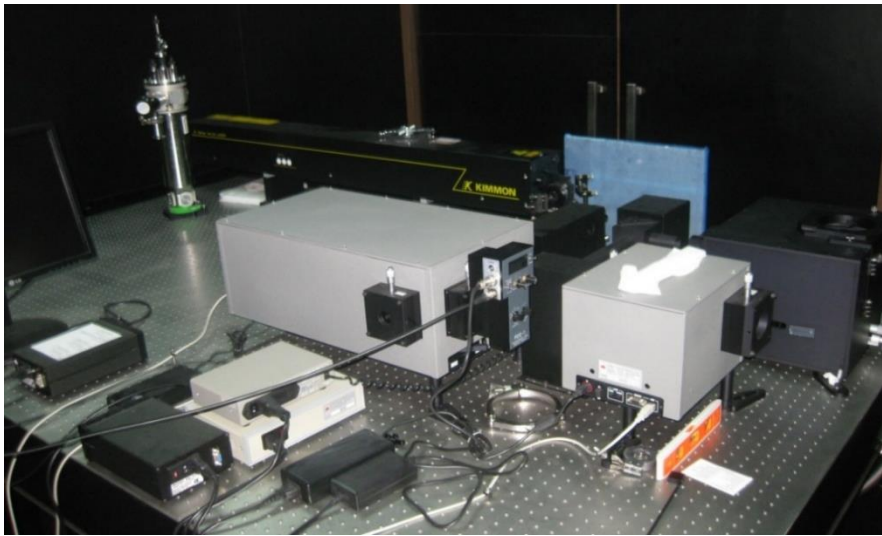


*Figure 3.10. Actual image of Photoluminescence Measurement Setup.*

of semiconductor and defect levels could be obtained from the analysis of PL spectra [8]. The peak emission in PL spectra correspond to transitions of electrons from conduction band minimum to valance band maximum and related to the band gap of the material.

In this research work, the luminescent properties of ZnO based films are measured by using Dong Woo Optron PL set-up, affixed with a 20 mW continuous wave (CW) He-Cd laser (excitation wavelength = 325 nm, TEM00 mode), monochromator, chopper, lock-in amplifier, and a photomultiplier tube (PMT) detector. All measurements were performed in a completely dark room. The image of PL spectroscopy experimental set-up is demonstrated in Figure 3.10

### 3.3.5. Variable Angle Variable Wavelength Spectroscopic Ellipsometry Measurement System

Ellipsometry technique measures a change in polarization as light reflects or transmits from a material structure [10], [11]. The polarization change is represented as an amplitude ratio,  $\Psi$ , and the phase difference,  $\Delta$ . The measured response depends on optical properties and thickness of individual materials. Thus, ellipsometry is primarily used to determine film thickness and optical constants. However, it is also applied to characterize composition, crystallinity, roughness, doping concentration, and other material



Figure 3.11. Photographic image of Variable Angle Variable Wavelength Spectroscopic Ellipsometry system.

properties associated with a change in optical response [10], [11]. The incident light is linear with both  $p$ - and  $s$ - components. The reflected light from the sample has undergone amplitude and phase changes for both  $p$ - and  $s$ - polarized light, and ellipsometry measures their changes. The change in polarization is the ellipsometry measurement, commonly written as:

$$\rho = \frac{r_p}{r_s} = \tan \psi e^{i\Delta} \quad (3.2)$$

where  $r_p$  and  $r_s$  are the amplitude reflection coefficients for the  $p$ - and  $s$ - polarized light, respectively,  $\tan(\Psi)$  is the ratio of the amplitude

reflection coefficients, and  $\Delta$  is the phase difference between  $s$ - and  $p$ -polarized light.

The primary components of the ellipsometry system are a light source, polarization generator, sample, polarization analyzer, and detector [10]. The polarization generator and analyzer are constructed of optical components that manipulate the polarization: polarizers, compensators, and phase modulators. In this research work, the thickness of thin films was measured by M-2000D J. A. Woollam Variable Angle Variable Wavelength Spectroscopic Ellipsometer. In this system, the measurement can be performed at different angles for the wavelength range of 200-1000 nm. The photographic image of Variable Angle Variable Wavelength Spectroscopic Ellipsometer is shown in Figure 3.11.



*Figure 3.12. Photographic image representation of HRTEM.*

---

### **3.3.6. High-Resolution Transmission Electron Microscopy**

To understand the operating principle of high-resolution transmission electron microscopy (HRTEM), one needs to first understand the operating principle of transmission electron microscopy (TEM). TEM is

a technique that uses the interaction of energetic electrons with the sample and provides morphological, compositional and crystallographic information. The electron emitted from filament passes through the multiple electromagnetic lenses and makes contact with the screen where the electrons are converted into light, and an image is obtained. The speed of electrons is directly related with the electron wavelength and determines the image resolution. A modern TEM is composed of an illumination system, a condenser lens system, an objective lens system, a magnification system, and the data recording system. A set of condenser lens that focuses the beam on the sample and an objective lens collects all the electrons after interacting with the sample and form image of the sample and determines the limit of image resolution. Finally, a set of intermediate lenses that magnify this image and projects them on a phosphorous screen or a charge coupled device (CCD). TEM can be used in imaging and diffraction mode [12].

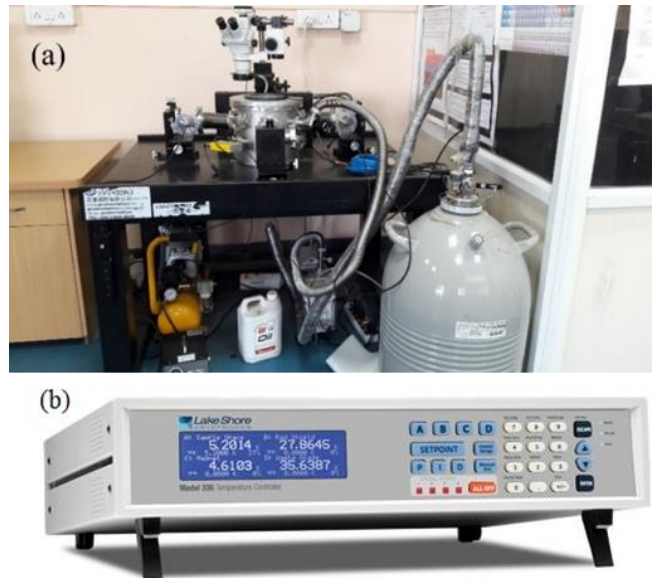
The high-resolution transmission electron microscopy (HRTEM) uses both the transmitted and the scattered beams to create an interference image. It is a phase contrast image and can be as small as the unit cell of the crystal. In this case, the outgoing modulated electron waves at very low angles interfere with itself during propagation through the objective lens. All electrons emerging from the specimen are combined at a point in the image plane. HRTEM has been extensively and successfully used for analyzing crystal structures and lattice imperfections in various kinds of advanced materials on an atomic resolution scale. It can be used for the characterization of point defects, stacking faults, dislocations, precipitates grain boundaries, and surface structures [12]. In this research work, the graphene quantum dots were studied using HRTEM. The photographic image of HRTEM is shown in Figure 3.12.

### **3.3.7. *I-V and C-V Measurement system***

The current-voltage (*I-V*) measurement is an important characterization to characterize the metal contact properties. It is used to identify ohmic and Schottky metal contact on the semiconductor. It is also used to evaluate contact properties like contact resistance in the case of ohmic

contact. For Schottky contact, it is used to determine the barrier height, ideality factor, and reverse saturation current. The details of  $I$ - $V$  characterization is present in later chapters of this thesis.

The capacitance-voltage ( $C$ - $V$ ) measurement method is used to determine the majority carrier concentration in semiconductors.  $C$ - $V$  measurements are capable of yielding quantitative information about the



---

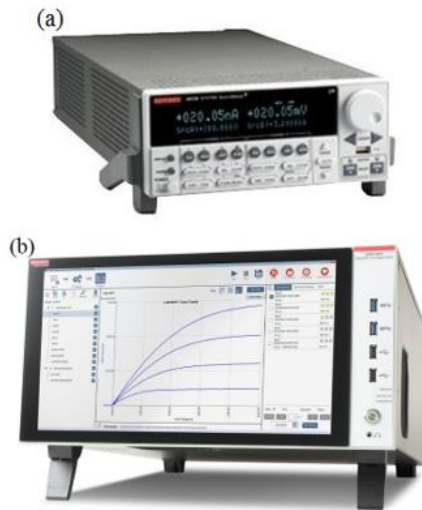
*Figure 3.13. Photographs of (a) probe station and (b) temperature controller.*

diffusion potential and doping concentration in semiconductor materials. The technique employs  $p$ - $n$  junctions, metal-semiconductor (MS) junctions (Schottky barriers), electrolyte-semiconductor junctions, metal-insulator-semiconductor (MIS) capacitors, and MIS field effect transistors (MISFETs).  $C$ - $V$  measurements yield accurate information about doping concentrations of majority carriers as a function of distance (depth) from the junction. The detail capacity of the  $C$ - $V$  characterization is present in [13].

Figure 3.13 and Figure 3.14 shows the photographic images of  $I$ - $V$  and  $C$ - $V$  measurement setup. The setup includes Everbeing cryogenic probe station with the temperature range of 80 K to 350 K, source meter Keithley 2612 A, and semiconductor parameter analyzer (4200A SCS).

In this research work,  $I$ - $V$  measurement is used to measure the light, and dark currents on Pt coated ZnO and its hybrid thin films. Also, the gas

---



---

Figure 3.14. Images of (a) Keithley 2612A and (b) Keithley 4200A semiconductor parameter analyzer.

---

sensing was done using the semiconductor parameter analyzer connected with extra Keithley.

### 3.4. Device Measurement Set-ups

#### 3.4.1. Incident Photon Conversion Efficiency

The spectral response of a photodetector device provides information on the physics at play at the device. The quantum efficiency (QE), also referred to as Incident Photon to Charge Carrier Efficiency (IPCE) - indicates the ratio of the number of photons incident on a solar cell to the number of generated charge carriers. In order to understand the conversion efficiency as a function of the wavelength of light impinging on the cell, the QE/IPCE measurement is critical for materials research and device design [18]. This measurement is performed by shining a monochromatic probe beam onto the sample and recording the photocurrent generated as a function of wavelength. The beam power of the probe is first characterized, using a detector of known responsivity. Subsequent measurement of the photocurrent generated by the device under test as a function of wavelength allows for the determination of

spectral responsivity. In this work, the fabricated photodetector devices were characterized using Bentham PVE300 IPCE system. The actual image of IPCE measurement set-up is shown in Figure 3.15.

The unique features of IPCE system are as below [18]

- (i) Optimized tunable light source based on xenon-quartz tungsten halogen dual source and single monochromator.
- (ii) Wide range of operation (300-2500nm).
- (iii) Reflective optics beam delivery to sample plane.

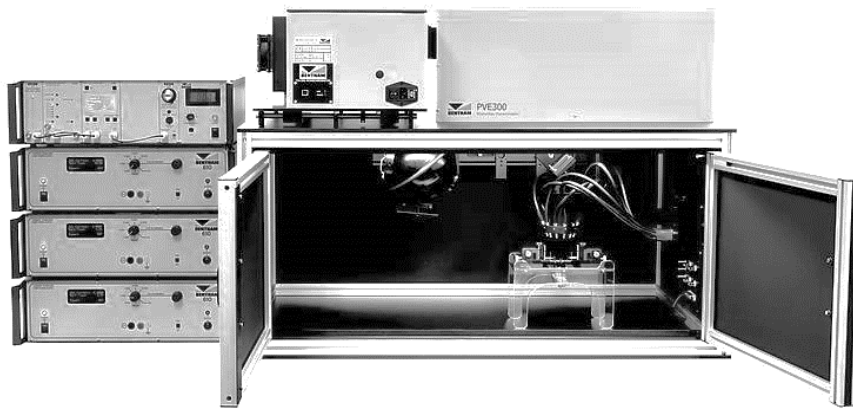


*Figure 3.15. Photograph of IPCE measurement setup.*

- (iv) A range of sample mounts and detection electronics to suit all device types and architectures.
- (v) Windows control software provides full automation via USB.
- (vi) Direct determination of device spectral response ( $\text{AW}^{-1}$ ).
- (vii) Direct determination of device external quantum efficiency (EQE %)
- (viii) Direct determination of total reflectance, R and transmittance, T.

### **3.4.2. Gas Sensing Set-up**

Gas sensing properties of the devices in this work has been measured with gas sensing setup which consist of one customized stainless steel chamber (volume roughly 500 cc) with heater system installed in it, two mass flow controller, one mixer chamber and two gas cylinders as

shown in Figure 3.16. Response of the device has been formulated as  $R_a/R_g$  for a gas, where  $R_a$  is resistance in air and  $R_g$  is resistance in gas. In this setup, for measuring sensor response in different gas concentrations, synthetic air was mixed in the mixer chamber through mass flow controller, and finally, mixed concentration was carried out to sensing chamber. For determining optimum temperature of operation, heater system has been used to heat the sample, controlled by an external PID temperature controller. For measuring DC resistance change, a resistance meter Keithley 2612-A has been used. Finally Keithley has been calibrated to personal computer for automatic data collection.

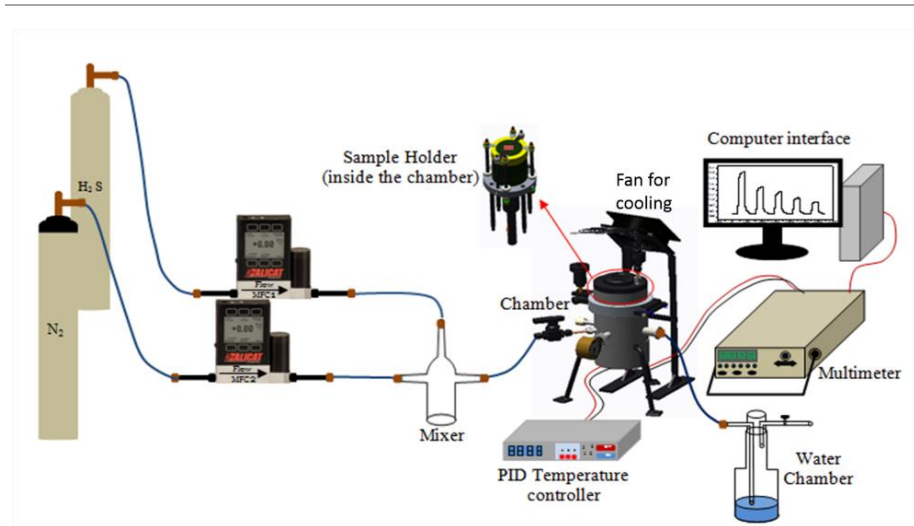


Figure 3.16. Gas sensing setup.

### 3.5. References

- [1] S. Kumar Pandey, S. Kumar Pandey, V. Awasthi, A. Kumar, U. P. Deshpande, M. Gupta, and S. Mukherjee, “p-type conduction from Sb-doped ZnO thin films grown by dual ion beam sputtering in the absence of oxygen ambient,” *J. Appl. Phys.*, vol. 114, no. 16, p. 163107, Oct. 2013.
- [2] F. Quaranta, A. Valentini, F. R. Rizzi, and G. Casamassima, “Dual- ion- beam sputter deposition of ZnO films,” *J. Appl. Phys.*, vol. 74, no. 1, pp. 244–248, Jul. 1993.

- [3] H. R. Kaufman, R. S. Robinson, and R. I. Seddon, "End- Hall ion source," *J. Vac. Sci. Technol. A Vacuum, Surfaces, Film.*, vol. 5, no. 4, pp. 2081–2084, Jul. 1987.
- [4] H. Kim, C. M. Gilmore, A. Piqué, J. S. Horwitz, H. Mattoussi, H. Murata, Z. H. Kafafi, and D. B. Chrisey, "Electrical, optical, and structural properties of indium–tin–oxide thin films for organic light-emitting devices," *J. Appl. Phys.*, vol. 86, no. 11, pp. 6451–6461, Dec. 1999.
- [5] L. Reimer, "Scanning Electron Microscopy: Physics of Image Formation and Microanalysis, Second Edition," *Meas. Sci. Technol.*, vol. 11, no. 12, pp. 1826–1826, Dec. 2000.
- [6] B. Bhushan and O. Marti, "Scanning Probe Microscopy -- Principle of Operation, Instrumentation, and Probes," in *Springer Handbook of Nanotechnology*, B. Bhushan, Ed. Berlin, Heidelberg: Springer Berlin Heidelberg, 2010, pp. 573–617.
- [7] S. T. D. Ellingham, T. J. U. Thompson, and M. Islam, "Scanning Electron Microscopy-Energy-Dispersive X-Ray (SEM/EDX): A Rapid Diagnostic Tool to Aid the Identification of Burnt Bone and Contested Cremains," *J. Forensic Sci.*, vol. 63, no. 2, pp. 504–510, Mar. 2018.
- [8] G. Weimann, "Vital volumes. Optical characterization of semiconductors: Infrared, raman and photoluminescence spectroscopy. By Sidney Perkowitz , harcourt brace, London 1993, X, 220 pp., hardcover, £ 40, ISBN 0-12-550770-4," *Adv. Mater.*, vol. 6, no. 10, pp. 804–804, Oct. 1994.
- [9] C. R. Brundle, C. A. Evans, and S. Wilson, *Encyclopedia of materials characterization: surfaces, interfaces, thin films*. Butterworth-Heinemann, 1992.
- [10] L. Arsov, M. Ramasubramanian, and B. N. Popov, "Ellipsometry," in *Characterization of Materials*, Hoboken, NJ, USA: John Wiley & Sons, Inc., 2012, pp. 1–11.

- [11] P. Sharma, Aaryashree, V. Garg, and S. Mukherjee, “Optoelectronic properties of phosphorus doped p-type ZnO films grown by dual ion beam sputtering,” *J. Appl. Phys.*, vol. 121, no. 22, p. 225306, Jun. 2017.
- [12] J. M. Howe, B. Fultz, and S. Miao, “Transmission Electron Microscopy,” in *Characterization of Materials*, Hoboken, NJ, USA: John Wiley & Sons, Inc., 2012, pp. 1–46.
- [13] P. A. Barnes, “Capacitance-Voltage (C-V) Characterization of Semiconductors,” in *Characterization of Materials*, Hoboken, NJ, USA: John Wiley & Sons, Inc., 2012.



# Chapter 4

## Photosensitive ZnO-Graphene Quantum Dot Hybrid Nanocomposite

### 4.1. Introduction

ZnO has accentuated its place among inorganic semiconductor oxides in both the physical and the engineering sciences. It has been extensively studied for the development of exciton-based optoelectronic devices such as light-emitting diode (LEDs) and photovoltaic cells because of its direct bandgap of 3.3 eV at room temperature and large exciton binding energy of 60 meV [1], [2]. Next-generation high-efficiency devices for optoelectronics and energy applications will primarily be based on nano-dimensional materials in the forms of quantum dots (QDs), quantum wires, and quantum wells. These nano-dimensional materials give rise to unique physical properties due to quantum confinement effect [3]. Recently, an overwhelming trend has been noticed worldwide to deploy organic-inorganic hybrid nanocomposite materials to realize such high-performance optoelectronic and energy devices and transferring the technology from conventional Si based substrates to cost-effective and flexible plastic and glass substrates. This revolutionary approach is expected to open several windows to achieve high-performance, flexible, transparent devices and modules with reduced cost-efficiency and better shock-absorbing capability [4], [5].

Lately, hybrid nanocomposite materials based on graphene-nano-dimensional structures have unfolded as promising candidates to fabricate such high-performance devices and modules. Graphene is well known to have unique electrical and optical properties. These properties, together with its abundance in nature, position graphene as a highly incipient next-generation conducting material. Graphene quantum dots

(GQDs) are tiny graphene fragments; where electronic transport is restrained in all three spatial dimensions [6]. GQDs have been fabricated by disintegration of graphene sheets (top-down approach), or with distinct molecular structure (bottom-up approach) [7]. Previous research work on GQDs were limited to the exploration of their physical properties [6]. More recently, GQDs have been chemically modified and prodigally used in applications of energy conversion, bio-analysis, and sensors [8]. Due to its preeminent electronic and optoelectronic properties GQDs have huge potential in nanoscale device applications such as next-generation electronic and optoelectronic devices such as LEDs and solar cells. GQDs have been reported to have low toxicity, excellent bio-compatibility, and are generally soluble in most of the solvents [11]. This serves as an aided advantage to the application of such ZnO-based hybrid GQD nanocomposites in areas of bio-imaging, pollutant detection [12], lithium ion batteries, super-capacitors [11], solar cells [13], gas sensors [14], and optoelectronic devices [15].

However, extensive research work has not yet been reported on the composite of these two fascinating inorganic (ZnO) and organic (GQD) hybrid materials. Research on GQD itself is still in a premature stage, and the full potential of this material has not yet been comprehended, and therefore, it is quite challenging to find literature on GQDs and ZnO concoction. The present work includes a comparative analysis of the properties of GQDs and ZnO-GQD organic–inorganic nanocomposite films deposited using simple electrochemical deposition process. We have investigated and comparatively associated the optical and structural properties of these films using various characterizations.

## **4.2. Experimental Details**

### **4.2.1. Experimental Layout**

The layout of the scheme of deposition of the structures is shown in Figure 4.1. Three films viz. ZnO, GQDs, and ZnO-GQD nanocomposite

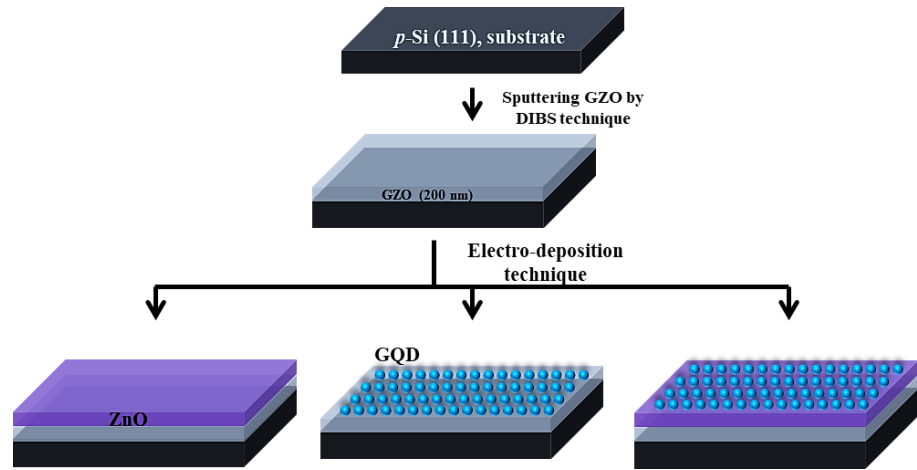


Figure 4.1. Layout of the scheme of deposition of the samples, ZnO, GQD and ZnO-GQD.

were grown using electrodeposition technique on Ga (3 at. %)-doped ZnO (GZO) coated high resistive Si (111) substrate. The parameters of deposition is tabulated in Table 4.1. Deposition of GZO on Si was performed by dual ion beam sputtering (DIBS) system [16].

Table 4.1. Deposition parameters for ZnO, GQD and ZnO-GQD.

Electrolyte	Voltage	Time	Temperature
	(V)	(Hr)	(°C)
<i>Aq. Zn(NO<sub>3</sub>).6H<sub>2</sub>O</i>	- 0.9	1	80
<i>Aq. GQD</i>	+ 2.0	1	80
<i>a) Aq. Zn(NO<sub>3</sub>).6H<sub>2</sub>O</i>	a) - 0.9	1	80
<i>b) Aq. GQD</i>	b) + 2.0		

The crystalline structure and morphology of the prepared samples were characterized by X-ray diffraction (XRD) using Rigaku SmartLab automated multipurpose X-ray diffractometer with Cu-K $\alpha$  radiation ( $\lambda = 1.54 \text{ \AA}$ ) and field emission scanning electron microscopy (FESEM) using Sigma Supra<sup>TM</sup> 55 of Carl Zeiss, respectively. The transmission electron microscopy (TEM) was done using JEOL electron microscope (model: JEM-2100), operated at an accelerating voltage of 200 kV. The photoluminescence (PL) spectrum of all three samples was obtained at room temperature by PL setup, affixed with 20 mW continuous wave He-Cd laser ( $\lambda = 325 \text{ nm}$ , TEM<sub>00</sub> mode), monochromator, chopper,

lock-in amplifier, and a photomultiplier (PMT) detector. For current-voltage (I-V) characteristics of the samples, cryogenic probe station with Keithley 2612A sourcemeter was employed. Optical parameters were obtained using the J. A. Woollam M-2000 variable-angle spectroscopic ellipsometry setup.

#### 4.2.2. Electrochemical Deposition

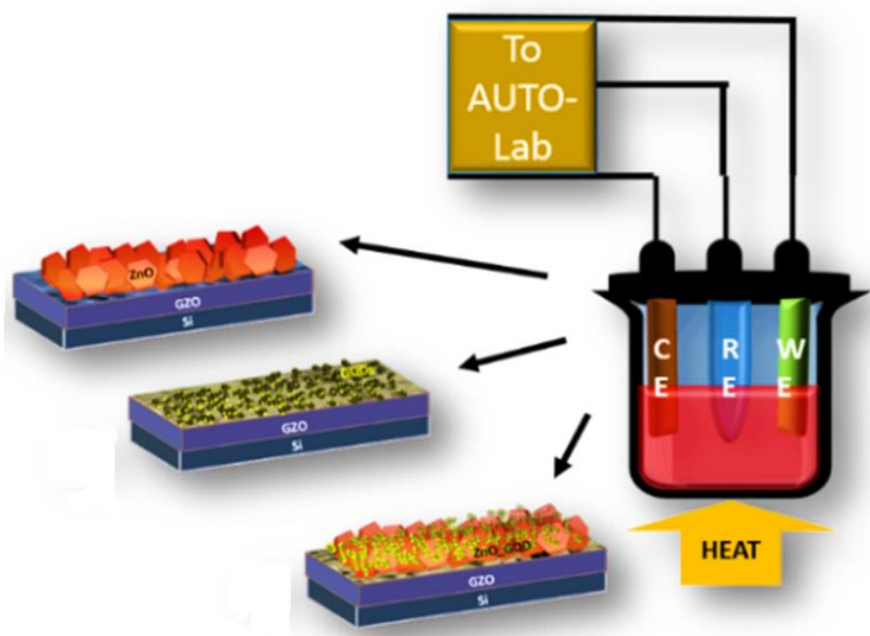


*Figure 4.2. The electrodeposition setup diagram. Here, CE is Counter Electrode, RE is Reference Electrode and WE is Working Electrode.*

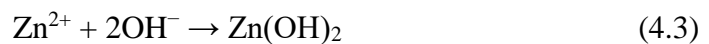
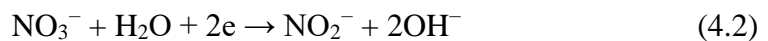
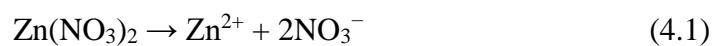
The schematic diagram of electrochemical deposition setup, as shown in Figure 4.2. The electrodeposition setup diagram. Here, CE is Counter Electrode, RE is Reference Electrode and WE is Working Electrode., was employed to grow hybrid nanocomposite structures. Prior to electrodeposition, the working electrodes were cleaned with DI water and purged with high-purity (99.999% pure) nitrogen gas. The conventional three electrode system was used to deposit GQD, ZnO and ZnO-GQD organic-inorganic nanocomposites onto the substrate with platinum (Pt) counter electrode and silver/silver chloride (Ag/AgCl) reference electrode. AUTOLAB, a computerised potentiostat was employed to perform the potentiostatic deposition. Voltammogram was

used to calculate the deposition potential. For the deposition of ZnO, the aqueous solution contained 0.2 M zinc nitrate hexahydrate ( $\text{Zn}(\text{NO}_3)_2 \cdot 6\text{H}_2\text{O}$ ) dissolved in DI water. The electrolyte was stirred constantly using a magnetic stirrer throughout the deposition and kept at a temperature of  $80\text{ }^\circ\text{C}$  ( $\pm 2\text{ }^\circ\text{C}$ ) for 1 hour at a potential of  $-0.9\text{ V}$ . To deposit ZnO-GQD hybrid nanocomposite, an aqueous solution of GQDs and  $\text{Zn}(\text{NO}_3)_2 \cdot 6\text{H}_2\text{O}$  were deposited for 1 hour at a potential of  $+2.0\text{ V}$  using 50 ml aqueous GQD solution with continuous stirring at a temperature of  $80\text{ }^\circ\text{C}$  ( $\pm 2\text{ }^\circ\text{C}$ ). Another sample was deposited using 50 ml aqueous GQD solution as electrolyte over GZO/Si working electrode. This deposition was also carried out for 1 hour at a temperature of  $80\text{ }^\circ\text{C}$  ( $\pm 2\text{ }^\circ\text{C}$ ) and with constant stirring of the electrolyte.

### 4.3. Results and Discussions:

#### 4.3.1. Voltammogram

The electrochemical behaviour of the samples was studied using the cyclic voltammetry to optimise the growth potential. The reactions that correspond to the electrochemical deposition process of growing ZnO from  $\text{Zn}(\text{NO}_3)_2$  aqueous solutions are mentioned in equations, [18]



Initially, the zinc nitrate salt dissolves to give rise to  $\text{Zn}^{2+}$  and  $\text{NO}_3^-$  ions in aqueous solution ((4.1). Then, the cathode reduction of nitrate ions release  $\text{NO}_2^-$  ions and  $\text{OH}^-$  ions near the cathode ((4.2). These  $\text{Zn}^{2+}$  ions and  $\text{OH}^-$  ions combine to form zinc hydroxide ((4.3). Finally, zinc hydroxide spontaneously dehydrates into ZnO, and  $\text{H}_2\text{O}$  ((4.4) as the solution temperature is higher than  $34\text{ }^\circ\text{C}$ . [19] Similarly, cyclic

voltammetry was done for GQD solution, and the voltammogram was obtained. A sharp peak is observed between 1.8 V and 2 V which implies the growth potential can be around these values.

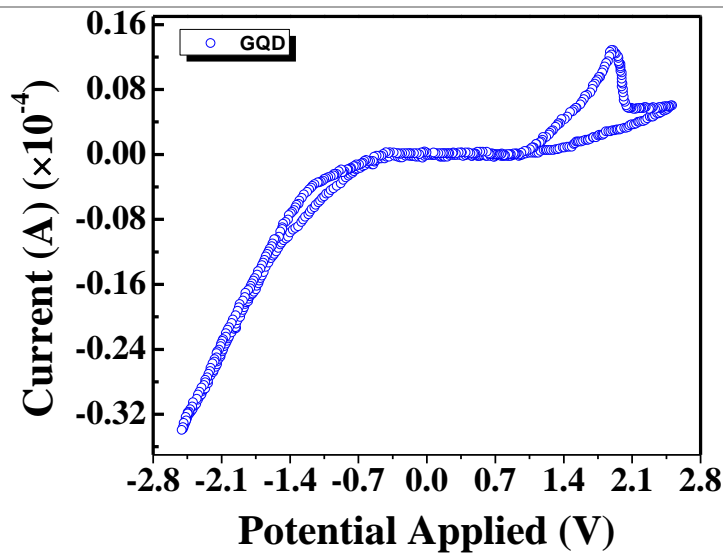


Figure 4.3. Cyclic voltammogram of GQD.

### 4.3.2. Morphology and Structure

#### 4.3.2.1. Field Emission Scanning Electron Microscopy

FESEM was used to examine the morphology of the films grown. FESEM images of ZnO, GQDs and ZnO-GQD nanocomposite samples are shown in Figure 4.4(a), Figure 4.4(c) and Figure 4.4(d), respectively.

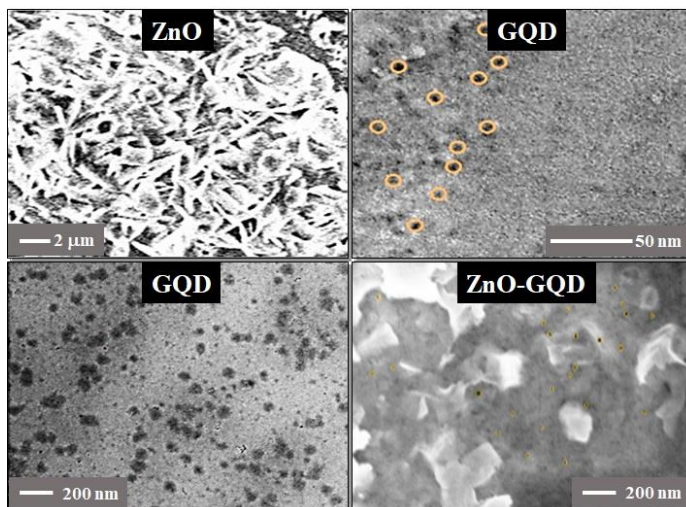


Figure 4.4. a), b), c) FESEM images of ZnO, GQD, and ZnO-GQD nanocomposite, respectively, d) TEM image of GQD individual sample.

In Figure 4.4(a), deposition of randomly oriented ZnO nano-sheets almost vertical to the substrate can be noticed. The GQDs deposited on the GZO substrate can be observed in Figure 4.4(c). However, owing to the reduced dimension of GQD, it is difficult to have a clear image of the particles deposited. Hence a TEM image of the GQD nanoparticles was taken and has been shown in Figure 4.4(b). The approximate size of the GQDs in the figure can be around 8-10 nm. Also, Figure 4.4(d) shows the SEM of ZnO-GQD hybrid nanocomposite film. To further confirm the anchorage of the above nanoparticles XRD analysis has been performed.

#### 4.3.2.2. X-ray Diffraction

For further confirmation of deposition of the nanoparticles and investigation of the crystallographic structure with preferred orientation, XRD patterns were recorded. The pattern of ZnO, GQDs and ZnO-GQD nanocomposite samples are presented in Figure 4.5. To enhance the small diffraction peaks, the intensity has been shown in log scale. XRD pattern shows that the ZnO crystal wurtzite structure with intense peak at  $34.5^\circ$  that can be indexed to (002) crystal plane. The weaker peak at  $\sim 44^\circ$  can be indexed to (102) reflections.[20] The angular position of Bragg's diffraction peak for ZnO (002) plane in the films deposited with and without GQD demonstrated no apparent difference. This reveals that the GQD deposition does not affect the orientation of the ZnO peaks over the studied preparative parameters. Similarly, the existence of the graphene layer along with the ZnO film is also confirmed by the appearance of both a broad, intense peak centred at  $2\theta \approx 25.6^\circ$  and a sharper peak at  $2\theta \approx 34.5^\circ$ , belonging to GQDs and ZnO, respectively.[15], [21], [22] However, in case of ZnO-GQD nanocomposite film, the relative intensity of the Bragg's diffraction peak for both ZnO (002) and GQD (002) is comparatively less than that of the individual diffraction peak of pure ZnO and GQD. This reduction in intensity value may be due to the formation of ZnO-GQD nanocomposites.

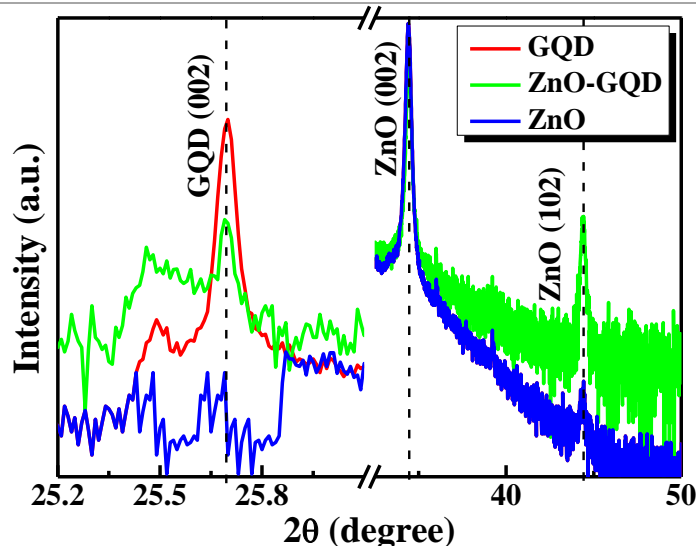


Figure 4.5. XRD peaks of ZnO, GQD and ZnO-GQD samples.

### 4.3.3. Optical Properties

#### 4.3.3.1. Photoluminescence

Room-temperature PL spectra of the ZnO\_GQD, GQDs, and ZnO structures are shown in Figure 4.6(a). The PL peak of ZnO is generally observed near ultraviolet (UV) region at ~370-385 nm.[23] In our case, the PL peak from ZnO is observed at 380 nm. Electrodeposition process might lead to a non-uniform film deposition with various intrinsic defects[24] which generally helps in producing a broad emission PL spectrum. ZnO film, primarily grown under oxygen rich conditions, begets most presumptive intrinsic defects like zinc vacancies, oxygen interstitial or the extrinsic defects like trapped OH<sup>-</sup>, some functional group impurities, etc.[25] The energy associate with the hydrogen related defects and intrinsic defects are in the range of 1.3-3.1 eV,[25], [26] which in our case is observed as 1.9-2.75 eV (450-650 nm), as observed in Figure 4.6(a).

GQDs are generally speculated to have a PL mechanism affected by their size, surface defects, and several functional groups that get introduced during the synthesis process. GQDs reported so far in the literature are luminescent, despite the fact that the exact origin of their luminescent behavior remain intangible.[12] Moreover, each GQD has some defects due to the incomplete reduction. It has been substantiated

that the root of these structural defects are the –OH, epoxy/ether, C=O and –CO–groups.[29] Nevertheless, the synthesis process of GQDs also determines their PL peaks. GQDs prepared in distinct ways can emit deep UV,[30] blue,[7], [15], [17], [31]–[33] green,[8], [29] yellow,[34] red,[35] and even white[33] PL. Various PL peaks ranging from 430 to 510 nm for GQD have been reported based on different excitations mechanism.[6] In our case, with the excitation of 325 nm, GQD exhibits a broad PL peak in the region of 340 to 560 nm, with a peak at 415 nm. These PL peaks are attributed from aromatic  $\pi$ - $\pi$  stacking interactions.[36]–[38]

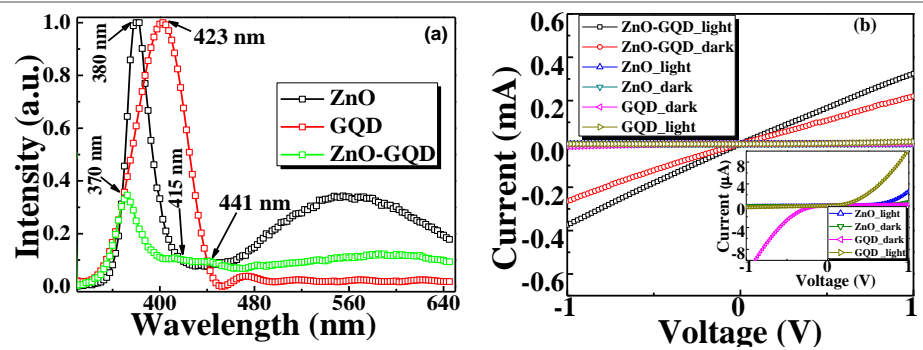


Figure 4.6. a) Room-temperature PL spectra of ZnO, GQD and ZnO-GQD nanocomposite, b) I-V characteristics of the samples under dark condition and illumination at room temperature. Inset shows the I-V of ZnO and GQD alone.

ZnO-GQD nanocomposite shows a distinct PL peak at 372 nm. Nevertheless, the peak look similar to the PL peak from ZnO. However, the spectral location of PL peak (380 nm) observed in ZnO film shows a marginal blue shift towards the UV region (~372 nm) in case of ZnO-GQD nanocomposite and the broad peak observed in GQD (340-560 nm) and ZnO (440-640 nm) is also evident in nanocomposite with suppressed intensity. This partial retention of the distinct component properties in PL is possibly due to the fact that the defects and the surface states of both ZnO and GQDs might be at play for the consequential alteration. As GQDs have various functional groups on the surface, on illuminating its surface, the emission is subjugated by a surface state emissive trap.[7], [30] Also, these functional groups attach themselves

to the inorganic molecules (ZnO) and may alter the emission. Hence, when mixed with ZnO, a characteristic PL curve is obtained. The smaller shoulder peaks at 415 and 441 nm are also observed in case of the ZnO-GQD nanocomposite PL spectra[39] which may be elucidated as being related to functionalization of the GQDs present in the nanocomposite sample.

#### 4.3.3.2. Current-Voltage (I-V) Characteristics

I-V characteristics of all three samples were studied under both dark and irradiated conditions. Two indium-ohmic contacts, separated by a distance of 10 mm were made on the surface of all the three samples. The samples were then, individually illuminated by a 150 W halogen lamp and the bias voltage was varied from -1 V to +1 V using Keithley sourcemeter. Figure 4.6(b) shows the I-V characteristics of the samples. All the three samples show similar behavior of photocurrent variation. Both the dark and the irradiated currents increase linearly with increasing bias voltage. It is observed from Figure 4.6(b) that ZnO alone and GQD alone give rise to insignificant current variation with the change in voltage. However, in the case of ZnO-GQD organic-inorganic nanocomposite, there is a comparatively larger magnitude of current variation with the change in bias voltage. This implies that the intercalation of the organic GQDs improves the I-V characteristics of the inorganic ZnO, as more number of charge carriers are generated in the nanocomposite. Such a remarkable enhancement in the I-V characteristics, i.e., indirectly an improvement in conductivity, would reduce the series resistance and facilitate charge transport.[40] This phenomenon is an indication to use such hybrid nanocomposite in the fabrication of optoelectronic devices that make use of linear I-V characteristics.

The photosensitivity (S) of the samples can be calculated using the equation (4.5), [34], [35]

$$S = \frac{I_{\text{light}} - I_{\text{dark}}}{I_{\text{dark}}} \quad (4.5)$$

where,  $I_{\text{light}}$  and  $I_{\text{dark}}$  indicate photo-illuminated and dark currents, respectively. Photosensitivity of the three samples was calculated at the bias of +1 V. The values of photosensitivity of ZnO, GQD, and ZnO-GQD nanocomposite were found to be 6.77, 51, and 99.32, respectively at room temperature. The enhancement of photosensitivity of ZnO-GQD nanocomposite was 1.9-fold and 14.67-fold as compared to that of GQDs and ZnO, respectively. This enhanced photosensitivity of the nanohybrids can hold immense potential for the application in UV-Vis optoelectronic devices.

#### 4.3.3.3. Spectroscopic Ellipsometry (SE)

Spectroscopic ellipsometry is a tool to probe into the optical response of materials. Analysis of the change in polarization state, i.e., psi ( $\Psi$ ) and delta ( $\Delta$ ) of the reflected light from the surface of a film enables precise extraction of the optical constants of the material under study when fitted employing the various preloaded models in the software.[43] One can also get the absorption coefficient of the material through this ellipsometric data analysis.

Ellipsometric characterization of nanoparticles is performed by generalized ellipsometry or Mueller matrix ellipsometry. Mueller matrix ellipsometry offers the great advantage that depolarizing samples can also be analysed, where depolarization may arise due to irregularities of nanoparticle parameters (e.g., shape, size, and ordering) and from multiple scattering.[44] Change in nanoparticle parameters changes the optical properties such as dielectric function, optical band gap of material, etc. Additionally, the fact that the method of preparation and deposition of nanoparticles affects the band gap and optical emissions cannot be neglected. Hence, considering all these, the generalised ellipsometric data was acquired and the curves were fitted using general oscillators (GenOsc) model[43] and the surface roughness was modelled considering air voids in co-ordination with other layers based on Bruggeman effective medium approximation (EMA),[45] since the films grown can be considered anisotropic. For determination of absorption and optical parameters in the case of ZnO-GQD

nanocomposites, Cody-Lorentz and Lorentz models have been implemented to achieve better data fitting.[46] The spectra of  $\Psi$  and  $\Delta$  for ZnO, GQDs and ZnO-GQD nanocomposite for  $70^\circ$  as optical incident angle are depicted in Figure 4.7 (c) and (d). The fringe pattern below the ZnO band gap ( $\sim 3.3$  eV) is due to interference phenomenon between the wave fronts generated at the interfaces (air-ZnO/ZnO-GZO/GZO-Si).[47] On the contrary, less or no interference oscillations above band gap reveal light absorption due to inter-band transitions in GQDs and ZnO-GQD samples. The valley in  $\Psi$  primarily indicates thickness of the nanostructures.[46]

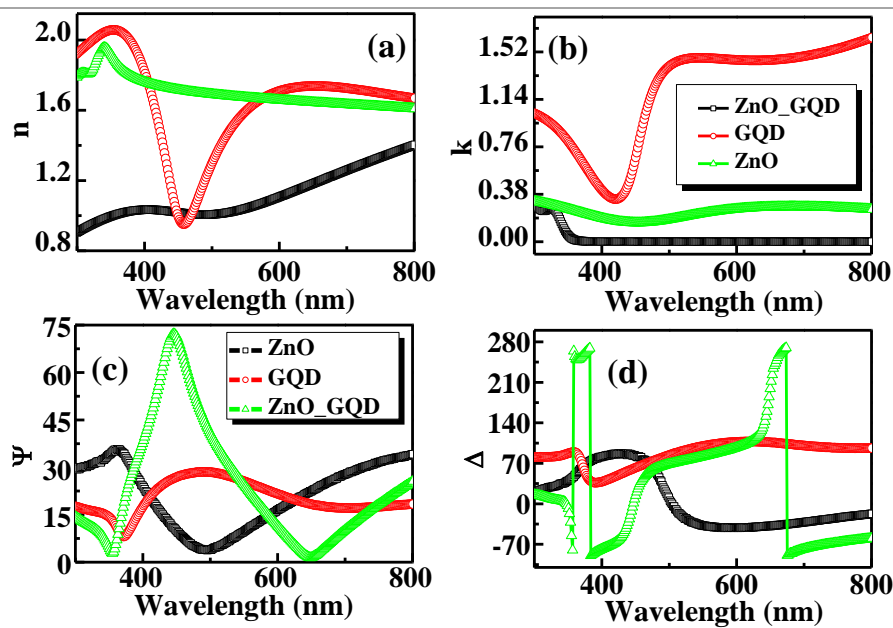


Figure 4.7. a)  $n$ , b)  $k$ , c)  $\Psi$ , and d)  $\Delta$  variation of ZnO, GQDs and ZnO-GQD nanocomposite.

The optical constants play an imperative role in scheming of the optoelectronic devices because they are closely associated to the electronic polarizability of ions and the local field inside the material.[48] Figure 4.7(a) and (b) show the refractive index ( $n$ ) and extinction coefficient ( $k$ ) of the nanostructures grown, which is obtained by data conversion using the respective  $\Psi$  and  $\Delta$  values. The value of  $n$  is seen to be always high in case of ZnO-GQD nano-hybrid material in comparison to that of ZnO. However, in case of GQDs, the value of  $n$  demonstrates variation with the change in optical energy. Since quantum

dots are directly deposited on the substrate, the substrate plays an important role in determination of the optical parameters. The value of  $k$  of ZnO-GQD composite nanohybrids can be seen to be reducing to zero for wavelength  $> 360$  nm. This indicates that ZnO-GQD composite nanohybrids are optically more transparent and lossless as compared to pure organic (GQDs) and inorganic (ZnO) samples. As in Figure 4.7(b), both ZnO and GQD show comparatively higher  $k$  values in the visible region pertaining to their high absorption in this region.

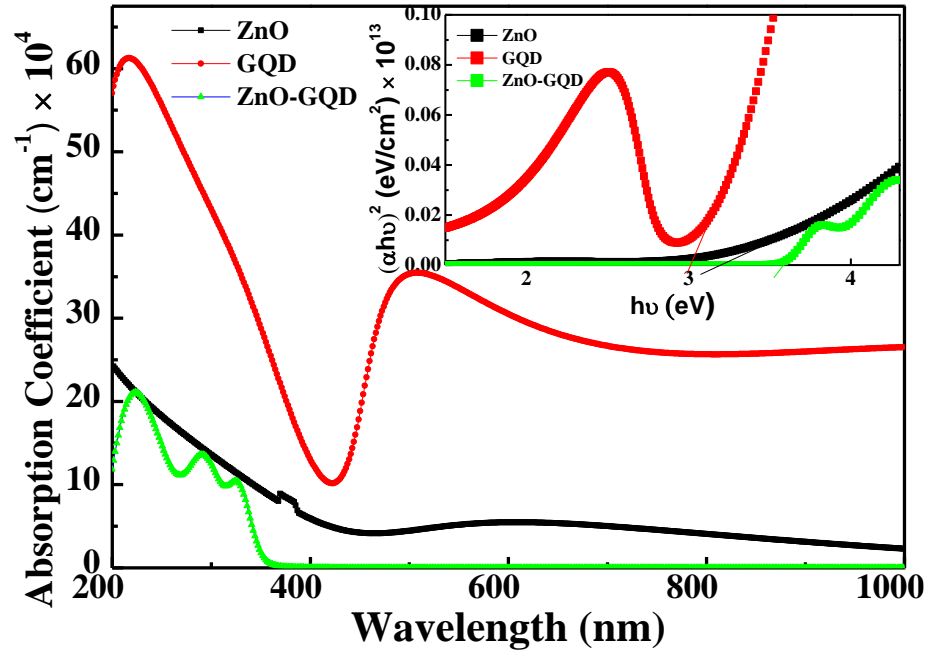


Figure 4.8. Spectral variation of absorption coefficient of ZnO, GQDs and ZnO-GQD nanocomposite as fitted from SE. Inset shows corresponding Tauc's plots.

Figure 4.8 shows the absorption coefficient ( $\alpha$ ) and the evaluation of energy band gaps of the three samples under consideration. The band gaps were calculated using equations (4.6) and ((4.7),[49]

$$(\alpha h\nu)^2 = A (E - E_g) \quad (4.6)$$

$$\alpha = \frac{4\pi k}{\lambda} \quad (4.7)$$

where  $A$  is a constant,  $E_g$  is the optical band gap, and  $\lambda$  is the wavelength.  $E_g$  is determined by extrapolation in the Tauc's plot at which  $(\alpha h\nu)^2 =$

0.[49] The values of optical band gap for ZnO, GQD, and ZnO-GQD nanostructure, as obtained from PL and SE data analysis are summarized in Table 4.2. The most interesting feature of the absorption peak is the sudden shooting up of the peak before the bandgap region in case of GQD and ZnO-GQD nanocomposite samples. This phenomenon can be attributed to the excitonic behaviour of the GQDs. Excitons in graphene have an interminable Bohr diameter, resulting in quantum confinement effects when scaled down to QDs of any defined size.[50] In general, the absorption spectra of GQDs have been reported to show a prominent peak at ~230 nm, accredited to the  $\pi \rightarrow \pi^*$  excitation of the aromatic  $sp^2$  domains.[30] However, in our case, this exciton peak is observed at ~220 nm. In addition to this, ZnO-GQD nanocomposite shows absorption peaks at 290 and 325 nm which are attributed for  $n-\pi^*$  transition of C=O bonds.<sup>48</sup> As compared to film with GQD alone, in ZnO-GQD nanocomposite film, these peaks are less pronounced confirming a correlation between ZnO and GQD nanoparticles.

*Table 4.2. Bandgap of the ZnO, GQD and ZnO\_GQD nanocomposite as obtained from PL and SE measurements.*

<b>Sample</b>	<b>MSE</b>	<b>Bandgap from PL at room temperature (eV)</b>	<b>Bandgap from SE at room temperature (eV)</b>
<b>ZnO</b>	18.17	3.26	3.20
<b>GQD</b>	15.49	2.93	3.01
<b>ZnO-GQD</b>	16.06	3.33	3.55

#### **4.4. Conclusion**

In summary, we have made an effort to demonstrate a simple and facile methodology, i.e., electrodeposition for synthesizing GQD and ZnO-GQD nanocomposite films. The effect of addition of GQD to ZnO has been established through characterization techniques such as PL, FESEM, I-V characteristics and SE measurements. Studies revealed that the GQDs play a significant role in shifting the PL peaks of the films.

Observations also concluded that the ZnO-GQD nanocomposites, in comparison to the ZnO and GQD individual films, produced higher optical band gap (3.33 eV). The electrical measurements also showed improved current sensitivity of the ZnO-GQD hybrid nanocomposites film over pure organic GQD and inorganic ZnO film. It can be expected that with further study on this nanocomposites, it will be easier to put this environmentally benign nanocomposites material for various applications in electronics.

#### 4.5. References

- [1] X. W. Sun, J. Z. Huang, J. X. Wang, and Z. Xu, "A ZnO nanorod inorganic/organic heterostructure light-emitting diode emitting at 342 nm.," *Nano Lett.*, vol. 8, no. 4, pp. 1219–23, Apr. 2008.
- [2] J. J. Cole, X. Wang, R. J. Knuesel, and H. O. Jacobs, "Integration of ZnO microcrystals with tailored dimensions forming light emitting diodes and UV photovoltaic cells.," *Nano Lett.*, vol. 8, no. 5, pp. 1477–81, May 2008.
- [3] M. A. El-Sayed, "Small is different: shape-, size-, and composition-dependent properties of some colloidal semiconductor nanocrystals.," *Acc. Chem. Res.*, vol. 37, no. 5, pp. 326–33, May 2004.
- [4] T. J. Booth, P. Blake, R. R. Nair, D. Jiang, E. W. Hill, U. Bangert, A. Bleloch, M. Gass, K. S. Novoselov, M. I. Katsnelson, and A. K. Geim, "Macroscopic graphene membranes and their extraordinary stiffness.," *Nano Lett.*, vol. 8, no. 8, pp. 2442–6, Aug. 2008.
- [5] Z. Dong, C. Jiang, H. Cheng, Y. Zhao, G. Shi, L. Jiang, and L. Qu, "Facile fabrication of light, flexible and multifunctional graphene fibers.," *Adv. Mater.*, vol. 24, no. 14, pp. 1856–61, Apr. 2012.
- [6] M. Bacon, S. J. Bradley, and T. Nann, "Graphene Quantum Dots," *Part. Part. Syst. Charact.*, vol. 31, no. 4, pp. 415–428, Apr. 2014.
- [7] R. Liu, D. Wu, X. Feng, and K. Müllen, "Bottom-up fabrication of

- photoluminescent graphene quantum dots with uniform morphology,” *J. Am. Chem. Soc.*, vol. 133, no. 39, pp. 15221–3, Oct. 2011.
- [8] Y. Li, Y. Hu, Y. Zhao, G. Shi, L. Deng, Y. Hou, and L. Qu, “An electrochemical avenue to green-luminescent graphene quantum dots as potential electron-acceptors for photovoltaics,” *Adv. Mater.*, vol. 23, no. 6, pp. 776–80, Feb. 2011.
- [9] J. M. Caruge, J. E. Halpert, V. Wood, V. Bulović, and M. G. Bawendi, “Colloidal quantum-dot light-emitting diodes with metal-oxide charge transport layers,” *Nat. Photonics*, vol. 2, no. 4, pp. 247–250, Mar. 2008.
- [10] P. O. Anikeeva, J. E. Halpert, M. G. Bawendi, and V. Bulović, “Electroluminescence from a mixed red-green-blue colloidal quantum dot monolayer,” *Nano Lett.*, vol. 7, no. 8, pp. 2196–200, Aug. 2007.
- [11] Y. Hu, Y. Zhao, G. Lu, N. Chen, Z. Zhang, H. Li, H. Shao, and L. Qu, “Graphene quantum dots–carbon nanotube hybrid arrays for supercapacitors,” *Nanotechnology*, vol. 24, no. 19, p. 195401, May 2013.
- [12] Z. Zhang, J. Zhang, N. Chen, and L. Qu, “Graphene quantum dots: an emerging material for energy-related applications and beyond,” *Energy Environ. Sci.*, vol. 5, no. 10, p. 8869, 2012.
- [13] M. Li, W. Ni, B. Kan, X. Wan, L. Zhang, Q. Zhang, G. Long, Y. Zuo, and Y. Chen, “Graphene quantum dots as the hole transport layer material for high-performance organic solar cells,” *Phys. Chem. Chem. Phys.*, vol. 15, no. 43, pp. 18973–8, 2013.
- [14] Y. Zhang, Z.-R. Tang, X. Fu, and Y.-J. Xu, “TiO<sub>2</sub>-graphene nanocomposites for gas-phase photocatalytic degradation of volatile aromatic pollutant: is TiO<sub>2</sub>-graphene truly different from other TiO<sub>2</sub>-carbon composite materials?,” *ACS Nano*, vol. 4, no. 12, pp. 7303–14, Dec. 2010.
- [15] D. I. Son, B. W. Kwon, D. H. Park, W.-S. Seo, Y. Yi, B. Angadi,

- C.-L. Lee, and W. K. Choi, "Emissive ZnO-graphene quantum dots for white-light-emitting diodes," *Nat. Nanotechnol.*, vol. 7, no. 7, pp. 465–471, May 2012.
- [16] S. K. Pandey, S. K. Pandey, S. Verma, M. Gupta, V. Sathe, and S. Mukherjee, "Investigation of dual ion beam sputtered transparent conductive Ga-doped ZnO films," *J. Mater. Sci. Mater. Electron.*, vol. 24, no. 12, pp. 4919–4924, Sep. 2013.
- [17] D. Pan, J. Zhang, Z. Li, and M. Wu, "Hydrothermal route for cutting graphene sheets into blue-luminescent graphene quantum dots," *Adv. Mater.*, vol. 22, no. 6, pp. 734–8, Feb. 2010.
- [18] B. Illy, B. a Shollock, J. L. Macmanus-Driscoll, and M. P. Ryan, "Electrochemical growth of ZnO nanoplates," *Nanotechnology*, vol. 16, no. 2, pp. 320–324, 2005.
- [19] A. Goux, T. Pauporté, J. Chivot, and D. Lincot, "Temperature effects on ZnO electrodeposition," *Electrochim. Acta*, vol. 50, no. 11, pp. 2239–2248, Apr. 2005.
- [20] C. Yilmaz and U. Unal, "Synthesis and Characterization of Hierarchical ZnO Structures by a Single-Step Electrodeposition under Hydrothermal Conditions," *Electrochim. Acta*, vol. 123, pp. 405–411, 2014.
- [21] X. Liang, Y. Ren, S. Bai, N. Zhang, X. Dai, X. Wang, H. He, C. Jin, Z. Ye, Q. Chen, L. Chen, J. Wang, and Y. Jin, "Colloidal Indium-Doped Zinc Oxide Nanocrystals with Tunable Work Function: Rational Synthesis and Optoelectronic Applications," *Chem. Mater.*, vol. 26, no. 17, p. 140807152509004, Sep. 2014.
- [22] Q. Chen, Y. Hu, C. Hu, H. Cheng, Z. Zhang, H. Shao, and L. Qu, "Graphene quantum dots–three-dimensional graphene composites for high-performance supercapacitors," *Phys. Chem. Chem. Phys.*, vol. 16, no. 36, p. 19307, Jul. 2014.
- [23] C. V. Manzano, D. Alegre, O. Caballero-Calero, B. Alén, and M. S. Martín-González, "Synthesis and luminescence properties of electrodeposited ZnO films," *J. Appl. Phys.*, vol. 110, no. 4, p. 17,

2011.

- [24] P. a. Rodnyi and I. V. Khodyuk, "Optical and luminescence properties of zinc oxide (Review)," *Opt. Spectrosc.*, vol. 111, no. 5, pp. 776–785, Dec. 2011.
- [25] E. V. Lavrov, F. Börrnert, and J. Weber, "Photoconductivity and infrared absorption study of hydrogen-related shallow donors in ZnO," *Phys. Rev. B*, vol. 72, no. 8, p. 085212, Aug. 2005.
- [26] E. V. Lavrov, J. Weber, F. Börrnert, C. G. Van de Walle, and R. Helbig, "Hydrogen-related defects in ZnO studied by infrared absorption spectroscopy," *Phys. Rev. B*, vol. 66, no. 16, p. 165205, Oct. 2002.
- [27] L. A. Ponomarenko, F. Schedin, M. I. Katsnelson, R. Yang, E. W. Hill, K. S. Novoselov, and A. K. Geim, "Chaotic Dirac billiard in graphene quantum dots.," *Science*, vol. 320, no. 5874, pp. 356–8, Apr. 2008.
- [28] T. Gokus, R. R. Nair, A. Bonetti, M. Böhmeler, A. Lombardo, K. S. Novoselov, A. K. Geim, A. C. Ferrari, and A. Hartschuh, "Making graphene luminescent by oxygen plasma treatment.," *ACS Nano*, vol. 3, no. 12, pp. 3963–8, Dec. 2009.
- [29] S. Zhu, J. Zhang, C. Qiao, S. Tang, Y. Li, W. Yuan, B. Li, L. Tian, F. Liu, R. Hu, H. Gao, H. Wei, H. Zhang, H. Sun, and B. Yang, "Strongly green-photoluminescent graphene quantum dots for bioimaging applications.," *Chem. Commun. (Camb)*, vol. 47, no. 24, pp. 6858–6860, 2011.
- [30] L. Tang, R. Ji, X. Cao, J. Lin, H. Jiang, X. Li, K. S. Teng, C. M. Luk, S. Zeng, J. Hao, and S. P. Lau, "Deep ultraviolet photoluminescence of water-soluble self-passivated graphene quantum dots.," *ACS Nano*, vol. 6, no. 6, pp. 5102–10, Jun. 2012.
- [31] J. Shen, Y. Zhu, X. Yang, and C. Li, "Graphene quantum dots: emergent nanolights for bioimaging, sensors, catalysis and photovoltaic devices.," *Chem. Commun. (Camb)*, vol. 48, no. 31, pp. 3686–99, Apr. 2012.

- [32] S. Zhuo, M. Shao, and S.-T. Lee, "Upconversion and downconversion fluorescent graphene quantum dots: ultrasonic preparation and photocatalysis.," *ACS Nano*, vol. 6, no. 2, pp. 1059–64, Feb. 2012.
- [33] V. Gupta, N. Chaudhary, R. Srivastava, G. D. Sharma, R. Bhardwaj, and S. Chand, "Luminescent graphene quantum dots for organic photovoltaic devices," *J. Am. Chem. Soc.*, vol. 133, no. 26, pp. 9960–3, Jul. 2011.
- [34] J. Peng, W. Gao, B. K. Gupta, Z. Liu, R. Romero-Aburto, L. Ge, L. Song, L. B. Alemany, X. Zhan, G. Gao, S. a Vithayathil, B. a Kaipparattu, a a Marti, T. Hayashi, J. J. Zhu, and P. M. Ajayan, "Graphene quantum dots derived from carbon fibers," *Nano Lett.*, vol. 12, no. 2, pp. 844–849, 2012.
- [35] M. L. Mueller, X. Yan, J. A. McGuire, and L. Li, "Triplet States and electronic relaxation in photoexcited graphene quantum dots.," *Nano Lett.*, vol. 10, no. 7, pp. 2679–82, Jul. 2010.
- [36] H. Sun, L. Wu, W. Wei, and X. Qu, "Recent advances in graphene quantum dots for sensing," *Mater. Today*, vol. 16, no. 11, pp. 433–442, Nov. 2013.
- [37] D. B. Rasale, S. Biswas, M. Konda, and A. K. Das, "Exploring thermodynamically downhill nanostructured peptide libraries: from structural to morphological insight," *RSC Adv.*, vol. 5, no. 2, pp. 1529–1537, Dec. 2015.
- [38] D. B. Rasale, I. Maity, and A. K. Das, "Lipase catalyzed inclusion of gastrodigenin for the evolution of blue light emitting peptide nanofibers.," *Chem. Commun. (Camb).*, vol. 50, no. 63, pp. 8685–8, Aug. 2014.
- [39] X. Li, M. Rui, J. Song, Z. Shen, and H. Zeng, "Carbon and Graphene Quantum Dots for Optoelectronic and Energy Devices: A Review," *Adv. Funct. Mater.*, p. 4929–4927, 2015.
- [40] Q. Chen, Y. Hu, C. Hu, H. Cheng, Z. Zhang, H. Shao, and L. Qu, "Graphene quantum dots-three-dimensional graphene composites

- for high-performance supercapacitors.,” *Phys. Chem. Chem. Phys.*, vol. 16, no. 36, pp. 19307–13, Sep. 2014.
- [41] P. J. George, A. Sanchez-Juarez, and P. K. Nair, “Modification of electrical, optical and crystalline properties of chemically deposited CdS films by thermal diffusion of indium and tin,” *Semicond. Sci. Technol.*, vol. 11, no. 7, pp. 1090–1095, Jul. 1996.
- [42] Y. Caglar, M. Caglar, S. Ilican, and A. Ates, “Morphological, optical and electrical properties of CdZnO films prepared by sol–gel method,” *J. Phys. D. Appl. Phys.*, vol. 42, no. 6, p. 065421, Mar. 2009.
- [43] S. Verma, M. K. Manna, S. K. Pandey, A. K. Das, and S. Mukherjee, “Benzo[ghi]perylene monoimide based photosensitive lamellar Cd-doped ZnO nanohybrids,” *RSC Adv.*, vol. 4, no. 107, pp. 62603–62614, 2014.
- [44] M. Losurdo, M. Bergmair, G. Bruno, D. Cattelan, C. Cobet, A. de Martino, K. Fleischer, Z. Dohcevic-Mitrovic, N. Esser, M. Galliet, R. Gajic, D. Hemzal, K. Hingerl, J. Humlicek, R. Ossikovski, Z. V Popovic, and O. Saxl, “Spectroscopic ellipsometry and polarimetry for materials and systems analysis at the nanometer scale: state-of-the-art, potential, and perspectives.,” *J. Nanopart. Res.*, vol. 11, no. 7, pp. 1521–1554, Oct. 2009.
- [45] D. A. G. Bruggeman, “Berechnung verschiedener physikalischer Konstanten von heterogenen Substanzen. I. Dielektrizitätskonstanten und Leitfähigkeiten der Mischkörper aus isotropen Substanzen,” *Ann. Phys.*, vol. 416, no. 7, pp. 636–664, 1935.
- [46] I. J. A. Wollam Co., “CompleteEASE™ Data Analysis Manual,” pp. 1–207, 2008.
- [47] G. Malandrino, M. Blandino, M. E. Fragala, M. Losurdo, and G. Bruno, “Relationship between Nanostructure and Optical Properties of ZnO Thin Films,” *J. Phys. Chem. C*, vol. 112, no. 26, pp. 9595–9599, Jul. 2008.

- [48] H. Neumann, W. Hörig, E. Reccius, H. Sobotta, B. Schumann, and G. Kühn, "Growth and optical properties of CuGaTe<sub>2</sub> thin films," *Thin Solid Films*, vol. 61, no. 1, pp. 13–22, Jul. 1979.
- [49] Q. H. Li, D. Zhu, W. Liu, Y. Liu, and X. C. Ma, "Optical properties of Al-doped ZnO thin films by ellipsometry," *Appl. Surf. Sci.*, vol. 254, no. 10, pp. 2922–2926, Mar. 2008.
- [50] L.-S. Li and X. Yan, "Colloidal Graphene Quantum Dots," *J. Phys. Chem. Lett.*, vol. 1, pp. 2572–2576, Apr. 2010.



## Chapter 5

### Devices Based on ZnO-OPV Nanocomposites

In the perspective of device fabrication, the hybrids containing conjugated organic moiety have been exploited in areas such as photodetectors, transistors, sensors, etc. Blending organic molecules with the inorganic network is seen to offer extra benefits such as tuning the optical spectra, the lifetime of trap states, sensitivity and response time. Sensitivity can be optimised by controlling the structure of nano-hybrids to maximize the density of organics bound to the inorganic surface and also minimize the turbulence and discontinuities in conduction through the permeating network.

In general, in the self-assembly of  $\pi$ -conjugated arrangements, various unambiguous interactions work concurrently, and the resulting strength gives way to many interconnected advances. This perspective inspired us to accomplish our goal of synthesizing self-assembled hybrid nanostructures having both electronically active organic (*i.e.*, OPV) and inorganic (ZnO) components. ZnO-based optoelectronic and sensing devices have rapidly gained momentum due to its inimitable properties such as high exciton binding energy, high radiation resistance, chemical and thermal stability in strident ambience, etc. Additionally, one amongst the most noteworthy properties of ZnO lies in its rich and precisely accessible nanostructures. Due to intrinsic absorption and fluorescence behaviors,  $\pi$ -conjugated OPVs are being widely used in the development of optoelectronics and photonics applications. The optoelectronic behaviour of OPVs can be tuned by chemical functionalization and external stimuli, *e.g.*, pH, solvent and temperature. Moreover, supramolecular architectures of functionalized OPVs, which are driven by hydrogen bonding as well as  $\pi$ - $\pi$  stacking interactions, are

highly conceived. Well-defined supramolecular architectures are of growing attraction for applications in optoelectronics and sensing.

## 5.1. ZnO-OPV Based Photodetector

### 5.1.1. Introduction

In agreement with the expedient material's properties, as discussed in *Chapter 2*, the present work reports, for the first time in literature, electrochemically deposited hybrid ZnO and OPV blended thin film. Electrodeposition is known to be a low-cost technique requiring no sophisticated instrumentation. It also has some added advantages such as low-temperature chemical processing, any permissible substrate shape, controllable film thickness and growth under normal laboratory conditions. However, besides shape and size, a highly ordered nanostructure enhances the performance of such devices.[1] Hence, this work reports, the self-assembly of an organic surfactant viz. dipeptide-functionalized OPV which interacts with inorganic ZnO forming ZnO-*f*-OPV nano-hybrids. The *f*-OPV contains functional acid groups at the terminals that can bind to zinc ions in the inorganic phase, and their hydrophobic segment is a conjugated moiety of OPV. The *f*-OPV enhanced the self-assembly of the hybrid owing to their tendency to form hydrogen bonding and  $\pi$ - $\pi$  stacking interactions. The acid functional group  $-\text{COO}^-$  of *f*-OPV covalently attaches on the growing ZnO and influences its structure and morphology. The present work aims to thoroughly examine the role of dipeptides present in *f*-OPV in modifying the properties of ZnO considering its ability to act as a template. Additionally, the chapter talks about the application of these hybrids as: a) UV photodetector, and b) ammonia gas sensor.

### 5.1.2. Experimental Section

#### 5.1.2.1. The Growth of Working Electrodes:

120 nm thick dual ion beam sputtered (DIBS) Indium Tin Oxide (ITO) thin films on glass substrates were used as electrodes. DIBS technique offers a distinct advantage of *in-situ* pre-cleaning of the substrate over other sputtering techniques. The technique ensures better compositional

stoichiometry and film adhesion to the substrate even for room temperature material growth. It offers high-quality growth with reduced surface roughness and better uniformity over the large surface area.[2] ITO thin films were deposited at 300 K by sputtering 99.99% pure 4-inch diameter ITO target disc for 5 hours in pure Ar ambience.

#### *5.1.2.2. Electrochemical Synthesis:*

Electrochemical syntheses were carried out in 24 mL solutions (1:1 (v/v) DMSO/H<sub>2</sub>O) of 0.02 M Zn(NO<sub>3</sub>)<sub>2</sub>·6H<sub>2</sub>O (Aldrich, 98%) with 2.0 mg organic surfactant using a three-electrode set-up (Autolab potentiostat) with a Pt counter electrode and an Ag/AgCl reference electrode.[3] Water is required for reduction of NO<sup>-3</sup> to generate OH<sup>-</sup>, and DMSO is added for surfactant solubility. Working electrode substrates (indium tin oxide (ITO)) were placed upright in the cell and deposition was achieved potentiostatically at -0.9 V for 30 min–20 h, depending on growth time, under constant magnetic stirring at 80 °C. Deposited films were rinsed with water and dried with dry N<sub>2</sub>. For device measurements and all other characterization, 2.5 cm × 2 cm ITO–glass (120 nm thin, grown by DIBS system) electrodes were used.

#### *5.1.2.3. Synthesis of Thin Film Standards:*

ZnO thin film was used as a standard for powder XRD, responsivity and I-V measurement. The conventional three electrode system was used to deposit ZnO onto the substrate (ITO coated glass) with platinum (Pt) counter electrode and silver/silver chloride (Ag/AgCl) reference electrode. AUTOLAB, a computerised potentiostat was employed to perform the potentiostatic deposition. For the deposition of ZnO, the aqueous solution contained 0.2 M zinc nitrate hexahydrate (Zn(NO<sub>3</sub>)<sub>2</sub>·6H<sub>2</sub>O) dissolved in DI water.[3] The electrolyte was stirred constantly throughout the deposition and kept at a temperature of 80 °C (± 2 °C) for 1 hour at a potential of -0.9 V.

#### *5.1.3. Device Characterization:*

The crystalline structure and morphology of the prepared samples were characterised by X-ray diffraction (XRD) using Rigaku SmartLab

automated multipurpose X-ray diffractometer with Cu-K $\alpha$  radiation ( $\lambda = 1.54 \text{ \AA}$ ) and field emission scanning electron microscopy (FESEM) using Sigma Supra<sup>TM</sup> 55 of Carl Zeiss, respectively. The photoluminescence (PL) spectra of all three samples were obtained at room temperature by PL setup, affixed with 20 mW continuous wave He–Cd laser ( $\lambda = 325 \text{ nm}$ , TEM<sub>00</sub> mode), monochromator, chopper, a lock-in amplifier, and a photomultiplier (PMT) detector. For current-voltage (I-V) characteristics of the samples, cryogenic probe station with Keithley 2612A sourcemeter was employed. The spectral response and the external quantum efficiency (EQE) of the devices were done on Bentham photovoltaic characterization system consisting of 150 W Xe lamp, chopper, monochromator, and a lock-in amplifier. Optical modeling was done using the J. A. Woollam M-2000 variable-angle spectroscopic ellipsometry setup.

#### **5.1.4. Results and Discussions**

##### *5.1.4.1. Morphology and Structure*

Figure 5.1(a) and 5.1(b) show field-effect scanning electron microscopy (FE-SEM) images of as-deposited structures of ZnO-OPV and ZnO-*f*-OPV respectively. For a typical synthesis, these structures are homogeneously deposited across the entire substrate with the nanostructures being randomly oriented and the structures in case of ZnO-*f*-OPV looked similar to ZnO nano-flakes. To determine the chemical composition of both the hybrid nanostructures, an energy dispersive X-ray (EDX) analysis has been performed. Figure 5.1(c) and 5.1 (d) show the EDX spectra ZnO-OPV and ZnO-*f*-OPV respectively. The spectra confirm the presence of C, N, O and Zn species in both nanohybrids. The presence of C and N in the organic has been used to determine the Zn/surfactant stoichiometry. EDX yielded Zn/C atomic ratio of 1.12 in ZnO-OPV and that of 0.28 in case of ZnO-*f*-OPV. Further, the Zn/N atomic ratios were 0.56 and 1.36 in case of ZnO-OPV and ZnO-*f*-OPV respectively. The compositional differences suggest a non-uniform chemical compatibility between ZnO and the two surfactants. X-ray diffraction (XRD) pattern of ZnO, ZnO-OPV and

ZnO-*f*-OPV is shown in Figure 5.1(d). In all the cases, (100), (002) and (101) diffraction peaks of ZnO are dominant. However, in case of ZnO-OPV and ZnO-*f*-OPV, the intensity of these peaks seems to be altered. Apart from the ZnO peaks, (005) and (006) reflections from the organic molecules are also quite prominent in case of ZnO-*f*-OPV. XRD measurements in the range of  $2\theta$  varying from  $2^\circ$  to  $6^\circ$  were also performed in order to confirm the presence of lamellar structure in ZnO-*f*-OPV nanohybrids. Figure 5.1(f) shows the X-ray scattering at small angles confirming the highly ordered lamellar structure with *d*-spacing

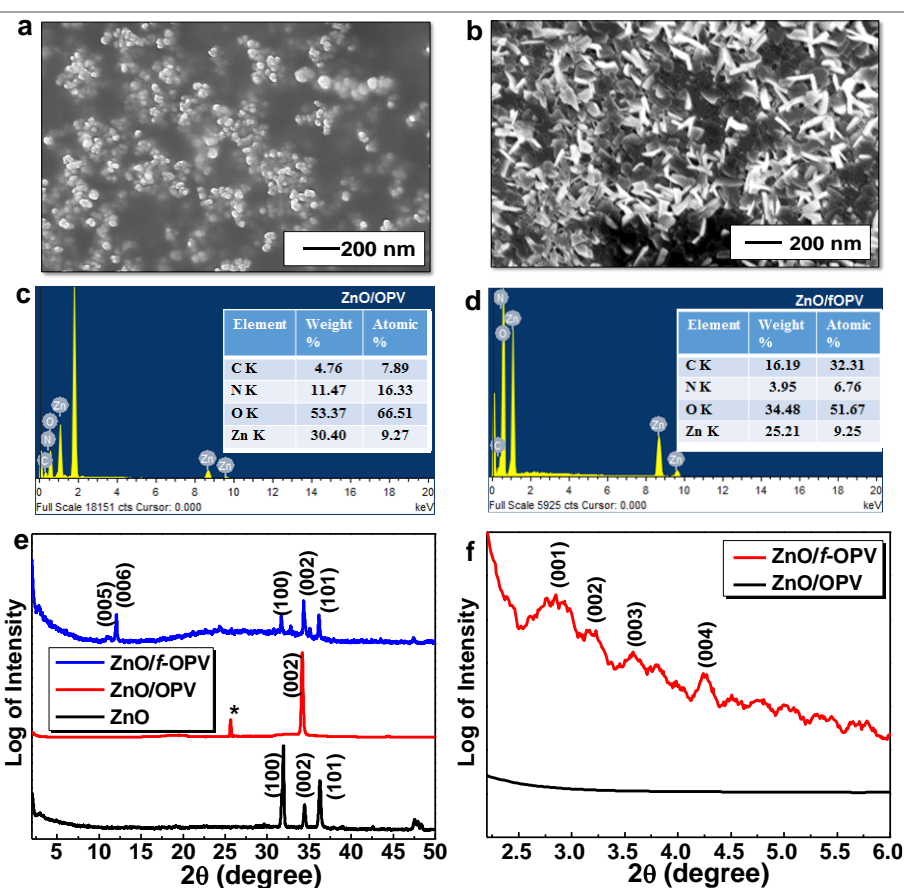


Figure 5.1. a) FE-SEM of ZnO-OPV hybrid, b) FE-SEM of ZnO-*f*-OPV hybrid, c) EDX image of ZnO-OPV, d) EDX image of ZnO-*f*-OPV, e) XRD pattern of ZnO, ZnO-OPV and ZnO-*f*-OPV hybrid compared. Asterisk (\*) represents some organic phase. f) XRD pattern of ZnO-OPV and ZnO-*f*-OPV hybrid at a smaller angle showing a lamellar structure of the ZnO-*f*-OPV hybrid.

of 32 Å, 28 Å, 25 Å and 21 Å corresponding to (001), (002), (003) and (004) reflections, respectively.

Interestingly, lamellar structures have been found to have profound application in optoelectronic devices[4], [5]; hence, we proceeded further, to fabricate a device based on ZnO-*f*-OPV.

#### 5.1.4.2. The Device Structure

Figure 5.2(a) shows the schematics of the fabricated device. The sensing layer has been varied consisting of a) ZnO b) ZnO-*f*-OPV hybrid in order to present a comparative analysis. Figure 5.2(b) shows the graphics of the energy level diagram of the photodetector under zero bias with sensing layer consisting of ZnO-*f*-OPV hybrid. The conduction band minima (-4.2 eV) and the valence band maxima (-7.6 eV) of ZnO have been taken from literature[6], [7]. The band gap of *f*-OPV having the HOMO level at -5.4 eV and the LUMO level at -2.2 eV has been calculated using density functional theory as discussed in Chapter 2. The band gap thus calculated is 3.2 eV for *f*-OPV and 3.4 eV for ZnO.

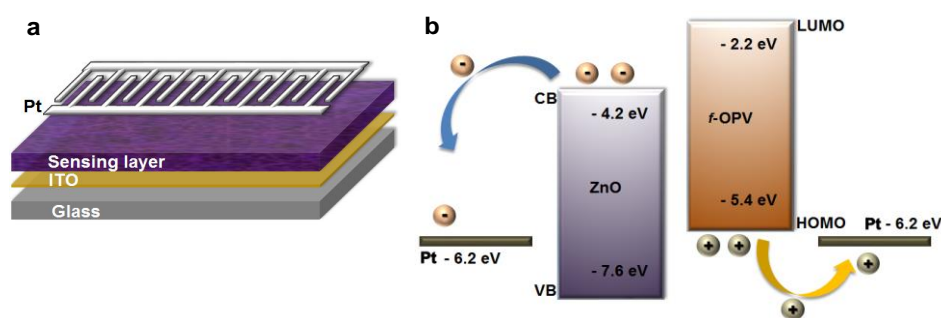


Figure 5.2. a) Schematic diagram of the fabricated device, b) Energy band diagram of photodetector under zero bias for the device with hybrid nanostructure as sensing (photo-detecting) layer.

#### 5.1.4.3. Device Performances

Figure 5.3 shows the complete summary of the performance measurement of hybrid nanocomposite based photodetector. Figure 5.3(a) shows the schematic of the Incident Photon-to-Current Efficiency (IPCE) measurement set-up. Responsivity, *R*, of a photodetector, can be

defined as a ratio of generated photocurrent ( $J_{ph}$ ) to the incident light intensity ( $L_{light}$ ) at a given wavelength. It is expressed as,

$$R = \frac{J_{ph}}{L_{light}} \quad (5.1)$$

where  $J_{ph}$  is the photocurrent and  $L_{light}$  is the incident light intensity. Further, R is proportional to the quantum yield of the photodetector, and therefore, high external quantum efficiency is essential. Figure 5.3(b) and 5.3(c) show responsivity curve on excitation with white light in the case of both ZnO and ZnO-f-OPV hybrid. However, it can be noticed that the highest responsivity of the hybrid ( $0.2 \text{ AW}^{-1}$ ) is 10 times greater than that of ZnO ( $0.02 \text{ AW}^{-1}$ ) at -20 V. Interestingly, the responsivity pattern in case of hybrid does not follow the same pattern as of its constituent (i.e., ZnO) but, becomes band selective.

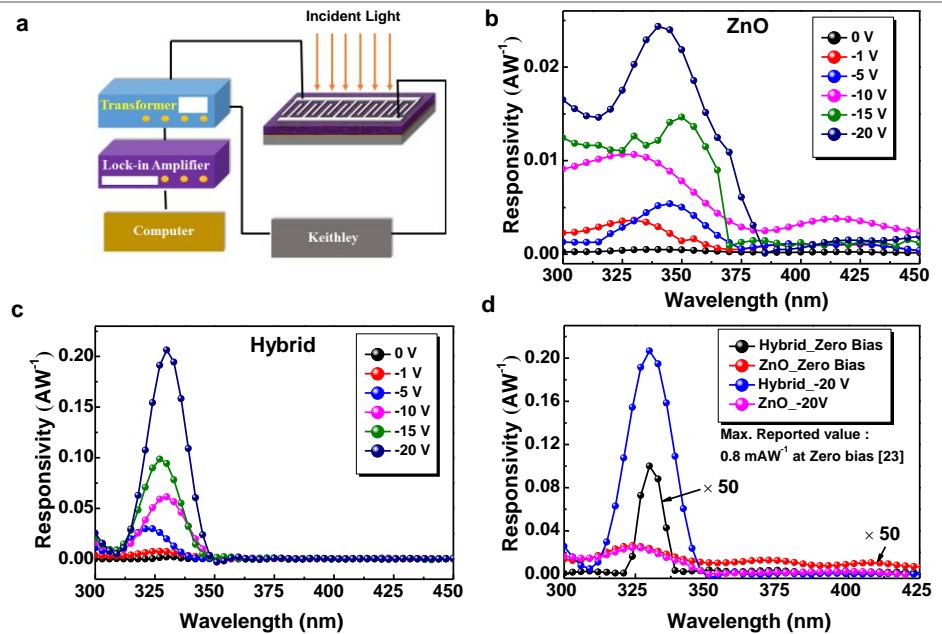


Figure 5.3. a) Schematic of IPC System, b) Responsivity of ZnO based detector c) Responsivity of ZnO-f-OPV hybrid based detector d) Responsivity of ZnO-f-OPV hybrid detector compared with ZnO detector at zero bias (responsivity at zero bias is  $\times 50$  times multiplied) and at a reverse bias of 20V.

Further, on increasing the reverse bias from zero to -20 V, the spectral response considerably incurred a blue shift and the response covered a

short wavelength of 320~350 nm which is a UV range. This phenomenon may be attributed to the lamellar structure so formed. To the best of our knowledge, the best-reported value of room-temperature responsivity of *f*-OPV based hybrid is 0.8 mA W<sup>-1</sup> at zero bias[8] which in our case is much higher at ~1.7 mA W<sup>-1</sup>. The comparison of the responsivity of the ZnO alone and hybrid device at zero bias and at -20 V bias has been mentioned in Figure 5.3(d).

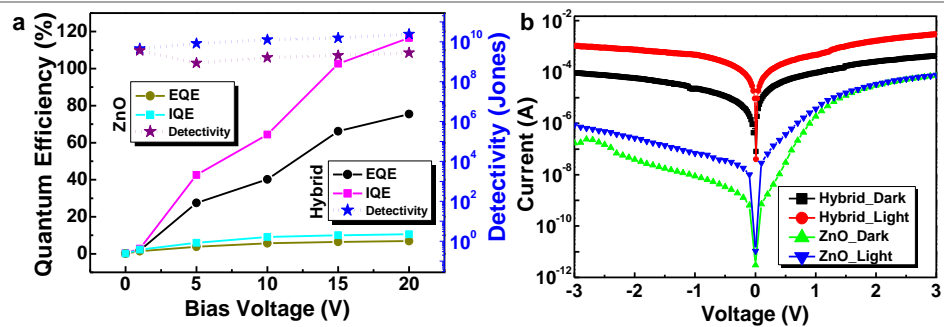


Figure 5.4. a) Comparison of the quantum efficiencies and the specific detectivity of ZnO alone and ZnO-*f*-OPV hybrid based detectors. b) Comparative analysis of I-V curves of sensing films of ZnO alone and ZnO-*f*-OPV hybrid.

Another critical parameter for a photodetector is its external quantum efficiency (EQE), which is the ratio of free charge carriers accumulated by the device to incident photons. EQE ( $\eta$ ) is obtained by measuring the photocurrent spectrum of the device under test and comparing it to the photocurrent spectrum of a calibrated photodetector (Si, in our case) as a reference, thereby removing the spectral characteristics of the test system. From our experimental results, maximum  $\eta$  for hybrid sample is calculated to be 75.5% at 20 V as plotted in Figure 5.4(a) which is much higher than that obtained for ZnO alone sample (6.83% at 20 V). Along with  $\eta$ , internal quantum efficiency (IQE) has also been plotted in Figure 5.4(a).

IQE was calculated by optical modeling[9] using spectroscopic ellipsometry (SE) and calculated as

$$IQE = \frac{\eta}{1 - \text{reflectance}} \quad (5.2)$$

The maximum IQE corresponding to the maximum EQE for hybrid sample was obtained to be approximately 116%, comparatively higher than IQE of 90% of a ZnO based hybrid recently reported by Benjamin *et al.*[10] Yet another important figure of merit for a photodetector is the specific detectivity ( $D^*$ ) that defines a photodetector in terms of its efficiency to detect the weakest light signal[11]. However, the specific detectivity is limited by two factors viz. responsivity and noise current. Hence, considering the dark current as the main source of noise, the specific detectivity of a device can be given by the formula[12]

$$D^* = \frac{R_\lambda}{\sqrt{2qI_{\text{dark}}}} \quad (5.3)$$

where  $I_{\text{dark}}$  is the dark current at the same value of reverse bias as used for responsivity at a particular wavelength ( $R_\lambda$ ) and  $q$  is the charge of an electron. The specific detectivities at 325 nm and 20 V were  $2.4 \times 10^{10}$  Jones for ZnO-*f*-OPV device and  $2.7 \times 10^9$  Jones for ZnO device. To the best of our knowledge, this is the highest  $D^*$  value reported for a lamellar hybrid based UV-photodetector. The value of specific detectivity for a similar lamellar structure has been reported by Sofos *et al.* to be as high as  $2 \times 10^{10}$  Jones.[4] Interestingly, though this is the first time reported ZnO-*f*-OPV photodetector, the results are quite comparable to the previously reported ones. Furthermore, in our hybrid samples, selective photoexcitation of the nanocomposite lead to an increase in light current as in Figure 5.4(b), which shows the current to voltage characteristics of the hybrid compared with ZnO at  $\lambda = 325$  nm. It is known that ZnO forms schottky contact with Pt (Figure 5.4(b)).[13] However in our case, it is observed that the hybrid structure forms a “quasi ohmic” contact with Pt.[8] Under illumination, the trapped electrons align the Fermi energy of the nanocomposite with that of the electrode thus boosting the current.[14]

The dynamic photoresponse of ZnO-*f*-OPV was measured under chopped illumination (100 s ON and 50 s OFF) of UV-light (325 nm) while simultaneously measuring the current value at -5 V applied bias. The logarithmic plot of photocurrent vs. time of the ZnO-*f*-OPV hybrid in Figure 5.5(a) shows that soon after illumination, the current value increases about 2 orders higher than the dark current value. Once the illumination is off, immediately it is restored to its dark value. Figure 5.5(b) elucidates the effect of UV corresponding to the blend film before and after UV exposure, respectively.

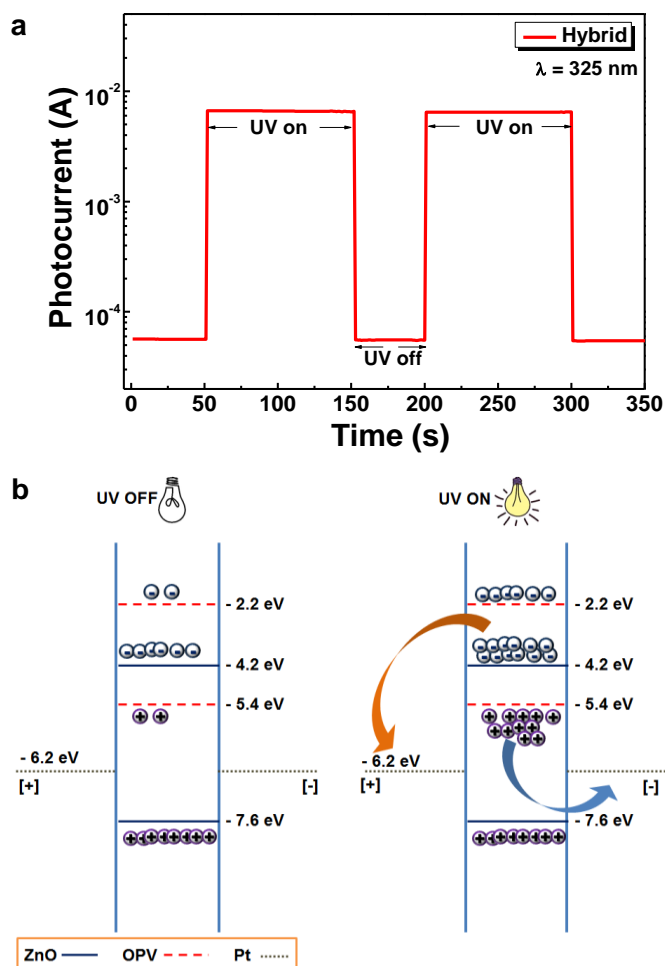


Figure 5.5. a) Temporal response of ZnO-*f*-oligophenylenevinylene hybrid at 325 nm and -5 V bias b) charge generation and transport model when UV light is off and when it is on at same bias and wavelength.

When the ZnO-*f*-OPV hybrid photodetector device is illuminated with a wavelength 325 nm, excitons are generated in both *f*-OPV and ZnO. On externally applying a bias, these photogenerated excitons in ZnO or *f*-OPV dissociate at various interfaces formed between the oligomer and ZnO inside the bulk and thus form a complimentary trajectory for the electrons from oligomer to transfer onto ZnO and holes to transfer onto *f*-OPV.[15] The overall photocurrent is thus increased. The maximum photocurrent value of 5.8 mA is similar to the value estimated from the I–V characteristics. There could be multiple processes leading to such an increase in the photocurrent. It has been previously reported that oxygen is necessary for the correct functioning of ZnO as an electron acceptor in these devices.[16] Since a lot of oxygen vacancies exist in the as-prepared ZnO nanostructure, it seems that such vacancies play a crucial role in the UV response as well. Additionally, when a high reverse bias is applied, the efficiency of charge transfer at the interface of ZnO and *f*-OPV is improved, substantiating more electron injection into ZnO thereby increasing light current.[17] However, both the rise and fall time of the response are approximately 0.8 s which can be obtained from the enlarged rising and decaying edges of the photoresponse curve, indicating an average photoresponse characteristics. Most likely, the charge trapping at the grain boundaries of the hybrid film is detrimental to the device performance.[18] Also, the presence of deep traps, which have longer charge release times, renders the device sluggish. Moreover, the photodetector response speed is also related to trap occupancy, which depends on light intensity. However, the response time at various light intensities could not be measured due to a limitation in the measurement system. A further enhancement in the device characteristics can be encouraged with appropriate device engineering, such as changing the ratio of organic to inorganic, changing the pH of the deposition solution, using a lower work-function electrode, etc. Nevertheless, in contrast to the previously reported photodetectors, our hybrid ultraviolet photodetectors are cost-effective and can be scaled up effortlessly to large areas. Furthermore, to check the stability of the devices, the devices were exposed to air and

kept in room ambience for eleven months, but no visible change in device performance was observed.

## **5.2. ZnO-OPV Based Gas Sensor**

### **5.2.1. Introduction**

Ammonia ( $\text{NH}_3$ ) is a conventional ingredient for a number of industries and also for various factories including the fertiliser industry, the petrochemical industry, etc. Occupational Safety and Health Administration (OSHA) declared that a threshold of 25 ppm of  $\text{NH}_3$  in air is quite dangerous for the human health [19]. Therefore, the development of a highly sensitive and highly selective ammonia sensor is important in view of the escalating environmental pollution. In the perspective of a device fabrication, especially in the contemporary and forthcoming era of plastic electronics, the use of hybrid nanostructures in gas sensor is an emerging research topic due to ease of tuning of the material properties.

Metal oxides have been extensively used as gas sensors due to their irreplaceable advantages, viz. low cost, small size and simple fabrication [20]–[22]. Their gas sensing mechanism is based on the electrical conductivity changes as a consequence of the chemical or physical interaction of the testing gas molecules with the gas-sensitive materials during exposure to analyte gas [23]–[25]. However, the challenge of fabricating gas-sensing elements with high performances such as high sensitivity, good selectivity and stability, fast response, low working temperature, and tunable parameters, still persists. Such performance is very important for the development of next-generation nanostructured gas-sensors. Interestingly, the self-assembly of  $\pi$ -conjugated molecules have been reported to result in many reciprocal developments towards such applications due to their unambiguous interactions within [26]–[29]. The hybrids formed from such self-assembled molecules are expected to be categorized as important materials. Recently, the different conducting polymer-inorganic nanocomposite conjugations

have received much attention because of their interesting properties and innumerable applications covering a wide area of interest [30]–[33].

ZnO is a typical *n*-type semiconductor, abundantly available and believed to be nontoxic and biocompatible [34], with many potential applications such as field effect transistors (FETs), gas sensors, nanogenerators, solar cells, photodetectors, materials for storing hydrogen, chemical sensors, and biosensors [35]–[42]. Moreover, the structural designs of functionalized oligo(*p*-phenylenevinylene), which are mostly controlled by hydrogen bonding as well as  $\pi$ - $\pi$  stacking interactions are recently being considered to a much extent due to their numerous applications [43]. Oligophenylenevinylene (OPV) is one of the typical conductive polymers which is usually considered as a *p*-type material and is used in making light batteries, electromagnetic shielding device, corrosion preventing coatings, and various sensors [8], [43], [44]. However, the ZnO-OPV composites have not been intensively studied among different composites and, hence, they can be expected to find applications in various devices.

Given the above-mentioned advantages of the materials properties, this work demonstrates, for the first time, the electrochemically deposited hybrid ZnO and OPV composite based gas sensor which is shown in Figure 5.6. Electrodeposition is known to be an economical technique requiring no intricate machinery. It also has several added advantages viz. low temperature processing, any favourable substrate dimension, controllable film thickness and growth under normal laboratory ambience [45]. Nonetheless, a highly ordered nanostructure is also significant to enhance the performance of such devices [46]. Considering the above perspective, the functionalized OPV, being known for its self-assembling architecture, interacts with the inorganic ZnO and forms ZnO-OPV composite. The functional group in the OPV can bind with the zinc ions in the inorganic phase. More importantly, the concept of this work is to use an environmentally benign and cheap composite based thin film as the sensing layer.

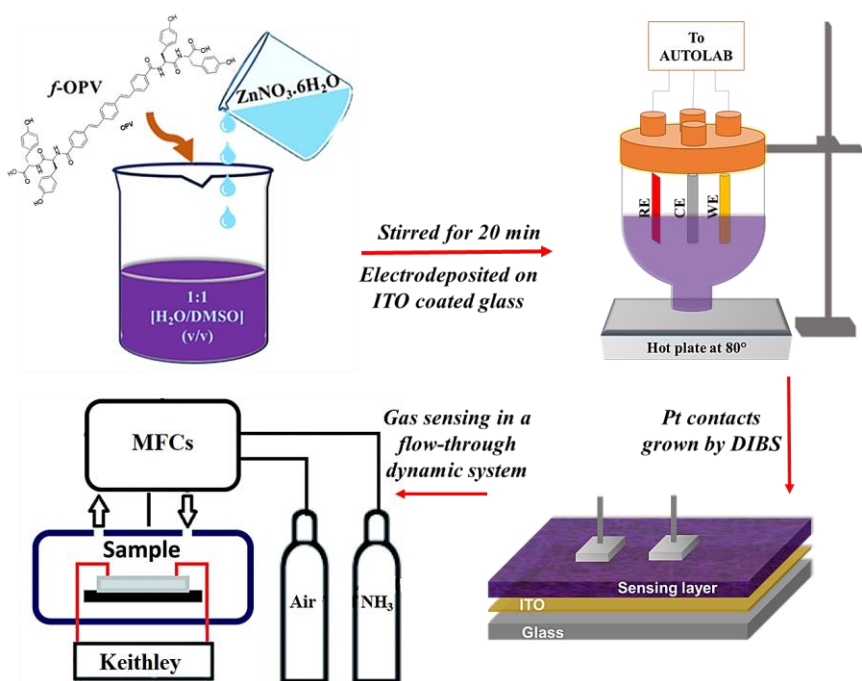


Figure 5.6. Schematic diagram of the preparation process for the ZnO-OPV hybrid.

## 5.2.2. Experiment Section

### 5.2.2.1. The Growth of Working Electrodes:

120 nm of indium tin oxide (ITO) thin films, deposited by dual ion beam sputtered (DIBS) on glass substrates were used as working electrodes. DIBS offers a distinctive advantage of *in-situ* pre-cleaning of the substrate over other sputtering techniques. The technique not only ensures better compositional ratios and film adherence but also offers high-quality growth with less surface roughness and improved homogeneity over the large surface area [2]. ITO thin films were deposited at 300 K by sputtering 99.99% pure 4-inch diameter ITO target disc for 5 h in pure Ar ambience.

### 5.2.2.2. Electrochemical Synthesis

Zn(NO<sub>3</sub>)<sub>2</sub>·6H<sub>2</sub>O (Aldrich, 98%) (0.02 M) with 2.0 mg OPV (compound 1) were dissolved in 24 ml solutions (1:1 (v/v) DMSO/H<sub>2</sub>O) to make the electrolyte. Autolab Potentiostat consisting a Pt counter electrode and an Ag/AgCl reference electrode were used for the electrochemical deposition [3]. Water facilitates reduction of NO<sup>-3</sup> to generate OH<sup>-</sup>, and

DMSO assists surfactant solubility. Working electrodes were placed upright in the cell and deposition was carried out at  $-0.9$  V for 30 min, under constant magnetic stirring at  $80$  °C. The deposited films were rinsed with DI water and dried with dry nitrogen gas. For device measurements and all other characterization,  $2.5$  cm $\times$  $2$  cm ITO–glass (120 nm thin, grown by DIBS system) electrodes were used.

#### *5.2.2.3. Synthesis of Standard Film*

ZnO thin film was used as a standard for XRD and response measurements. For the deposition of ZnO, the aqueous solution contained  $0.2$  M zinc nitrate hexahydrate ( $\text{Zn}(\text{NO}_3)_2 \cdot 6\text{H}_2\text{O}$ ) dissolved in DI water [3]. The electrolyte was stirred constantly throughout the deposition at a temperature of  $80$  °C ( $\pm 2$  °C) for 1 h at a potential of  $-0.9$  V.

#### *5.2.2.4. Device Fabrication*

An active layer of ZnO templated with OPV was electrochemically deposited onto an ITO coated glass anode ( $10 \Omega \cdot \text{cm}^{-1}$ ). The ZnO-OPV was annealed under vacuum at  $150$  °C for 2 h. On this film, the circular Pt electrodes, 3 mm apart, were directly deposited by RF-sputtering using a suitable mask.

#### *5.2.3. Device Characterization*

Rigaku SmartLab automated multipurpose X-ray diffractometer (XRD) with Cu-K $\alpha$  radiation ( $\lambda = 1.54$  Å) and field emission scanning electron microscopy (FESEM) using Sigma Supra<sup>TM</sup> 55 of Carl Zeiss were deployed to study the crystal structure and morphology, respectively of the prepared samples. Gas sensing properties of the ZnO-OPV composite based sensor were characterized in a dynamic flow-through measurement system comprising a custom made stainless steel based cylindrical gas sensing chamber. This chamber is installed with a cylindrical heater which acts as a sample holder as well. The temperature of the heater is controlled by an externally connected precise PID temperature controller (with an accuracy of  $\pm 1$  °C). The flow rate of gas was controlled by a mass flow controller (model: Alicat®, MC 1 slpm,

USA). The change in resistances were measured using the Keithley 4200A-SCS parameter analyzer.

## 5.2.4. Results and Discussions

### 5.2.4.1. Morphology and Structure

Figure 5.7(a) shows the field emission scanning electron microscopy (FESEM) image of annealed ZnO-OPV. It is seen that these structures are evenly deposited across the entire substrate with the nanostructures being oriented haphazardly. Although the orientation is random, the nanostructures are aggregated and closely associated with each other which can prove beneficial for better charge transport. An energy dispersive X-ray (EDX) analysis has been performed to determine the chemical composition of the hybrid nanostructures (annealed ZnO-OPV), as shown in Figure 5.7(b). The figure clearly shows the existing C, N, O and Zn species in the nanohybrids. The Zn/surfactant stoichiometry was assumed using the presence of C and N of the organic. As calculated, the EDX yielded Zn/C atomic ratio of 0.28 and the Zn/N atomic ratio of 1.36.

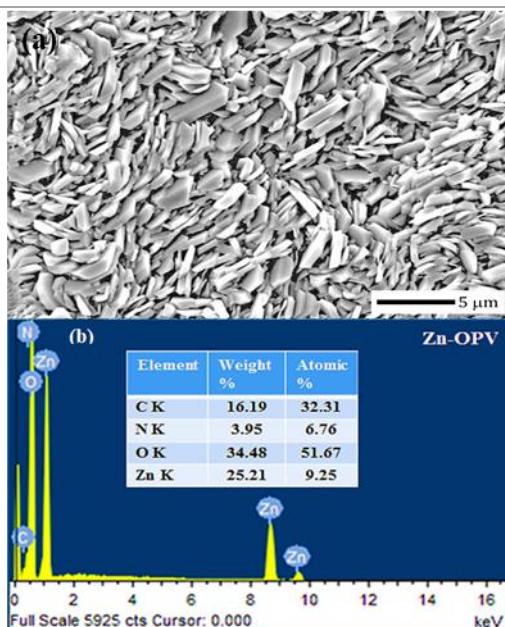


Figure 5.7. a) FESEM image of ZnO-OPV and b) EDX image of ZnO-OPV

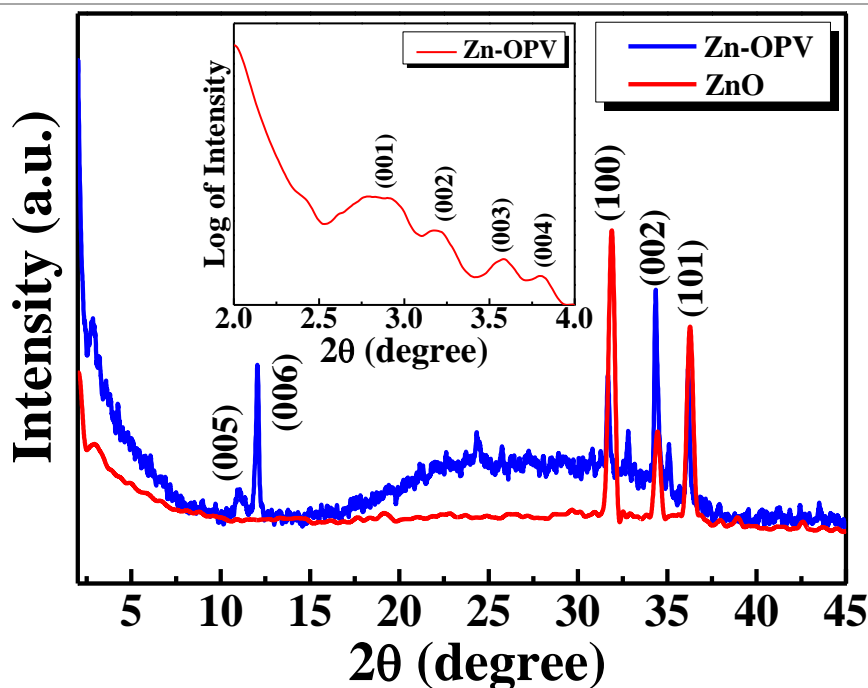


Figure 5.8. XRD images of ZnO and ZnO-OPV. Inset shows the peaks due to formation of lamellar structure.

The X-ray diffraction patterns of ZnO and ZnO-OPV (annealed) are shown in Figure 5.8. In both the cases, (100), (002) and (101) peaks of ZnO are dominant (JCPDS 36-1451). However, in case of ZnO-OPV, the peak intensities of (100), (002) and (101) are seen to be changed. Apart from the mentioned ZnO peaks, the (005) and the (006) reflections from the organic molecules are also quite prominent in case of ZnO-OPV. To confirm the presence of lamellar structure in ZnO-OPV nanohybrids, XRD measurements in the range of  $2\theta$  varying from  $2^\circ$  to  $6^\circ$  were also performed. Inset in Figure 5.8 shows the X-ray scattering at small angles confirming the highly ordered lamellar structure with d-spacing of 32 Å, 28 Å, 25 Å and 21 Å corresponding to (001), (002), (003) and (004) reflections, respectively.

#### 5.2.4.2. Device Performances

The sensing responses of the three sensors viz. OPV, ZnO, and ZnO-OPV sensors were measured by exposing them to different concentrations of  $\text{NH}_3$  gas at room temperature, as shown in Figure 5.9(a). It is seen that, among the three sensors, ZnO-OPV sensor shows

the best response. For the ZnO and the OPV sensors, the responses at all the concentrations are almost similar, i.e., they do not change much.

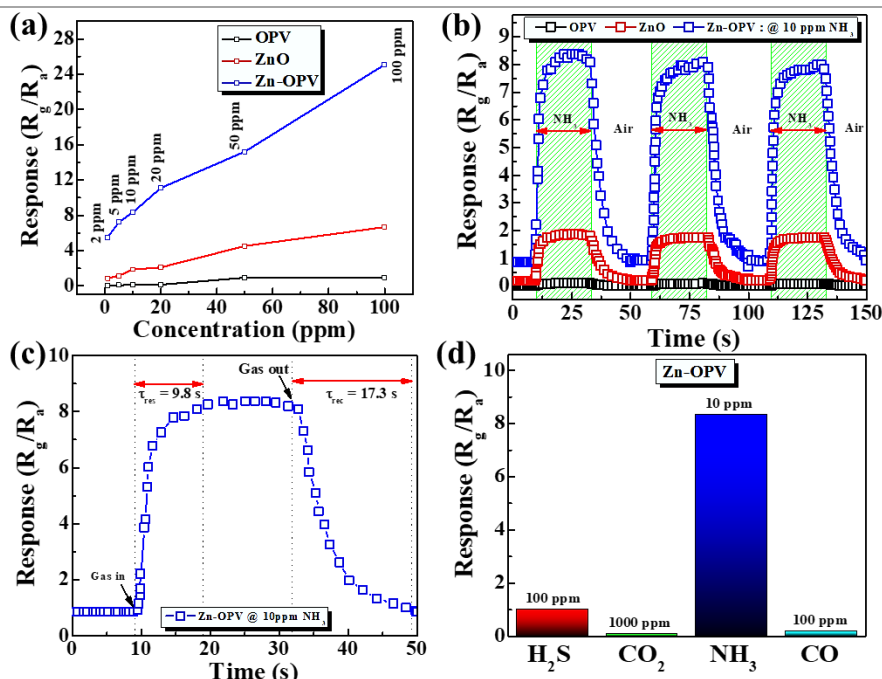


Figure 5.9. a) Sensing response of ZnO, OPV and ZnO-OPV with varying ppm of ammonia, b) cyclic response of ZnO, OPV and ZnO-OPV at 10 ppm of ammonia, c) single cycle response of ZnO-OPV towards 10 ppm of ammonia showing response time and recovery time, and d) selectivity graph showing selectivity of ZnO-OPV towards ammonia over other analyte gases.

However, in the case of ZnO-OPV sensor, the change in response with change in concentration is quite noticeable. Also, it is very clear from the figure that the response of ZnO-OPV sensor to lower concentrations of ammonia is much higher than that of ZnO and OPV. This implies that ZnO-OPV can be used even for sensing the lower concentrations of  $NH_3$  gas. The transient response of the sensors (OPV, ZnO, and ZnO-OPV) are shown in Figure 5.9(b). Amazingly, the resistance immediately increases when the ZnO-OPV sensor was exposed to  $NH_3$  and rapidly recovers with the withdrawal of  $NH_3$ . Here, the sensor response was defined as “Response =  $R_g/R_a$ ” where  $R_g$  is the resistance in the presence of the analyte gas, and  $R_a$  is the resistance in air or absence of the analyte gas. According to this equation, the response of OPV and

ZnO thin films are 0.09 and 1.86 to 10 ppm of  $\text{NH}_3$ , respectively. The highest response up to 8.33 is observed for the ZnO-OPV thin film, which is 4.48 times higher than the response of the ZnO thin film and approximately 95 times higher than that of OPV thin film. Also, the ZnO-OPV sensor shows good response and good repeatability upon exposure to  $\text{NH}_3$ , unlike other two sensors which are sluggish and slow. The OPV sensor shows no vivid response with time clearly indicating that its response and recovery time is quite large.

As seen in Figure 5.9(a) and 5.9(b), the response of ZnO-OPV thin film to  $\text{NH}_3$  is the highest of all the samples studied, so the composite sample is considered to be the best to be used as an ammonia sensor. The response and recovery times are also important parameters for a gas sensor, and these were defined as the times to reach 90% of the final value after the detected gas was first introduced and then removed, respectively. The response and recovery times of a ZnO-OPV thin film to 10 ppm of  $\text{NH}_3$  were 9.8 s and 17.3 s, respectively as shown in Figure 5.9(c). These response and recovery times indicate that the ZnO-OPV sensor has much faster response than many of the reported hybrid sensors, as tabulated in Table I. Nonetheless, a high selectivity is important for a gas sensor to be practically valuable. Therefore, the room temperature selectivity data of the ZnO-OPV thin film towards selected gases such as hydrogen sulphide, carbon dioxide, and carbon monoxide as shown in Figure 5.9(d), were 1 to 100 ppm, 0.1 to 1000 ppm, and 0.2 to 100 ppm, respectively, as compared to 10 ppm of  $\text{NH}_3$ . In hydrated state (in presence of humidity), the ionic mobility across the peptide bonds arises due to the  $\text{H}^+$  transfer from  $-\text{NHCO}-$  to  $-\text{N-COH}-$  via the hydrogen bonding with water. The  $\text{H}^+$  transfer becomes restricted in the presence of  $\text{NH}_3$  due to the formation of  $[\text{NH}_3\cdots\text{H}_2\text{O}]$  complex formation. As a consequence,  $\text{H}^+$  transfer across the peptide molecules become hindered, and resistance increases along the organic layer [47]. Stability performance of ZnO-OPV sensor films was measured to fixed 10 ppm concentration of  $\text{NH}_3$  gas at room temperature over the period

of 30 days at an interval of 1 day and obtained results are displayed in Figure 5.10.

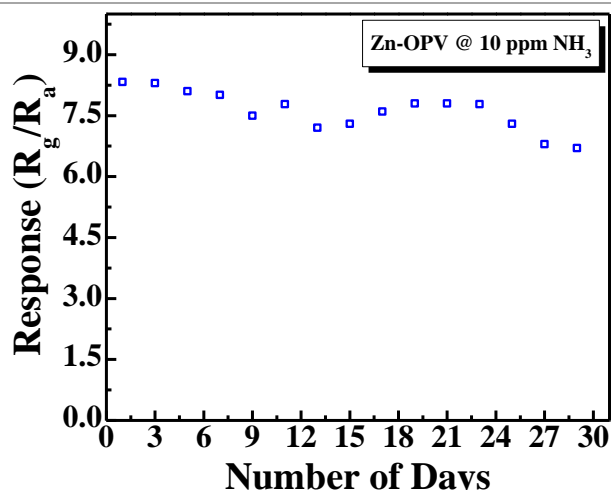


Figure 5.10. Long-term stability of ZnO-OPV at 10 ppm of NH<sub>3</sub>.

Initially, the sensor showed relatively maximum response of 8.33; however it dropped from 8.33 to 6.9 in 15 days. The response was seen to be unstable over the period of next 15 days. This may be because, in the later stage, the ZnO-OPV sensor undergoes both interface and surface modification and then reaches to an unsteady state indicating the long-term instability of the sensor operating at room temperature. A comparative characteristics of various ZnO based organic-inorganic hybrid sensors has been presented in Table 5.1. Schutt *et al.* [48] have reported a highly porous carbon nanotubes (CNTs) functionalized tetrapodal ZnO (ZnO-T-CNT) hybrid material for highly sensitive ammonia vapor detection at room temperature. Their fabricated sensor exhibited a response of 330 at 100 ppm of ammonia. However, the response and recovery times were 18.4 and 35 s, respectively. Tai *et al.* [49] deposited a ZnO nanoparticles and graphene oxide (GO) thin film on gold interdigitated electrodes in sequence via a simple spraying process, which was further restored to ZnO/reduced graphene oxide (rGO) bilayer thin film by the thermal reduction treatment. The rGO/ZnO sensor exhibited a low response of 3.05% for 50 ppm of NH<sub>3</sub> at room temperature with a moderate response and recovery times of 30 s and 90 s, respectively. Shukla *et al.* [50] reported zinc

oxide/polyaniline (ZnO/PANI) nanocomposite film prepared by a chemical method using CuSO<sub>4</sub> as redox initiator. Their nanocomposite sensor showed a low response of 4.75 to 1000 ppm NH<sub>3</sub> and response time and recovery time of 15 s and 45 s, respectively. Thus, from the table, it is clear that the ZnO-OPV not only does respond to a lower ppm of ammonia but also gives the least response and recovery times. The rGO/ZnO composite is seen to have the next lower concentration sensing. However, it shows quite longer recovery time.

*Table 5.1. Comparative analysis of sensing properties of various ZnO based organic-inorganic hybrid ammonia sensor.*

Material	Fabrication Method	Operating Temperature (°C)	Concentration (ppm)	Response	Response Time (s)	Recovery Time (s)	Ref.
ZnO-CNT	Simple Dripping	RT	100	330 *	18.4	35	[48]
rGO/ZnO	Spraying	RT	50	3.05 % <sup>s</sup>	30	90	[49]
PANI/ZnO	Drop Cast	-	1000	4.75 <sup>#</sup>	15	45	[50]
ZnO-OPV	Electrodeposition	RT	10	8.83	9.8	17.3	<b>This Work</b>

#### 5.2.4.3. Device Sensing Mechanism

It was observed that the ZnO-OPV composite sensor shows rapid resistance increase upon exposure to NH<sub>3</sub> which indicates *p*-type behavior of the composite. The presence of *p-n* heterojunction at the interface between OPV and ZnO may be attributed to the improved response in ZnO-OPV nanohybrids as compared to pure OPV. In air, at junction, due to mismatch of Fermi level between *p*-type OPV and *n*-type ZnO, the electron from conduction band of ZnO will flow across the interface to LUMO states of OPV until their Fermi energy level matches. As a result, a depletion layer is generated at the interface [51], [52], as shown in Figure 5.11. In NH<sub>3</sub> reducing gas, NH<sub>3</sub> molecules adsorbed on the surface of the hybrid and releases electron in the hybrid, especially into OPV in the junction region, which leads to decrease of the main carrier in OPV. As a result, the depletion layer thickness increases. Thus, this increase in depletion layer further increases the resistance of the ZnO-OPV composite in the presence of NH<sub>3</sub>. Also, layer-by-layer assemblies of *p*-type OPV and *n*-type ZnO showed fast

adsorption and desorption of  $\text{NH}_3$ . This was attributed to the presence of alternating ZnO layers, which might facilitate the flexible carrier transport path in ZnO-OPV composite [53].

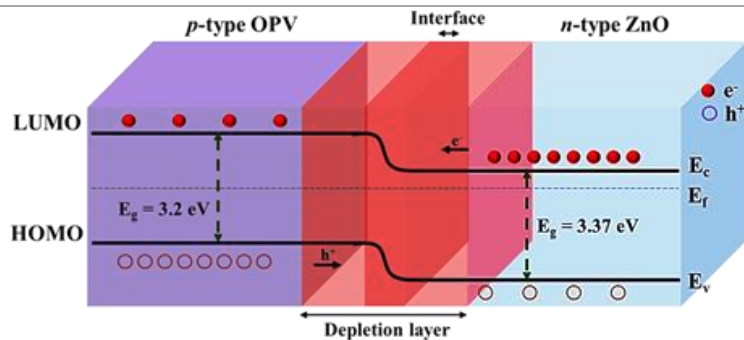


Figure 5.11. Schematics of sensing mechanism using the band diagram.

Although, the exact reason for the high selectivity of ZnO-OPV towards ammonia is not clear, yet, the reason that might account for the excellent selectivity is: ammonia has a strong electron donating ability due to the presence of a lone electron pair, and thus it can readily donate the unpaired electrons. The sensing layer, consisting of the  $p$ -type OPV might have higher binding affinity for the electron-donating ammonia [8], [54]. Hence, the electrons get transferred to the sensing layer, which may lead to significant change in resistance [54], [55]. Also, the layer by layer self-assembly of OPV and ZnO provides a continuous path for charge transfer, thus, providing a faster response.

### 5.3. Conclusion

The contribution from the present work can be summarized as under:

- The ZnO-OPV hybrid photodetector is demonstrated for the first time in literature. The photoresponse and external quantum efficiency of the nanohybrid photodetector were measured at different bias voltages and reached  $0.2 \text{ AW}^{-1}$  and 75.5%, respectively, at -20 V. These experimental findings indicate that the hybrid nanostructure of ZnO-OPV may be especially well suited for the use in high-performance nanoscale photodetectors.
- Sensors with sensing layers made up of OPV, ZnO and ZnO-OPV composites are successfully synthesized by

electrochemical deposition. The composite based sensor exhibited the highest response of 8.83 to 10 ppm of NH<sub>3</sub>. It showed an excellent selectivity to NH<sub>3</sub> among various test gases.

#### 5.4. References

- [1] S. Verma, M. K. Manna, S. K. Pandey, A. K. Das, and S. Mukherjee, "Benzo[ghi]perylene monoimide based photosensitive lamellar Cd-doped ZnO nanohybrids," *RSC Adv.*, vol. 4, no. 107, pp. 62603–62614, 2014.
- [2] R. Singh, P. Sharma, M. A. Khan, V. Garg, V. Awasthi, A. Kranti, and S. Mukherjee, "Investigation of barrier inhomogeneities and interface state density in Au/MgZnO: Ga Schottky contact," *J. Phys. D. Appl. Phys.*, vol. 49, no. 44, p. 445303, Nov. 2016.
- [3] Aaryashree, S. Biswas, P. Sharma, V. Awasthi, B. S. Sengar, A. K. Das, and S. Mukherjee, "Photosensitive ZnO-Graphene Quantum Dot Hybrid Nanocomposite for Optoelectronic Applications," *ChemistrySelect*, vol. 1, no. 7, pp. 1503–1509, May 2016.
- [4] M. Sofos, J. Goldberger, D. A. Stone, J. E. Allen, Q. Ma, D. J. Herman, W.-W. Tsai, L. J. Lauhon, and S. I. Stupp, "A synergistic assembly of nanoscale lamellar photoconductor hybrids," *Nat. Mater.*, vol. 8, no. 1, pp. 68–75, Jan. 2009.
- [5] N. Haberkorn, M. C. Lechmann, B. H. Sohn, K. Char, J. S. Gutmann, and P. Theato, "Templated Organic and Hybrid Materials for Optoelectronic Applications," *Macromol. Rapid Commun.*, vol. 30, no. 14, pp. 1146–1166, Jul. 2009.
- [6] H. Tampo, H. Shibata, K. Maejima, T.-W. W. Chiu, H. Itoh, A. Yamada, K. Matsubara, P. Fons, Y. Chiba, T. Wakamatsu, Y. Takeshita, H. Kanie, and S. Niki, "Band profiles of ZnMgO/ZnO heterostructures confirmed by Kelvin probe force microscopy," *Appl. Phys. Lett.*, vol. 94, no. 24, p. 242107, 2009.

- [7] M. Nakano, A. Tsukazaki, R. Y. Gunji, K. Ueno, A. Ohtomo, T. Fukumura, and M. Kawasaki, "Schottky contact on a ZnO (0001) single crystal with conducting polymer," *Appl. Phys. Lett.*, vol. 91, no. 14, p. 142113, Oct. 2007.
- [8] J.-F. Eckert, J.-F. Nicoud, J.-F. Nierengarten, S. Liu, L. Echegoyen, F. Barigelletti, N. Armaroli, L. Ouali, V. Krasnikov, and G. Hadziioannou, "Fullerene–Oligophenylenevinylene Hybrids: Synthesis, Electronic Properties, and Incorporation in Photovoltaic Devices," *J. Am. Chem. Soc.*, vol. 122, no. 31, pp. 7467–7479, Aug. 2000.
- [9] D. N. Congreve, J. Lee, N. J. Thompson, E. Hontz, S. R. Yost, P. D. Reuswig, M. E. Bahlke, S. Reineke, T. Van Voorhis, and M. A. Baldo, "External Quantum Efficiency Above 100% in a Singlet-Exciton-Fission-Based Organic Photovoltaic Cell," *Science (80-. )*, vol. 340, no. 6130, pp. 334–337, Apr. 2013.
- [10] B. S. Mashford, M. Stevenson, Z. Popovic, C. Hamilton, Z. Zhou, C. Breen, J. Steckel, V. Bulovic, M. Bawendi, S. Coe-Sullivan, and P. T. Kazlas, "High-efficiency quantum-dot light-emitting devices with enhanced charge injection," *Nat. Photonics*, vol. 7, no. 5, pp. 407–412, Apr. 2013.
- [11] J.-M. Liu, *Photonic Devices*. Cambridge: Cambridge University Press, 2005.
- [12] D. Y. Kim, J. Ryu, J. Manders, J. Lee, and F. So, "Air-Stable, Solution-Processed Oxide p–n Heterojunction Ultraviolet Photodetector," *ACS Appl. Mater. Interfaces*, vol. 6, no. 3, pp. 1370–1374, Feb. 2014.
- [13] S.-H. Kim, H.-K. Kim, and T.-Y. Seong, "Effect of hydrogen peroxide treatment on the characteristics of Pt Schottky contact on n-type ZnO," *Appl. Phys. Lett.*, vol. 86, no. 11, p. 112101, Mar. 2005.
- [14] F. Guo, B. Yang, Y. Yuan, Z. Xiao, Q. Dong, Y. Bi, and J. Huang,

- “A nanocomposite ultraviolet photodetector based on interfacial trap-controlled charge injection,” *Nat. Nanotechnol.*, vol. 7, no. 12, pp. 798–802, Nov. 2012.
- [15] F. Liu, Y. Gu, J. W. Jung, W. H. Jo, and T. P. Russell, “On the morphology of polymer-based photovoltaics,” *J. Polym. Sci. Part B Polym. Phys.*, vol. 50, no. 15, pp. 1018–1044, Aug. 2012.
- [16] M. Lira-Cantu, K. Norrman, J. W. Andreasen, N. Casan-Pastor, and F. C. Krebs, “Detrimental Effect of Inert Atmospheres on Hybrid Solar Cells Based on Semiconductor Oxides,” *J. Electrochem. Soc.*, vol. 154, no. 6, p. B508, 2007.
- [17] Y.-Y. Lin, C.-W. Chen, W.-C. Yen, W.-F. Su, C. Ku, and J.-J. Wu, “Near-ultraviolet photodetector based on hybrid polymer/zinc oxide nanorods by low-temperature solution processes,” *Appl. Phys. Lett.*, vol. 92, no. 23, p. 233301, Jun. 2008.
- [18] P. A. C. Quist, W. J. E. Beek, M. M. Wienk, R. A. J. Janssen, T. J. Savenije, and L. D. A. Siebbeles, “Photogeneration and Decay of Charge Carriers in Hybrid Bulk Heterojunctions of ZnO Nanoparticles and Conjugated Polymers,” *J. Phys. Chem. B*, vol. 110, no. 21, pp. 10315–10321, Jun. 2006.
- [19] D. K. Bandgar, S. T. Navale, A. T. Mane, S. K. Gupta, D. K. Aswal, and V. B. Patil, “Ammonia sensing properties of polyaniline/ $\alpha$ -Fe<sub>2</sub>O<sub>3</sub> hybrid nanocomposites,” *Synth. Met.*, vol. 204, pp. 1–9, Jun. 2015.
- [20] L. a. Obvintseva, “Metal oxide semiconductor sensors for determination of reactive gas impurities in air,” *Russ. J. Gen. Chem.*, vol. 78, no. 12, pp. 2545–2555, Dec. 2008.
- [21] U. Kizil and J. A. Lindley, “Potential use of gas sensors in beef manure nutrient content estimations,” *African J. Biotechnol.*, vol. 8, no. 12, 2009.
- [22] D. Kohl, “Function and applications of gas sensors,” *J. Phys. D*.

- Appl. Phys., vol. 34, no. 19, pp. R125–R149, Oct. 2001.
- [23] M. Tiemann, “Porous Metal Oxides as Gas Sensors,” *Chem. - A Eur. J.*, vol. 13, no. 30, pp. 8376–8388, Oct. 2007.
- [24] L. Jia and W. Cai, “Micro/Nanostructured Ordered Porous Films and Their Structurally Induced Control of the Gas Sensing Performances,” *Adv. Funct. Mater.*, vol. 20, no. 21, pp. 3765–3773, Nov. 2010.
- [25] G. Jiménez-Cadena, J. Riu, and F. X. Rius, “Gas sensors based on nanostructured materials,” *Analyst*, vol. 132, no. 11, pp. 1083–99, Nov. 2007.
- [26] J. F. Hulvat, M. Sofos, K. Tajima, and S. I. Stupp, “Self-Assembly and Luminescence of Oligo(*p*-phenylene vinylene) Amphiphiles,” *J. Am. Chem. Soc.*, vol. 127, no. 1, pp. 366–372, Jan. 2005.
- [27] C. Reese and Z. Bao, “Organic single-crystal field-effect transistors,” *Mater. Today*, vol. 10, no. 3, pp. 20–27, Mar. 2007.
- [28] A. P. H. J. Schenning and E. W. Meijer, “Supramolecular electronics; nanowires from self-assembled pi-conjugated systems,” *Chem. Commun. (Camb)*, no. 26, pp. 3245–58, Jul. 2005.
- [29] B. W. Messmore, J. F. Hulvat, E. D. Sone, and S. I. Stupp, “Synthesis, Self-Assembly, and Characterization of Supramolecular Polymers from Electroactive Dendron Rodcoil Molecules,” *J. Am. Chem. Soc.*, vol. 126, no. 44, pp. 14452–14458, Nov. 2004.
- [30] L. Jia, W. Cai, and H. Wang, “Layer-by-layer strategy for the general synthesis of 2D ordered micro/nanostructured porous arrays: structural, morphological and compositional controllability,” *J. Mater. Chem.*, vol. 19, no. 39, p. 7301, Oct. 2009.

- [31] L. Jia, W. Cai, H. Wang, F. Sun, and Y. Li, "Hetero-apertured Micro/Nanostructured Ordered Porous Array: Layer-by-Layered Construction and Structure-Induced Sensing Parameter Controllability," *ACS Nano*, vol. 3, no. 9, pp. 2697–2705, Sep. 2009.
- [32] F. Sun, W. Cai, Y. Li, B. Cao, Y. Lei, and L. Zhang, "Morphology-Controlled Growth of Large-Area Two-Dimensional Ordered Pore Arrays," *Adv. Funct. Mater.*, vol. 14, no. 3, pp. 283–288, Mar. 2004.
- [33] Y. Li, W. Cai, and G. Duan, "Ordered Micro/Nanostructured Arrays Based on the Monolayer Colloidal Crystals," *Chem. Mater.*, vol. 20, no. 3, pp. 615–624, Feb. 2008.
- [34] J. Zhou, N. S. Xu, and Z. L. Wang, "Dissolving Behavior and Stability of ZnO Wires in Biofluids: A Study on Biodegradability and Biocompatibility of ZnO Nanostructures," *Adv. Mater.*, vol. 18, no. 18, pp. 2432–2435, Sep. 2006.
- [35] B. Mandal, Aaryashree, R. Singh, and S. Mukherjee, "Highly Selective and Sensitive Methanol Sensor Using Rose-Like ZnO Microcube and MoO<sub>3</sub> Micrograss-Based Composite," *IEEE Sens. J.*, vol. 18, no. 7, pp. 2659–2666, Apr. 2018.
- [36] R. Bhardwaj, P. Sharma, R. Singh, M. Gupta, and S. Mukherjee, "High Responsivity Mg<sub>x</sub>Zn<sub>1-x</sub>O Based Ultraviolet Photodetector Fabricated by Dual Ion Beam Sputtering," *IEEE Sens. J.*, vol. 18, no. 7, pp. 2744–2750, Apr. 2018.
- [37] M. Anbia, M. Faryadras, and A. Ghaffarinejad, "Synthesis and Characterization of Zn<sub>3</sub>(BTC)<sub>2</sub> Nanoporous Sorbent and its Application for Hydrogen Storage at Ambient Temperature," vol. 41, pp. 33–41, 2015.
- [38] Q. Li, K. Cheng, W. Weng, P. Du, and G. Han, "Synthesis, characterization and electrochemical behavior of Sb-doped ZnO microsphere film," *Thin Solid Films*, vol. 544, pp. 466–471, Oct.

2013.

- [39] V. V. Atuchin, E. N. Galashov, A. S. Kozhukhov, L. D. Pokrovsky, and V. N. Shlegel, “Epitaxial growth of ZnO nanocrystals at ZnWO<sub>4</sub>(010) cleaved surface,” *J. Cryst. Growth*, vol. 318, no. 1, pp. 1147–1150, Mar. 2011.
- [40] V. Garg, B. S. Sengar, V. Awasthi, A. Kumar, R. Singh, S. Kumar, C. Mukherjee, V. V. Atuchin, and S. Mukherjee, “Investigation of Dual-Ion Beam Sputter-Instigated Plasmon Generation in TCOs: A Case Study of GZO,” *ACS Appl. Mater. Interfaces*, vol. 10, no. 6, pp. 5464–5474, Feb. 2018.
- [41] A. Meng, J. Xing, Z. Li, Q. Wei, and Q. Li, “Ag/AgCl/ZnO nano-networks: Preparation, characterization, mechanism and photocatalytic activity,” *J. Mol. Catal. A Chem.*, vol. 411, pp. 290–298, Jan. 2016.
- [42] Aaryashree, P. Sharma, B. Mandal, A. Biswas, M. K. Manna, S. Maiti, A. K. Das, and S. Mukherjee, “Synergetic Accrual of Lamellar Nanohybrids for Band-Selective Photodetection,” *J. Phys. Chem. C*, vol. 121, no. 26, pp. 14037–14044, Jul. 2017.
- [43] V. K. Praveen, C. Ranjith, E. Bandini, A. Ajayaghosh, and N. Armaroli, “Oligo(phenylenevinylene) hybrids and self-assemblies: versatile materials for excitation energy transfer,” *Chem. Soc. Rev.*, vol. 43, no. 12, pp. 4222–4242, 2014.
- [44] A. Chaieb, L. Vignau, R. Brown, G. Wantz, N. Huby, J. François, and C. Dagron-Lartigau, “PL and EL properties of oligo(p-phenylene vinylene) (OPPV) derivatives and their applications in organic light-emitting diodes (OLED),” *Opt. Mater. (Amst.)*, vol. 31, no. 1, pp. 68–74, Sep. 2008.
- [45] T. Pauporté and D. Lincot, “Electrodeposition of semiconductors for optoelectronic devices: results on zinc oxide,” *Electrochim. Acta*, vol. 45, no. 20, pp. 3345–3353, Jun. 2000.

- [46] M. K. Manna, Aaryashree, S. Verma, S. Mukherjee, and A. K. Das, "Lamellar Peptide-Cadmium-Doped Zinc Oxide Nanohybrids That Emit White Light," *Chempluschem*, vol. 81, no. 3, pp. 329–337, Mar. 2016.
- [47] D. Porter and F. Vollrath, "Water mediated proton hopping empowers proteins," *Soft Matter*, vol. 9, no. 3, pp. 643–646, 2013.
- [48] F. Schütt, V. Postica, R. Adelung, and O. Lupan, "Single and Networked ZnO–CNT Hybrid Tetrapods for Selective Room-Temperature High-Performance Ammonia Sensors," *ACS Appl. Mater. Interfaces*, vol. 9, no. 27, pp. 23107–23118, Jul. 2017.
- [49] H. Tai, Z. Yuan, W. Zheng, Z. Ye, C. Liu, and X. Du, "ZnO Nanoparticles/Reduced Graphene Oxide Bilayer Thin Films for Improved NH<sub>3</sub>-Sensing Performances at Room Temperature," *Nanoscale Res. Lett.*, vol. 11, no. 1, p. 130, Dec. 2016.
- [50] S. K. Shukla, N. B. Singh, and R. P. Rastogi, "Efficient ammonia sensing over zinc oxide/polyaniline nanocomposite," *Indian J. Eng. Mater. Sci.*, vol. 20, no. 4, pp. 319–324, 2013.
- [51] H. Tai, Y. Jiang, G. Xie, J. Yu, and X. Chen, "Fabrication and gas sensitivity of polyaniline–titanium dioxide nanocomposite thin film," *Sensors Actuators B Chem.*, vol. 125, no. 2, pp. 644–650, Aug. 2007.
- [52] J. Sun, X. Shu, Y. Tian, Z. Tong, S. Bai, R. Luo, D. Li, and A. Chen, "Preparation of polypyrrole@WO<sub>3</sub> hybrids with p-n heterojunction and sensing performance to triethylamine at room temperature," *Sensors Actuators B Chem.*, vol. 238, pp. 510–517, Jan. 2017.
- [53] M. Gerard, A. Chaubey, and B. D. Malhotra, "Application of conducting polymers to biosensors," *Biosens. Bioelectron.*, vol. 17, no. 5, pp. 345–359, May 2002.
- [54] S. Virji, J. Huang, R. B. Kaner, and B. H. Weiller, "Polyaniline

Nanofiber Gas Sensors: Examination of Response Mechanisms,”  
Nano Lett., vol. 4, no. 3, pp. 491–496, Mar. 2004.

- [55] A. Hagfeldt and M. Graetzel, “Light-Induced Redox Reactions in Nanocrystalline Systems,” Chem. Rev., vol. 95, no. 1, pp. 49–68, Jan. 1995.

# Chapter 6

## Conclusion and Scope for Future Work

In this research work, the optimization and fabrication of ZnO based organic-inorganic hybrid materials and their thin films were performed using the electrodeposition technique. After the growth, the thin films were characterized for structural, electrical, optical, morphological and elemental properties. Efforts were put to establish the correlations among different properties by employing XRD, AFM, FESEM, Raman, SE, PL and *I-V* measurement techniques. Also, the thin films were employed to make devices such as photodetector and gas sensor. Therefore, in summary, the present thesis work mainly discussed the following,

- **Study of ZnO-Graphene Quantum Dots (GQD) hybrid:**
  - Synthesis: GQD, ZnO, and ZnO-GQD hybrid were deposited by the electrodeposition process. Also, the Pt electrodes were grown on the three samples.
  - Characterization: A comparative study of optical, elemental, electrical, crystalline and morphological properties of the grown thin films (GQD, ZnO, and ZnO-GQD hybrid) were discussed. The effect of addition of GQD to ZnO has been established through characterization techniques such as PL, FESEM, *I-V* characteristics and SE measurements. Studies revealed that the GQDs play a significant role in shifting the PL peaks of the films. Observations also concluded that the ZnO-GQD nanocomposites, in comparison to the ZnO and GQD individual films, produced higher optical band gap (3.33 eV). The electrical measurements also showed improved current sensitivity of the ZnO-GQD hybrid

nanocomposites film over pure organic GQD and inorganic ZnO film. The values of photosensitivity of ZnO, GQD, and ZnO-GQD nanocomposite were found to be 6.77, 51, and 99.32, respectively at room temperature. The enhancement of photosensitivity of ZnO-GQD nanocomposite was 1.9-fold and 14.67-fold as compared to that of GQDs and ZnO, respectively.

- *Application:* Since the ZnO-GQD showed enhanced optical properties, it be utilized for various optoelectronic applications.

- **ZnO-Oligo(*p*-phenylenevinylene) (OPV) hybrid:**

- *Synthesis:* The synthesis of OPV, ZnO and ZnO-OPV hybrid has been done. Further, they have been deployed as sensing layers in two different devices a) photodetector, and b) gas sensor.
- *Characterization:* Study of structural, elemental, electrical, morphological and optical properties of the grown thin films (OPV, ZnO and ZnO-OPV hybrid).
- *Applications:*

*Fabrication of ZnO-OPV based band-selective ultraviolet (UV) photodetector.*

The ZnO-OPV hybrid photodetector is demonstrated for the first time in literature. The photoresponse and external quantum efficiency of the nanohybrid photodetector were measured at different bias voltages and reached  $0.2 \text{ AW}^{-1}$  and 75.5%, respectively, at -20 V. These experimental findings indicate that the hybrid nanostructure of ZnO-OPV may be especially well suited for the use in high-performance nanoscale photodetectors.

*Fabrication of ZnO-OPV based highly selective ammonia gas sensor.*

Sensors with sensing layers made up of OPV, ZnO and ZnO-OPV composites are successfully synthesized by electrochemical deposition. The composite based sensor exhibited the highest response of 8.83 to 10 ppm of NH<sub>3</sub>. It showed an excellent selectivity to NH<sub>3</sub> among various test gases.

The following are the future work that can be focused:

- Other functionalized organic moiety can be tested to make a composite with ZnO to give more stable composites for long-term sensing.
- The fabricated sensors can be further explored for application in the sensor array.